A Review of Aeronautical Fatigue Investigations in Sweden During the Period April 2017 to March 2019

Edited by Zlatan Kapidzic
Saab AB
Sweden

Saab Doc. No. LN-049888

Presented at the 36th Conference of the International Committee on Aeronautical Fatigue and Structural Integrity (ICAF), Krakow, Poland, 3-4 June 2019.

CONTENT

CONTENT

1 INTRODUCTION

In this paper a review is given of the work carried out in Sweden in the area of aeronautical fatigue and structural integrity during the period April 2017 to March 2019. The review includes basic studies and industrial applications.

Contributions to the present review are from the following bodies:

§ Saab AB
Sections 2.1, 2.2, 2.3, 2.4, 2.5, 2.6, 2.7, 2.8, 2.9, 2.10, 3.1, 3.4

§ Linköping University (LiU)
Sections 2.9, 2.10, 3.1, 4.1

§ The Royal Institute of Technology (KTH)
Sections 3.2

§ RISE SICOMP, OXEON AB
Section 3.3, 3.4

§ Technical Research Centre of Finland (VTT)
Section 2.8

2 STRUCTURAL INTEGRITY CHARACTERISTICS OF METAL MATERIALS AND STRUCTURE

2.1 Damage tolerance test verification programme for Gripen E airframe

Zlatan Kapidžić, Martin Ekström, Hans Ansell, Saab AB

Service life and damage tolerance capability need to be verified by testing. These tests can either be based on similarities to previously conducted tests, if applicable, or by new tests when no previous test results are available. Full-scale testing is required when:

- Changed design principles in primary load paths
- Changed material in safety-of-flight critical parts
- Significant change of stress conditions in legacy primary load paths

When Gripen A/B was initially developed, the test verification task was huge since all of the above criteria applied. Especially the implementation of the damage tolerance task according to the MIL-A-83444 specification called for test verification. An extensive fatigue and damage tolerance test program of full-scale test assemblies was accomplished, see figure 2.1-1. Both airframe and systems parts, e.g. actuators in the flight control system, were included and a total of about 800 artificial defects, sizing between .05 and .25 inch, were introduced in the structural parts and in the correct structural surroundings. In addition conventional full-scale static and fatigue tests of both A and B versions were conducted covering testing beyond ultimate loads and 4 lifetimes respectively.

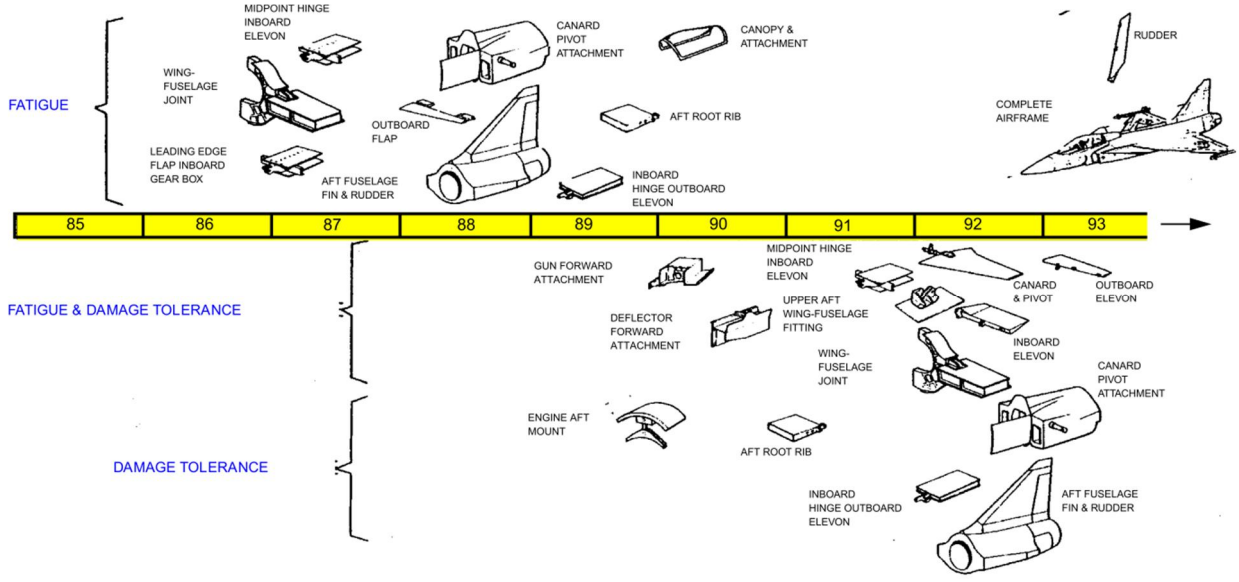

Figure 2.1-1. Test programme for fatigue and damage tolerance verification of Gripen A/B airframe.

When Gripen C/D was developed, no change of materials was done and no change of major load paths. Essential changes of local geometries were however done through the redesign to integral structures, extended service life (from 4,000 to 8,000 hours) and increased basic design mass (~10% compared to A/B versions) and some other load and structural changes, e.g. air-to-air refuelling probe, called for new full-scale fatigue tests, se figure 2.1-2. Damage tolerance tests were however not done in any large extent since the load path were the same although redesigned but the validation effort done on the fracture mechanic based damage

tolerance methods during the A/B developments were deemed to be sufficient also for the C/D versions.

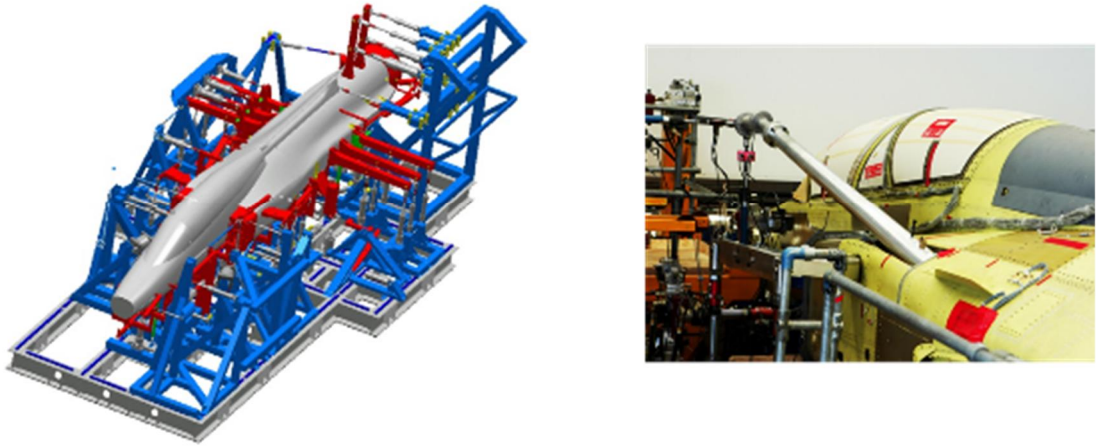

Figure 2.1-2. Full-scale fatigue test of Gripen D version.

With the development of Gripen NG versions, structural changes were made that interrogated with several of the criteria for the need of test verification. Certification for airworthiness by full-scale testing required due to:

- New mid fuselage/wing design, fuselage joints, MLG attachments
- Change of classification of parts due to design-for-manufacturing purposes
- Use of a new material type (Al-Li AA2050 and AA2060)
- Increased basic design mass (~40% compared to C/D versions)
- New operational profiles

These structural changes call for a more extensive test programme than what was needed for the C/D versions. A full-scale static test (including impact damaged composite parts) of the complete airframe is underway and a full-scale fatigue test of the complete airframe will follow thereafter and tested in the same rig for 4 lifetimes, see figure 2.1-3. In addition to the full-scale fatigue test, control surfaces (not included in the test airframe) will be tested in separate assemblies. These tests will be a combined fatigue and damage tolerance test by initially cycled for 2 lifetimes without artificial initial defect followed by 2 lifetimes with artificially manufactured defects installed.

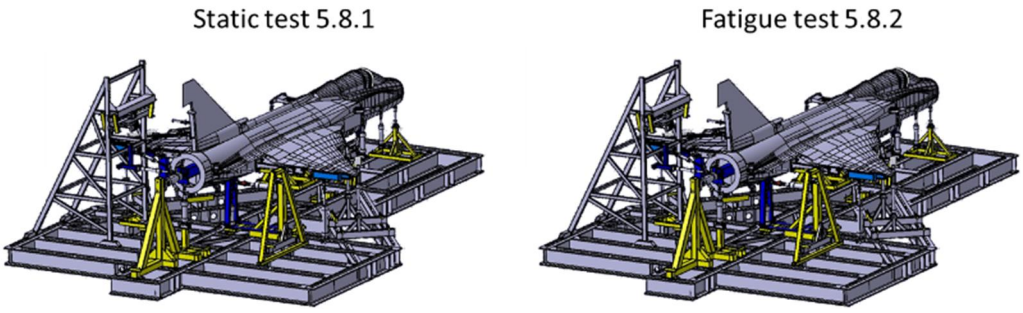

Figure 2.1-3. Full scale fatigue tests of Gripen E version.

Full-scale tests for compliance with damage tolerance requirements are also needed due to the structural changes in load paths and the upgraded classification of fuselage stringer joints and the design change of the wing to fuselage joint. A change from AA7050 alloy to AA2050

alloy in safety-of-flight critical parts also makes the damage tolerance test verification needed. The decision to use aluminium-lithium alloys in primary structural components was preceded by extensive validations of the fatigue and damage tolerance material properties. To assure necessary and sufficient confidence regarding damage tolerance, a significant test effort designed to challenge typical airframe crack scenarios with part through cracks (surface cracks in thickness steps, open and loaded holes etc.) was accomplished.

Figure 2.1-4 shows structural objects/assemblies which are verified for damage tolerance when having multiple artificial initial defects installed in critical sections. Some of the ongoing tests from Fig. 2.1-4 are described in more detail in the following sections.

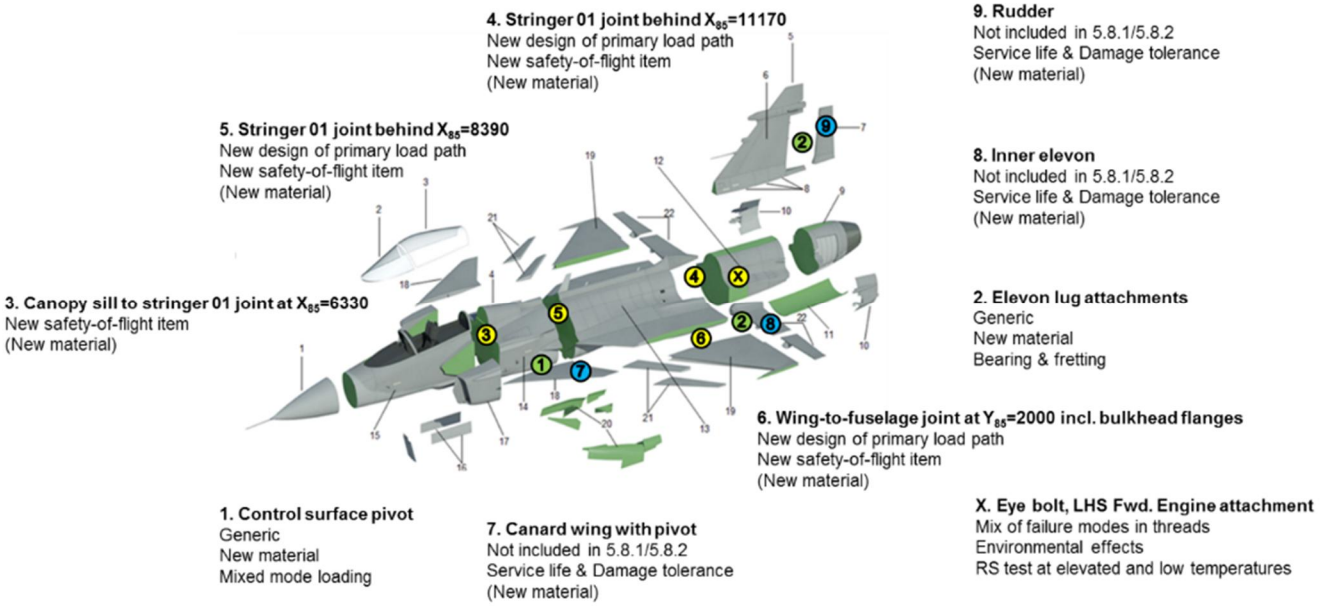

Figure 2.1-4. Full-scale damage tolerance tests of assemblies having artificial defects installed.

Wing to fuselage joint at Y_{85}=2000

COMPONENT TEST

The component test "Wing to fuselage joint at Y_{85}=2000 incl. bulkhead flanges" is a certification test. The cause of test is new design, upgraded criticality level and material change. Two identical specimens are to be tested, see Figure 2.1-5, one in static loading and one in fatigue with artificial defects.

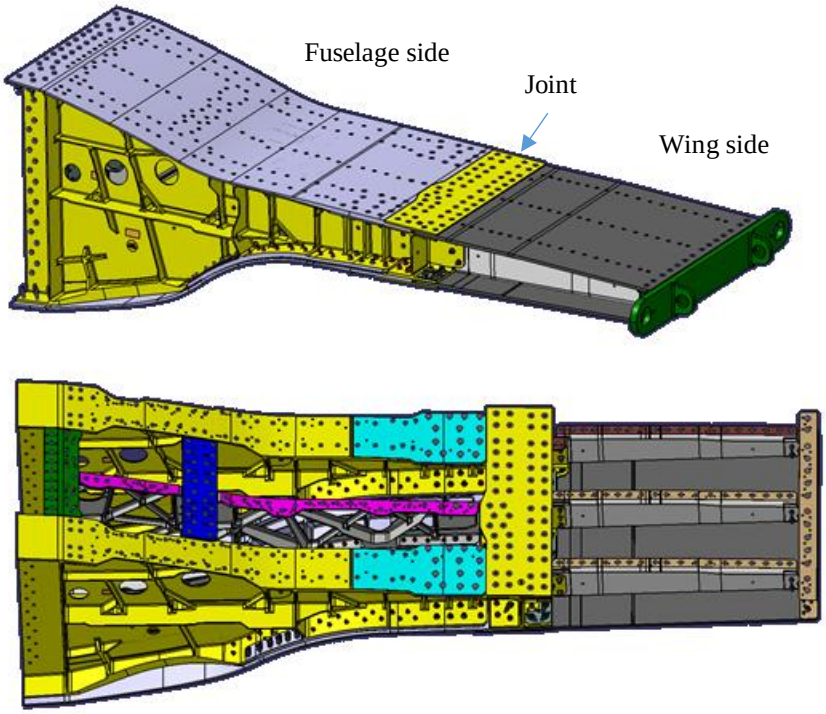

Figure 2.1-5. The component test object “Wing to fuselage joint at Y_{85}=2000”.

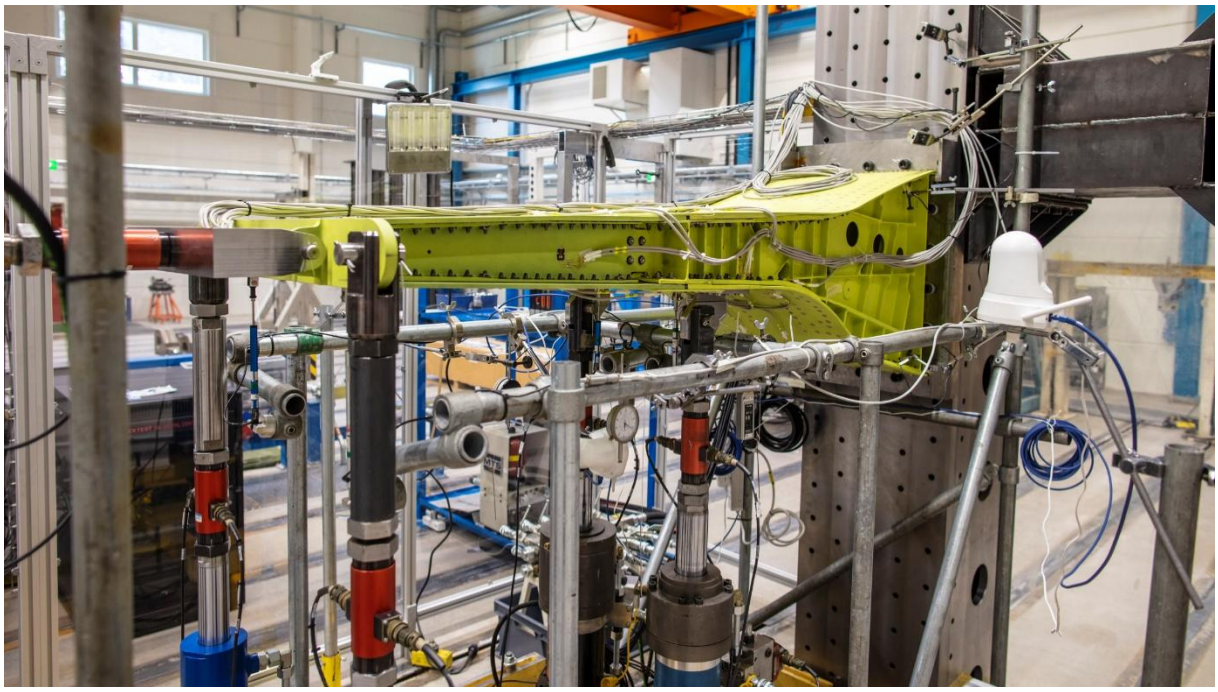

Figure 2.1-6. The static component test arrangement “Wing to fuselage joint at Y_{85}=2000.

The test specimens are mounted on a wall at the fuselage side and the tensile/bending loads are applied by five actuators, as shown in Fig. 2.1-6. In order to apply the correct loads in critical sections in the joint and frames an FE-model of the test was used to match the critical section loads to the ones in the global FE-model of the whole aircraft. Refined versions of the test model are used for computation of local strains, that are compared to the measured strains in the test, and local stresses that are used for fatigue crack growth predictions.

The static test has been successfully completed without any outcomes. Damage tolerance test considering both metallic and composite structural parts remains to be done.

SIMPLIFIED SPECIMEN TESTS

Prior to the component tests, a series of static, fatigue and damage tolerance development tests were performed on a simplified representation of the wing-fuselage joint, see Fig. 2.1-7. Two different designs were considered, one that was finally adopted at the upper wing side and one that was chosen for the lower wing side.

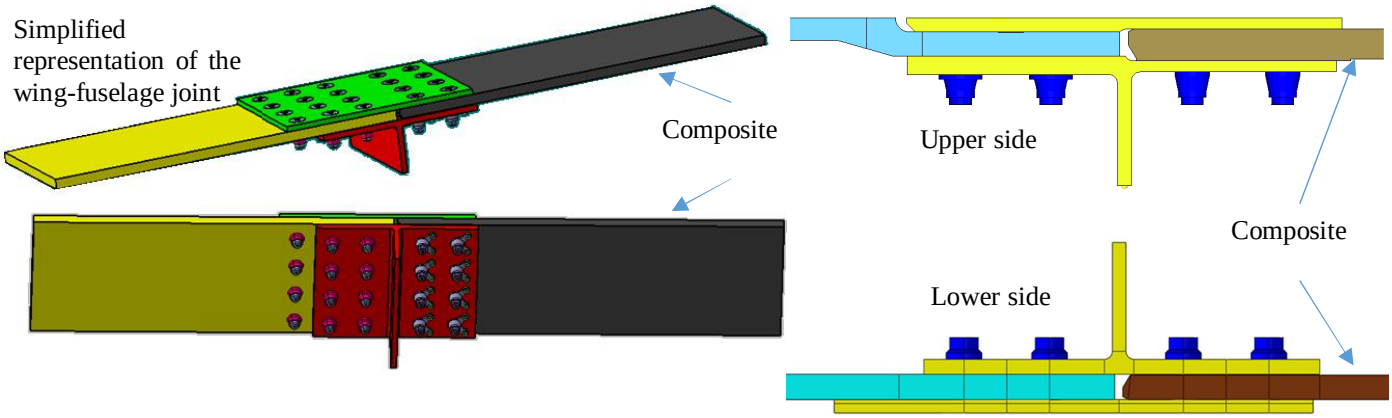

Figure 2.1-7. Simplified component test specimens of the wing-fuselage joint.

The work included studies of:

- Two different joint designs
- Two different aluminium materials AA7050 and AA2050
- Different fastener types and countersinking procedures
- Static tests to failure
- Fatigue tests to failure
- Damage tolerance fatigue tests with cracks growing from artificial defects in different scenarios in the skin plate, splice plate and in the T-profile
- Residual strength tests
- Strain measurements
- Detailed FE analyses of stresses and strains
- Fatigue and crack growth analyses

Figure 2.1-8 shows some examples of different types of failure that were obtained in the tests.

The tests and the analyses showed the capability of the final design to withstand >4 DSL in fatigue, >3 DSL in damage tolerance and a static strength of >220%DLL.

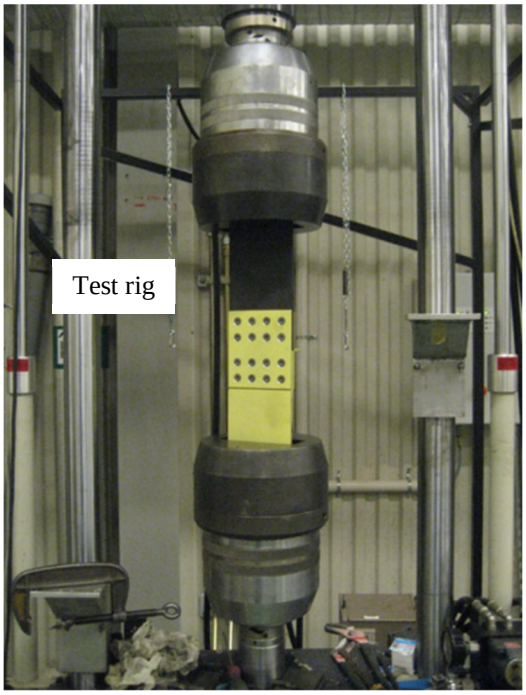

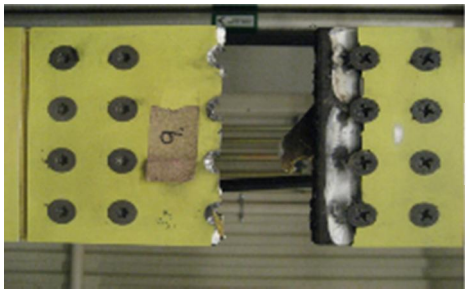

Fatigue failure
in the splice plate

Residual
strength test of
the skin plate

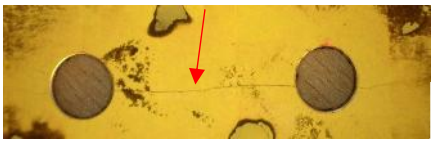

Fatigue cracks
in the skin plate

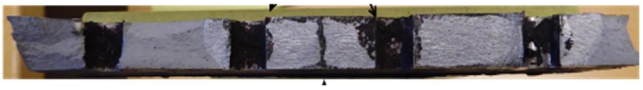

Damage tolerance test
of the skin plate radius

Static failure of
the composite
wing plate

Figure 2.1-8. Photos of the test rig and failed specimens.

Canopy sill to stringer

The component test “Canopy sill to stringer 01 joint at X_{85}=6330” is a certification test. The cause of test is upgraded criticality level and potential material change. Three test specimen will be used, one for a fatigue test and two for damage tolerance tests with artificial defects. Totally 18 defects are introduced in the two test specimens, mainly at fastener holes. The strains are measured by strain gauges at key locations and are compared to the results from an FE model of the test setup. Figure 2.1-9 shows the test set up where the load introduction points are indicated by the arrows. The test object is clamped at the opposite end and supported by rods at eight locations.

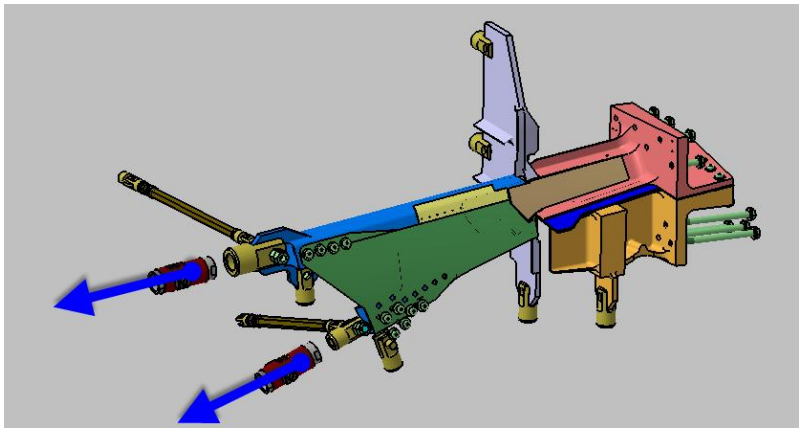

Figure 2.1-9. The component test object “Canopy sill to stringer 01 joint at X_{85}=6330”.

Figure 2.1-10. Photo of the test rig.

Stringer 01 behind X_{85}=8390

The component test “Stringer 01 joint behind X_{85}=8390” is also a certification test. The cause of test is upgraded criticality level and potential material change. Three test specimen will be will be used, both with and without artificially introduced defects.

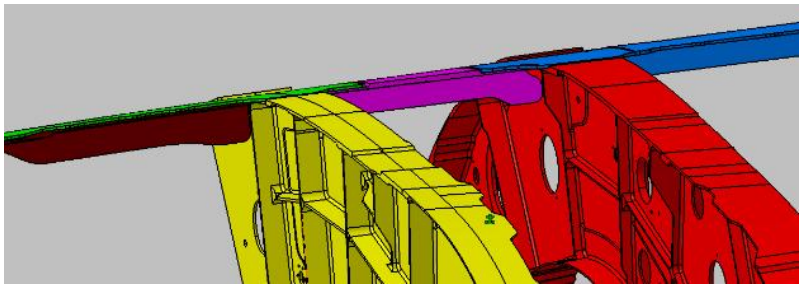

Figure 2.1-11. The component test “Stringer 01 joint behind X_{85}=8390”. The figure shows the design for the current area.

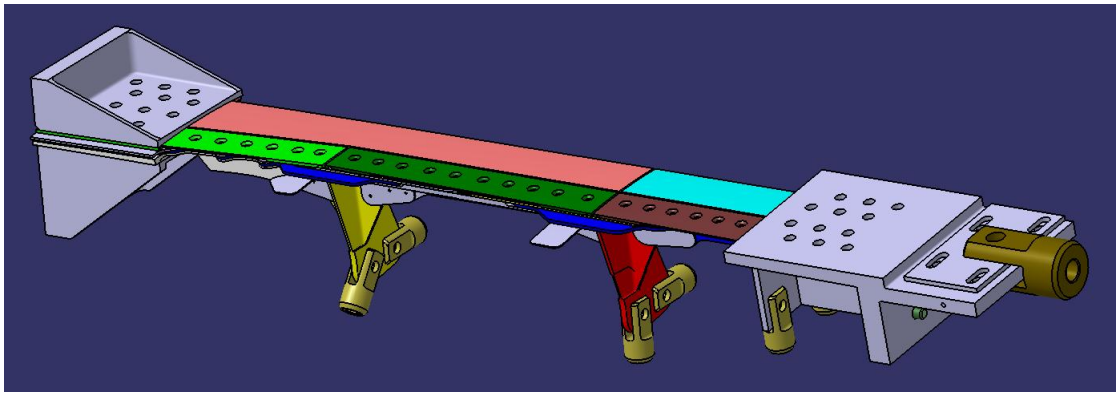

Figure 2.1-12. The component test object “Stringer 01 joint behind X_{85}=8390”.

Stringer 01 behind X_{85}=11770
The test represents the main stringer joint between the mid and the rear fuselage and is generally similar to the joint at X_{85}=8390.

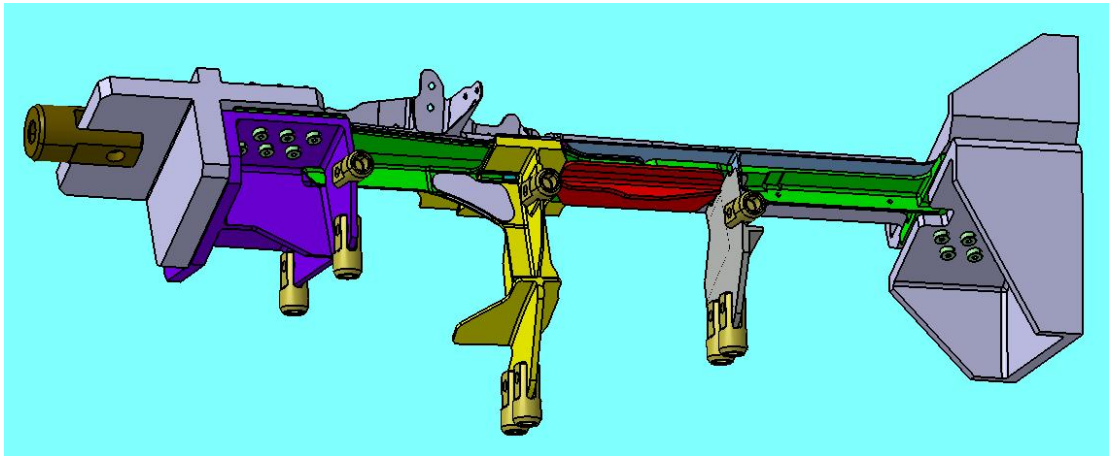

Figure 2.1-13. The component test object “Stringer 01 joint behind X_{85}=11770”.

2.2 Full-scale static test of Gripen E airframe

Björn Fredriksson, Martin Ekström, Saab AB

A full-scale static test of the Gripen E single seater airframe is currently being conducted. The purposes of the test are to:

- Verify static strength of the airframe
- Verify stress analysis of new design concepts (FE-models)
- Airworthiness approval of first flying unit
- Fast opening of flight test envelop
- Reduce strain measurements on flight test aircraft

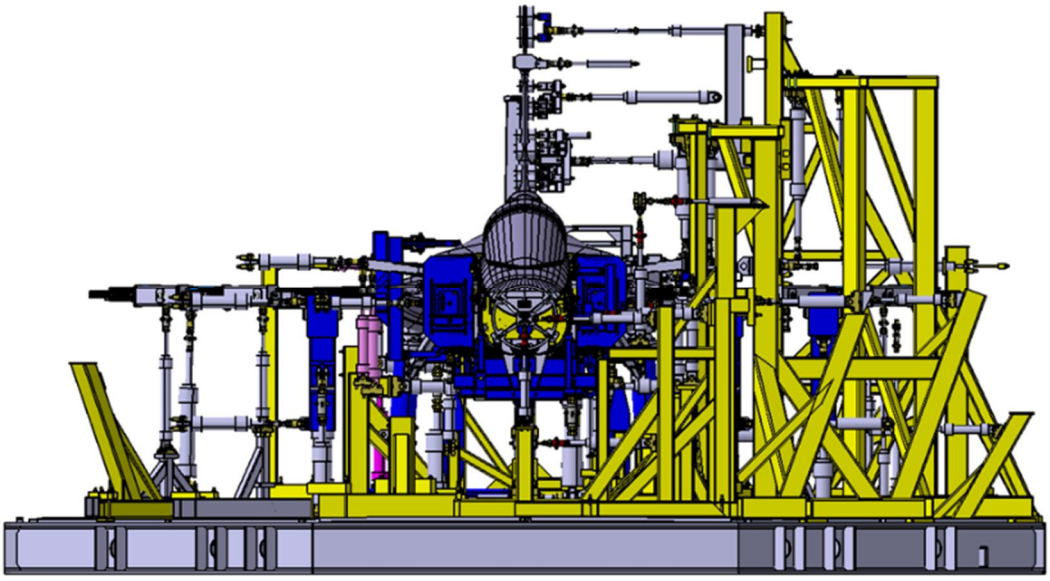

Figure 2.2-1. Static test set-up.

The test objectives are categorized according to Overall, Primary and Secondary objectives, see sections below.

Overall objectives
The overall objectives with the test are to:

- Open the envelope for test aircraft 39.8.
- Verify the static strength requirements.
- Verify the stiffness/load distribution of the global FE-model.

Primary objectives
The primary objectives are to verify the static strength of:

- The wing and the wing joints at 180 % LL.
- The fuselage at 150 % LL.
- The fin and the fin attachment towards the fuselage at 180 % LL.

Secondary objectives
Secondary objectives are to:

- Verify the static strength of the attachments on the wing for the following components:
    - Inner and outer flap
    - Inner and outer elevon
    - Pylon 1 L/R, Pylon 2 L/R, Pylon 3 L/R

- Verify the attachments on the fuselage for the following components:
    - Radar attachment
    - AAR
    - NLG

- MLG's
- Canards
- Air intakes
- Pylon 4, Pylon 5 L/C/R
- Engine

· Verify the rudder attachments on the fin.

The test object consists of an airframe representing the test aircraft with fuselage, wings and fin. Landing gears, control surfaces, weapon pylons, canards and engine are replaced by "dummies" and are tested separately.

The test is loaded by 126 load control channels for hydraulic actuators and 8 control channels for pressurized air in fuel tanks, cock-pit and air intakes and furnished with 2400 strain gauges for stress measurements.

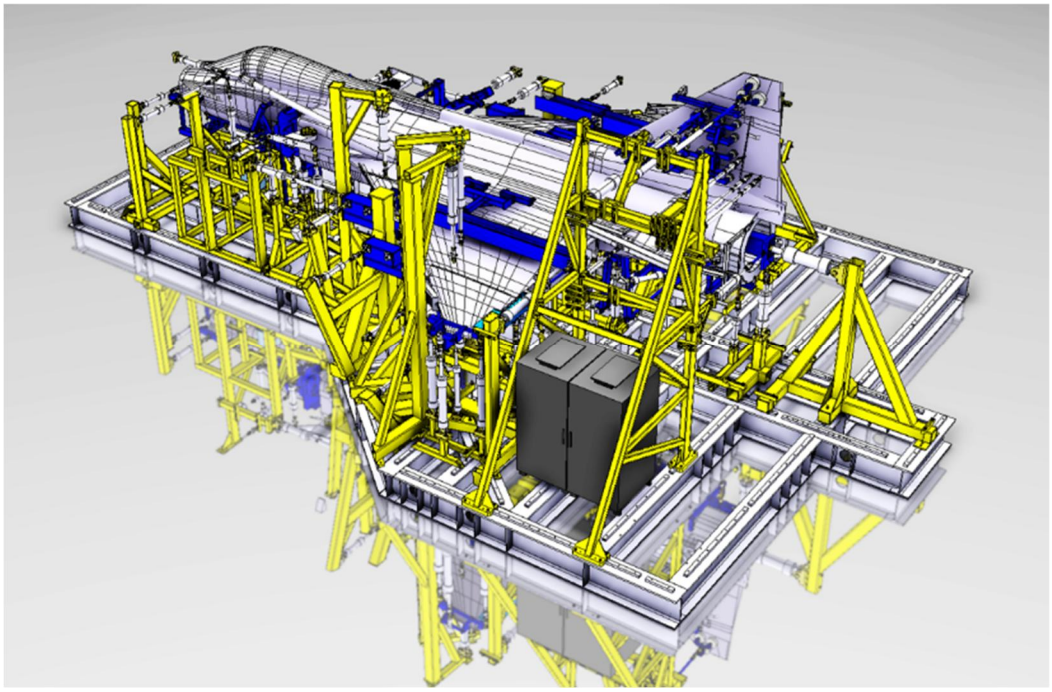

Figure 2.2-2. Static test setup, side view.

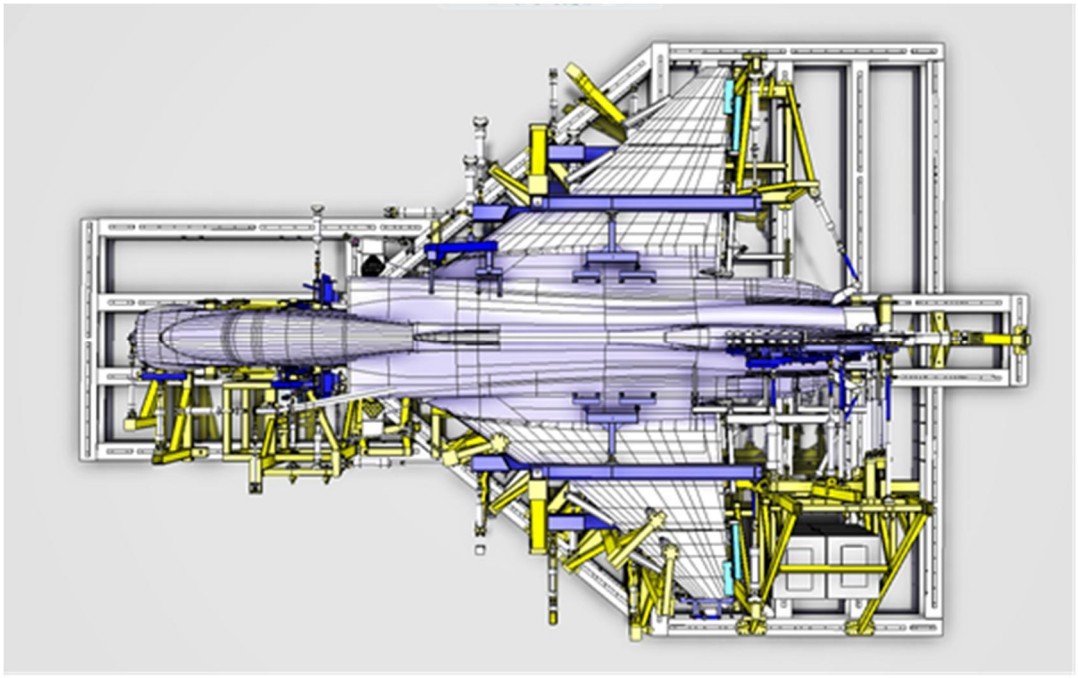

Figure 2.2-3. Static test set-up, top view.

Figure 2.2-4. Static test during assembly of airframe in test rig, top view.

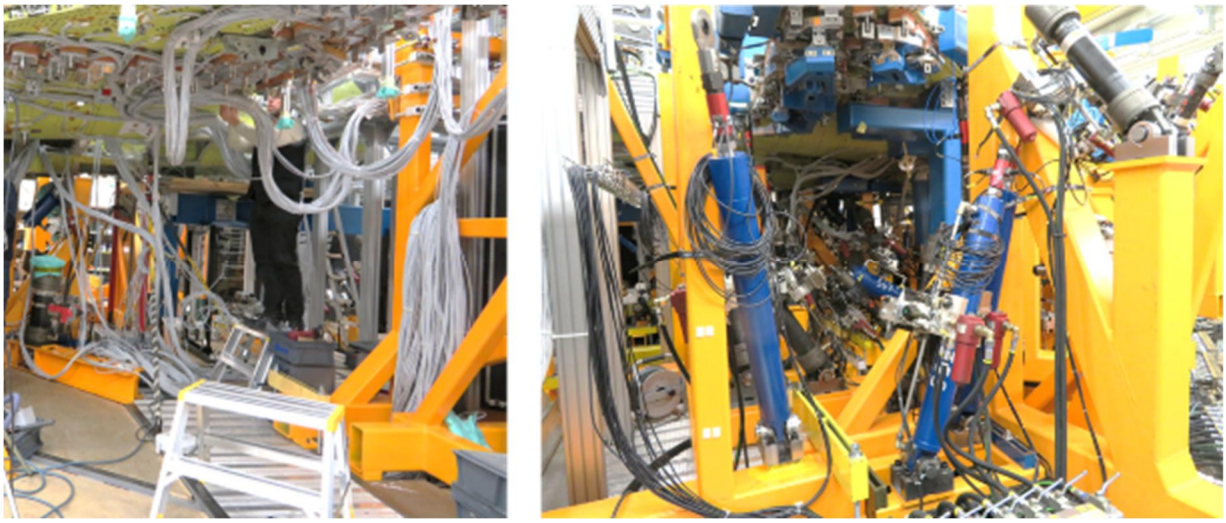

Figure 2.2-5 Static test during assembly of airframe in test rig, view from below.

The ordinary testing of the Full Scale Static Test has been successfully completed. This means that the test aircraft can in principle fly without restrictions on the airframe. Only some minor outcomes in the test have led to design updates for the serial version of Gripen E. What remains now is over testing of pylon attachments and hard landings.

2.3 Damage tolerance analysis of tests of canard wing pivots made of AA7050-T7451 and AA2050-T84

Zlatan Kapidžić Saab AB, Hans Ansell Saab AB

Introduction

Pivots for Gripen aircraft are made of AA7010-T7451 which is similar to alloy AA7050-T7451 which is the prime choice candidate to replace the no longer available AA7010 alloy. The use of AA7050 instead of the test verified pivot made of AA7010 is not considered to require any additional testing i.e. outcome from the previous test, consisting of canard wing, pivot and actuator arm, can be used to access damage tolerance capability of metal parts through similarity calculations.

An optional change to the less proven and less experienced alloy AA2050 requires renewed testing. The main reason for the need of testing is that the pivot is bi-axially loaded in critical sections. Biaxial stresses give rise to mixed crack modus which is a recognized weak property for aluminium-lithium alloys. A repeated test, in accordance with previous damage tolerance test is considered to be the best approach for certification purposes but a simplified development test in order to challenge AA2050 to be a candidate alloy. The accomplished test was a comparable test where simplified test objects (part of the pivot, no wing) was tested in two embodiments, manufactured in AA2050 and AA7050 respectively.

The aim of the test programme was to show if there were any differences in the damage tolerance capability of a generic canard wing pivot manufactured in aluminium-lithium alloy AA2050-T84 compared to a pivot made of AA7010/7050 alloys. Reference [1] describes the description and the outcome of the testing. The current paper also includes the results of the crack growth and residual strength analyses that were performed in the test evaluation work.

Test setup

Totally 4, geometrically identical, specimens have been manufactured from thick plate material and all 4 have been tested with the same initial defect size. Two of the specimens are made of AA2050-T84 and two are made of AA7050-T7451 alloy. The specimens are numbered as shown in Table 2.3-1.

Spec #	Material	Fatigue loading	Residual strength test loading
#1	AA2050-T84	Bend/Twist	Bend
#2	AA7050-T7451	Bend/Twist	Bend
#3	AA2050-T84	Bend	Bend
#4	AA7050-T7451	Bend	Bend

Table 2.3-1. Specimen numbering and applied load type.

The specimen geometry is a thick-walled tube with two rectangular end sections for load introduction see Fig. 2.3-1. The test area is located in between the end sections and contains a circumferential radius where a semi-circular artificial defect is introduced on top side of the specimen by electro spark machining. The specimens are in all cases installed so that the defect is located on the top side of the specimen, where the tensile stresses are present. This means that the crack front is oriented in L-S direction at the surface and in L-T direction in the deepest point in the specimen interior.

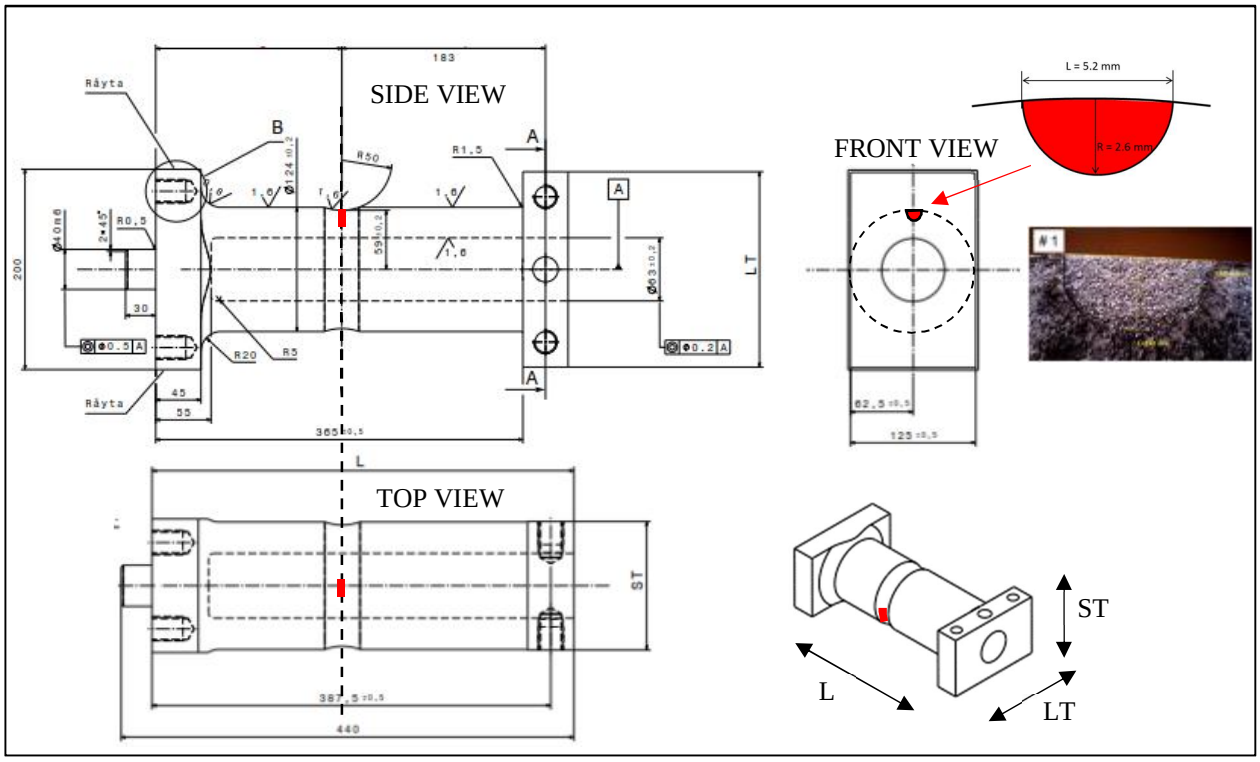

Figure 2.3-1. Test specimen geometry and position of the artificial crack

The specimens are mounted to a wall in one end and at the other end the loads are introduced by means of two hydraulic load actuators that are connected to the floor. Both actuators apply a pulling force, giving bending moment or/and twisting moment in the test section depending on the combination of the applied actuator forces. Two of the specimens were fatigued in bending/twisting, with shear to bending stress ratio of $t/s = 0.20$, and two in pure bending. residual strength tests (to failure) were performed in pure bending as stated in Table 2.3-1.

A test spectrum was used where insignificant load cycles were eliminated in order to reduce testing time. The elimination was done using the max principal stress in the critical section as the steering stress component. The derived elimination vector was thereafter applied to the individual bending (Mb) and torsion (Mt) moment sequences. The final number of load states in the test sequences was 83,350 which represent 800 h.

During all fatigue test, the crack growth was measured every 800 flh by means of eddy current and a loupe and in some cases penetrant was used. The post mortem measurements of the final crack sizes were performed in a microscope.

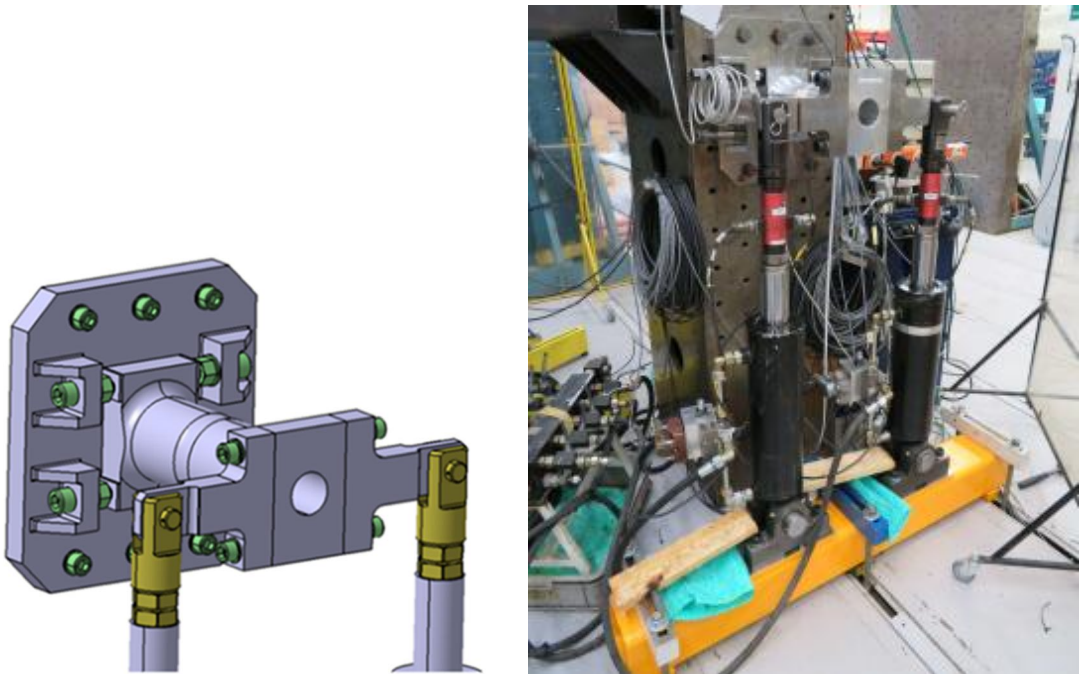

Figure 2.3-2. Test specimen in loading arrangement

Test results

The crack in specimen #2 (AA7050) propagated at an angle of about 10 degrees to the axial direction, which coincides with its growth perpendicular to the direction of the max principal stress even though the shallow radius ditch constituted a certain limitation of deviation. The crack in specimen #1 (AA2050) propagated initially in the same way but turned almost 90 degrees at the end of it growth, se Figure 2.3-3. In both specimens #3 and #4 the cracks grew at 0 degrees, consistent with pure bending. The crack propagation for both torsion/bending and pure bending was recorded and is shown in the diagram in Figure 2.3-6.

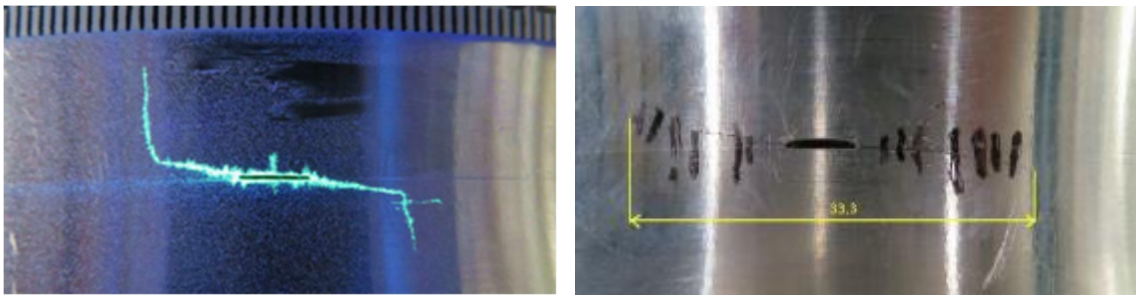

Figure 2.3-3. Crack propagation directions in specimen #1 (AA2050) and #2 (AA7050)

Specimens #1 and #2 were subjected to a residual strength tests to 125% limit load under combined torsion/bending with no failure. Due to limited actuator capacity the subsequent failure tests were done under pure bending load. The AA2050 specimen #1 was loaded to the maximum actuator capacity of 220% limit load but did not fail. The AA7050 specimen #2 failed at 217% limit load.

Specimens #3 and #4 (with longer cracks than in specimens #1 and #2) were also subjected to a residual strength test to 125% limit load (pure bending) with no failure in the test section. The AA7050 specimen #4 failed at 160% limit load.

Specimens #1 and #3 made of AA2050 alloy were cut to be able to be pulled apart and showed a significant crack branching behaviour towards L-direction, see Figure 2.3-4. Specimens #2 and #4 made of AA7050 alloy had a plane crack surface structure in LT-ST plane, Figure 2.3-5.

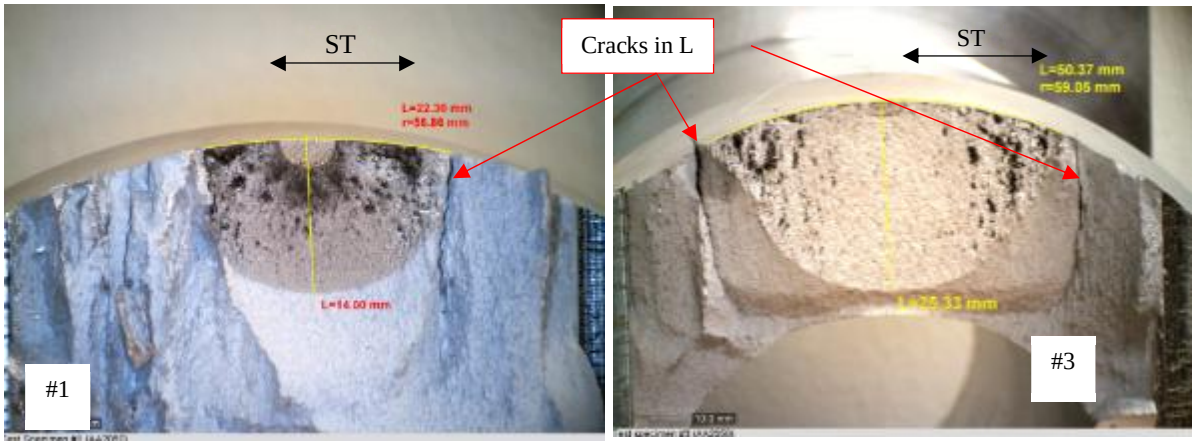

Figure 2.3-4. Broken specimens #1 (AA2050) and #3 (AA2050).

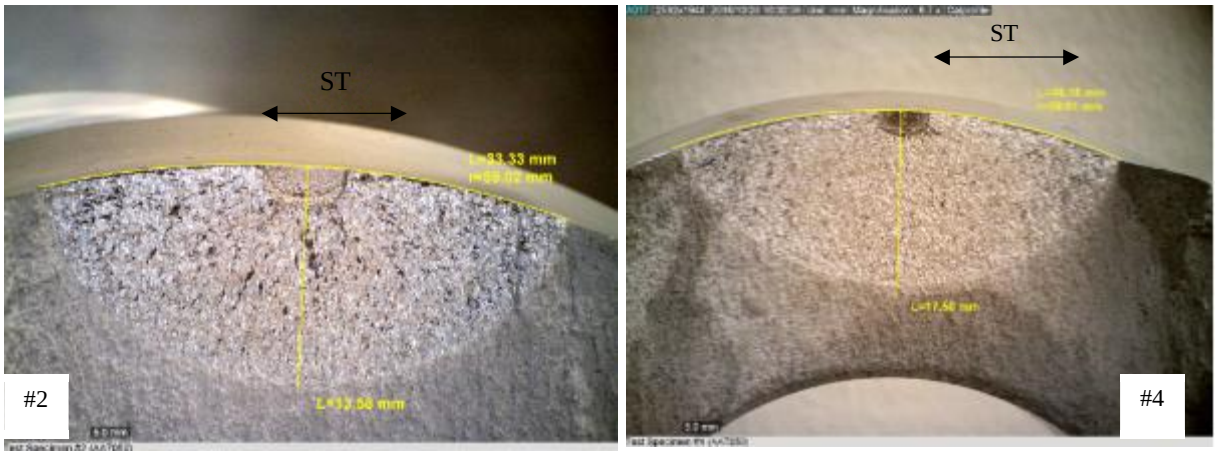

Figure 2.3-5. Broken specimens #2 (AA7050) and #4 (AA7050).

The apparent high residual strength of AA2050 specimens was observed in other tests as well, see sections 2.4 and 2.5, and is believed to be the result of the crack turning effect in L-S loading. Relatively large cracks oriented in ST direction have a strong tendency to turn towards L direction despite the fact that the load is applied in L direction. Because of the turning, the crack driving force is reduced, resulting in an apparently high residual strength.

Crack growth calculations

The crack growth software AFGROW has a model for crack growth in thick walled tubes for bending but not for twisting. Considering that the shear stress is small relative to the bending stress in the combined load case, the analyses were based on the pure bending model but with the principal stress for the combined case. In all crack growth calculations, the correction for the notch is introduced by means of the beta correction capability in AFGROW. Load sequence interaction effects were disregarded. The predicted and tested crack lengths versus the number of flight hours are shown in Figure 2.3-6.

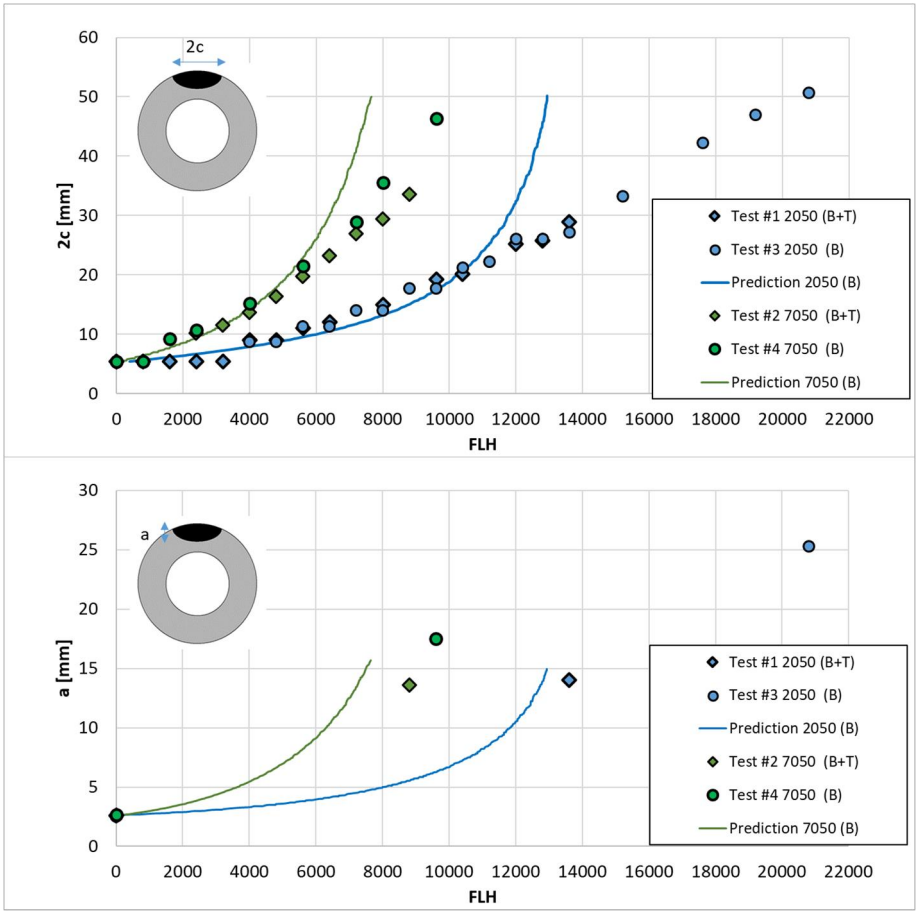

Figure 2.3-6. Predicted and measured crack growth.

The correlation between the predictions and measurements is fairly good for 2c<20 mm. At larger crack lengths the deviation is probably caused by the retardation effects. Both the tests and the analyses show about 1.7 times slower crack growth in AA2050.

Residual strength calculations

The residual strength calculations were performed at max applied test load using the geometry functions extracted from AFGROW at final crack lengths. The mode I stress intensity factors (SIF) at the surface crack tip ,K_I^c, and at the deepest crack point, K_I^a, were calculated and normalized with the plane stress fracture toughness K_C (in L-S direction) and plane strain fracture toughness K_{IC} (in L-T direction) respectively, see Figure 2.3-7. If the (stress intensity factor)/(fracture toughness) ratio is greater than one, as it is for specimens #1, #2 and #4, failure should be expected. Yet only specimens #2 and #4 actually failed. The reason that specimen #1 has not failed is believed to be crack turning towards L-direction.

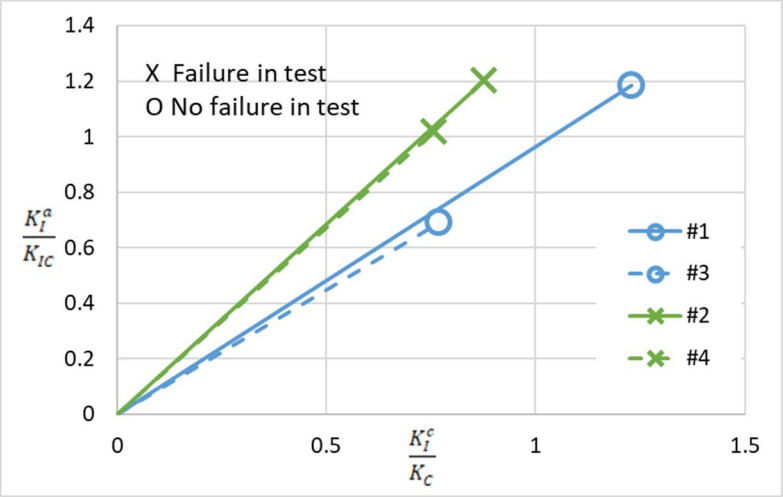

Figure 2.3-7. Mode I stress intensity factor to fracture toughness ratios.

The SIFs in Figure 2.3-7 are calculated assuming a planar crack in all cases. An alternative approach is to assume that the crack in specimen #1 has deflected an angle of 90 degrees. Defining an effective stress intensity factor k_{eff} for a crack turning at angle α as

$$k_{eq} = \sqrt{(1-\nu^2)k_I^2 + (1-\nu^2)k_{II}^2}$$

where ν is Poisson's ratio and k_I and k_{II} are the stress intensity factors of the turned crack

$$k_I = cos^3\left(\frac{\alpha}{2}\right)K_I$$
$$k_{II} = sin\left(\frac{\alpha}{2}\right)cos^2\left(\frac{\alpha}{2}\right)K_I$$

k_{eff} is calculated as $k_{eff} = 0.474 \cdot K_I$ for a turning angle of 90 degrees. Assuming that k_{eff} is a relevant quantity for failure prediction of a deflected crack and recalculating the ratios for specimen #1 $\left(\frac{k_{eff}}{K_{C(S-L)}}, \frac{k_{eff}}{K_{IC(T-L)}}\right) = (0.7,0.6)$ the conclusion is that specimen #1 will not fail.

Conclusions

The tests and the analyses have shown that cracks from artificial defects grew approximately 1.7 slower in AA2050 than in AA7050 canard wing pivot specimens. A significantly higher residual strength was observed in the AA2050 tests than calculated assuming Mode I planar crack growth at failure. The reason is believed to be reduction of the stress intensity factor due to crack turning.

References

[1] Ansell, H. A Review of Aeronautical Fatigue Investigations in Sweden During the Period April 2015 to March 2017, ICAF 2017 Proceedings of the 36th Conference, Nagoya, Japan.

2.4 Damage tolerance analysis of spectrum loaded notched geometries made of AA7050-T7451 and AA2050-T84

Zlatan Kapidžić Saab AB, Hans Ansell Saab AB

Crack growth in plates made of Aluminum-Lithium alloy AA2050-T84 has shown different behaviour compared to AA7050-T7451, concerning the crack growth rate and the character of the crack surfaces. These results have been obtained by testing of generic specimens, designed for derivation of sizing data, which do not contain stress concentrations that are commonly present in aircraft structure. The aim of this testing series is to evaluate the crack growth rate, the residual strength and the crack growth characteristics for the two materials, using specimens which include structure like stress concentrations. The results shall also be used to evaluate the predictions produced by the crack growth and residual strength models used for damage tolerance sizing.

Specimens

The test series include spectrum and residual strength testing of two types of pre-cracked specimens:

- Plate with radius, surface crack in radius, type (R), 12 specimens
    - 4 specimens in AA 7050-T7451
    - 8 specimens in AA 2050-T84
- Plate with hole, corner crack in hole, type (H) , 10 specimens
    - 4 specimens in AA 7050-T7451
    - 6 specimens in AA 2050-T84

see, figures below.

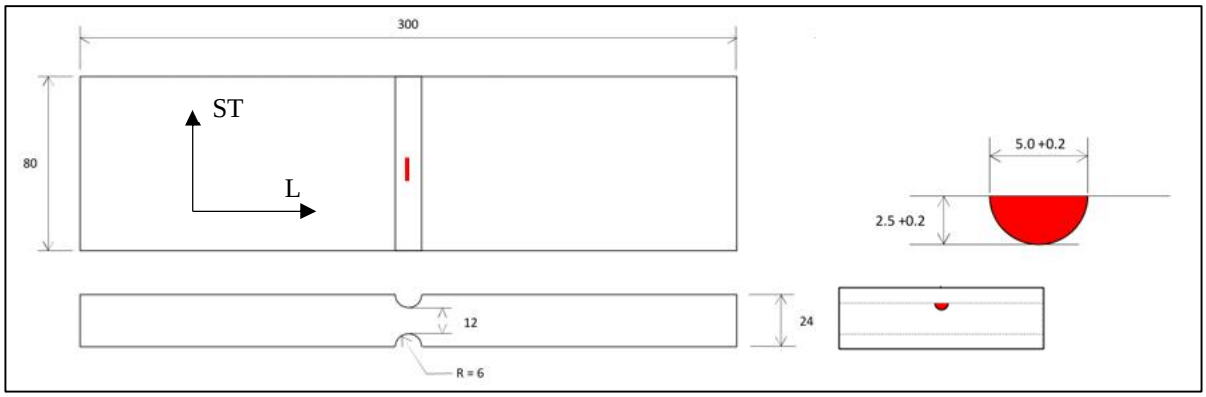

Figure 2.4-1. R-type specimen with a surface crack.

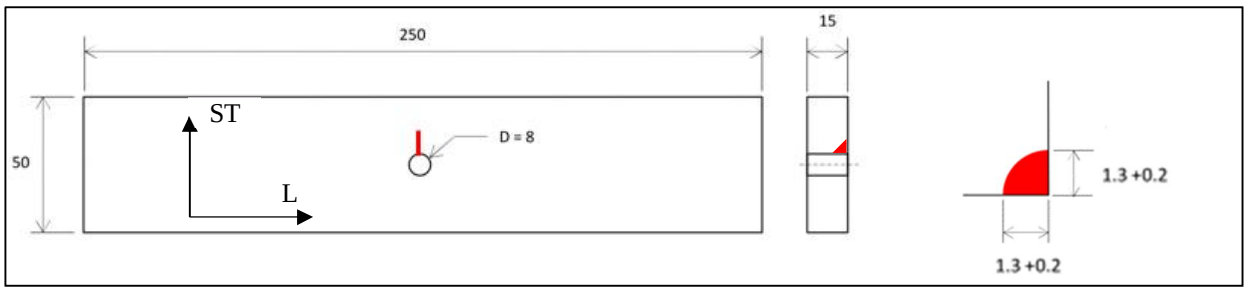

Figure 2.4-2. H-type specimen with a corner crack.

Each individual specimen is given a name written according to a designation code:

Specimen type Material: Specimen number
For instance R2:1 means, R-type specimen made of 2050, number 1.

Load Spectra
Two different load spectra were used in this testing series, UVKB and BFKB.

Wing spectrum UVKB:	Asymmetric, tensile dominant load spectrum, which represents the load variation in the lower wing attachment.
Fin spectrum BFKB:	Symmetric load spectrum which represents the load variation in the fin attachment.

Test arrangement and measurements
The testing is performed in a servo-hydraulic testing machine. Specimen types R and H are simply clamed at both ends in the loading frames of the machine. Specimen type P is clamped at one end while the hole is loaded on the other end by a steel pin, which is connected to the loading frame via a loading fork.

Crack measurements were performed in order to establish the relation between the crack length and the number of flight hours passed. For specimen type R, both crack tips are visible and are measured. In specimen types H, only the surface crack tip is measured. The cracks are frequently photographed during the cycling and measurement of the crack length is performed a posteriori in the photographs.

Test procedure
The specimens were fatigued for more than 2DSL until the cracks grew through the thickness of the plates. After that, the specimens were pulled to failure and the failure load was recorded for the purpose of residual strength evaluation.

Crack growth calculations
Fatigue crack growth calculations using AFGROW [1] have been performed for the purpose of comparison with the test results. AFGROW appropriate classic stress intensity factors have been used. For R-specimens the correction for the stress concentration was introduced by means of weigh function. Crack growth retardation by load sequence effects was considered using Closure Model [1]. The residual strength calculation was based on classical stress intensity solutions.

Results
The main test results that are compared between the materials and to the calculations are crack length as function of number of flight hours and the residual strength. The comparisons are performed below for R and H specimen types and photographs of the surfaces of the broken specimens are shown.

Crack growth tests and calculation results

R-TYPE SPECIMENS

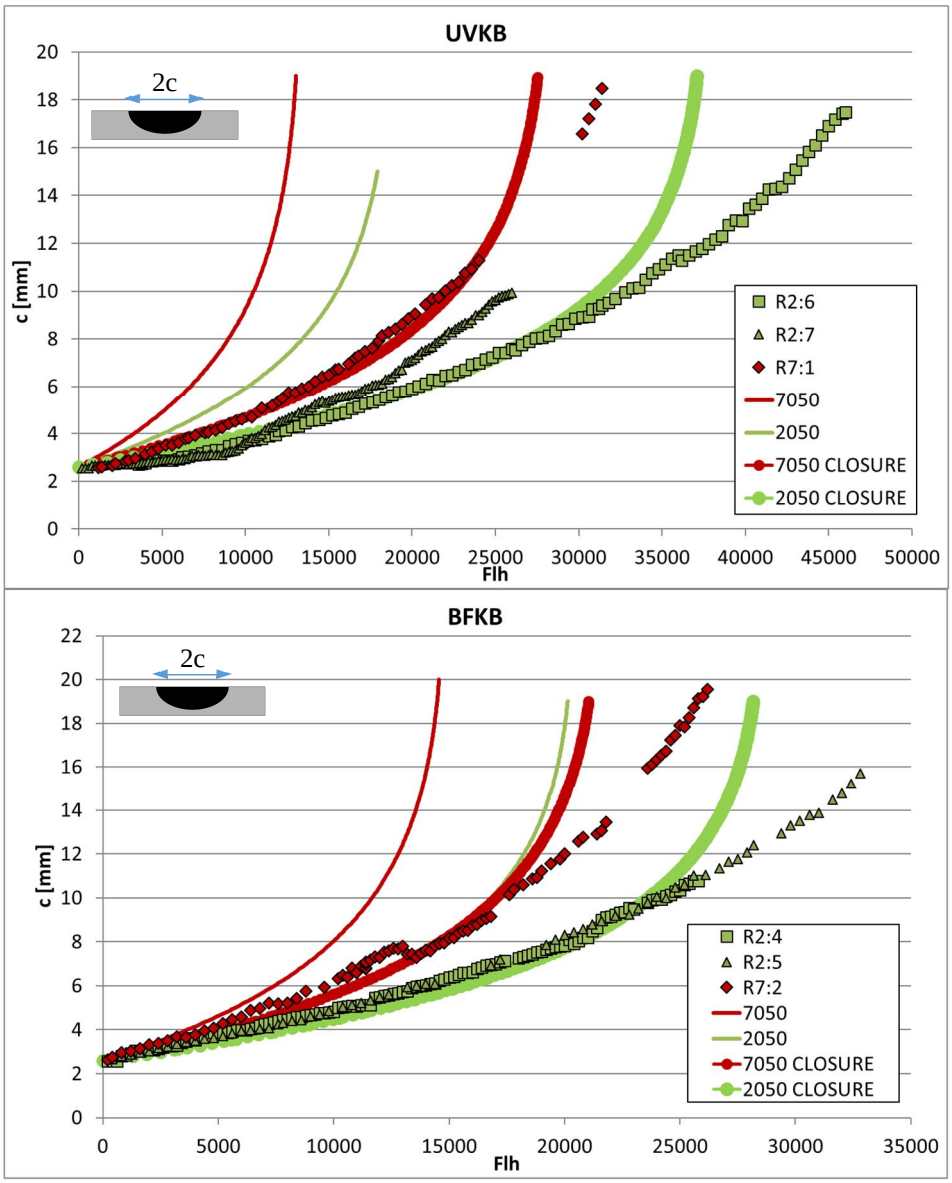

Figure 2.4-3. Surface crack length, UVKB and BFKB spectra, R-type specimen, test vs prediction (with and without closure).

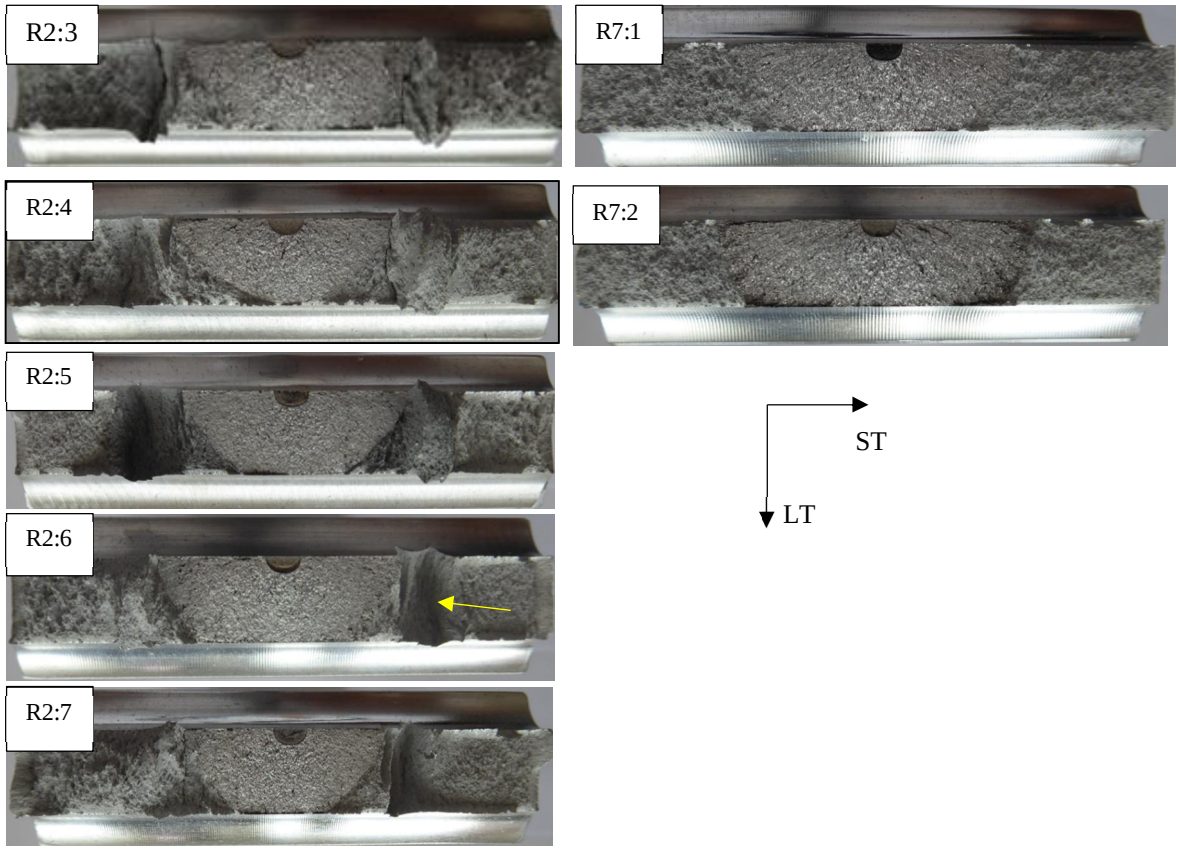

Figure 2.4-4. Crack plane of R-specimens after failure.

Comments regarding R-type specimens:

- Stable slow crack growth was achieved in all specimens and the cracks grew through the thickness of the.
- In 2050 specimens the cracks grew 1.3-1.5 times slower than in 7050 specimens.
- The predictions generally conservative compared to test results if retardation effects are disregarded. Accounting for the retardation gives good correlation to the test until the crack grows through the thickness.
- Significant crack turning towards L-direction is observed (yellow arrow in Figure 2.4-4) in the residual fracture in 2050 specimens and no such crack turning is seen in 7050 specimens.

H-TYPE SPECIMENS

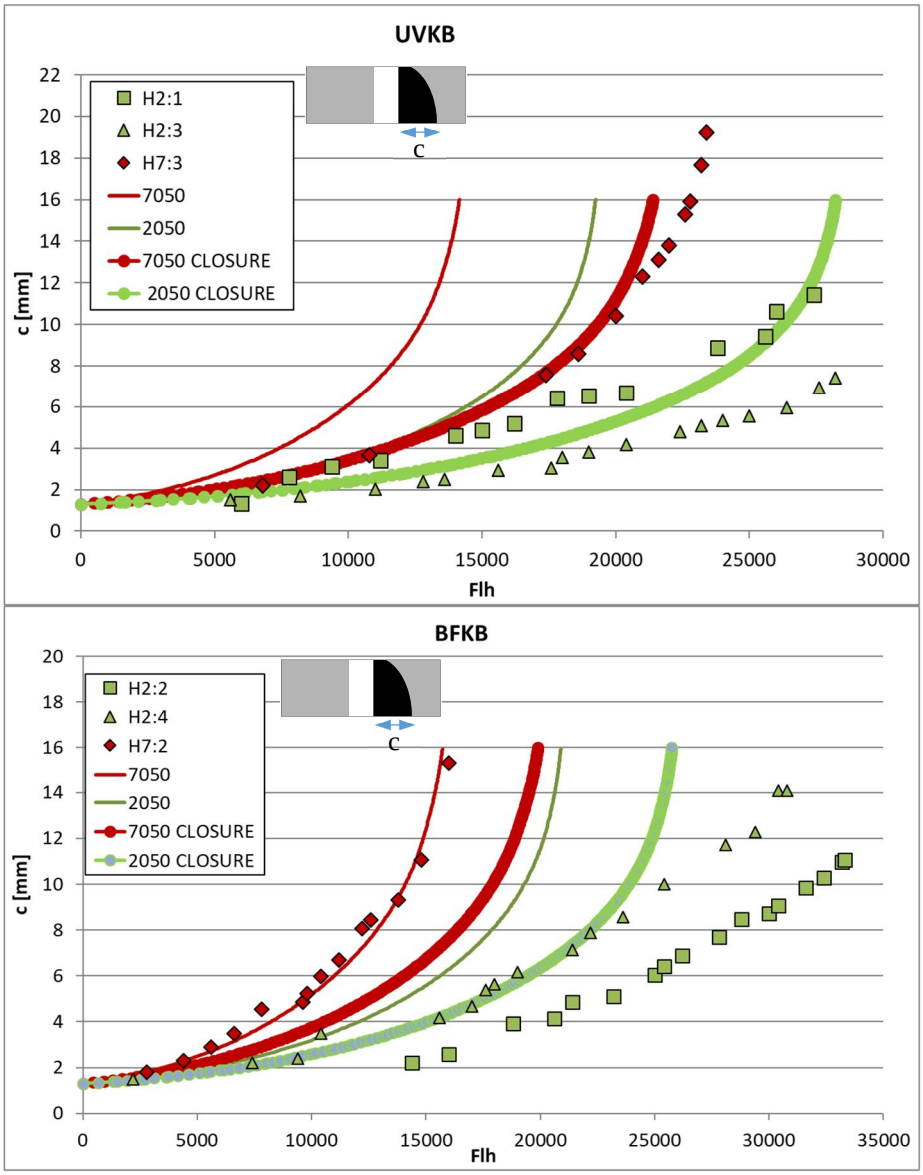

Figure 2.4-5. Surface crack length, UVKB and BFKB spectra, H-type specimen, test vs prediction (with and without closure).

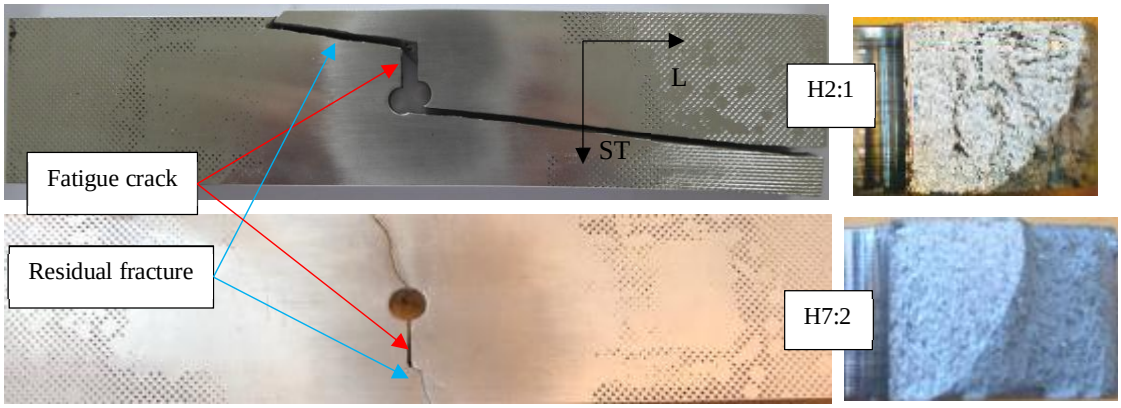

Figure 2.4-6. Cracking of H-specimens after failure.

Comments regarding H-type specimens:

- Stable slow crack growth was achieved in all specimens and the cracks grew through the thickness of the specimens.
- In 2050 specimens the cracks grew 1.3-1.9 times slower than in 7050 specimens.
- The predictions were conservative compared to test results for UVKB spectrum if the retardation was disregarded and good correlation was obtained with retardation. The same thing can be said about 2050 with BFKB. For 7050 with BFKB spectrum the predictions with no retardation were close to the measured results and the retardation model over predicted the results.

Residual strength tests and calculation results

As discussed in section 2.3 of this document and as shown in 2.4-4 and 2.4-6, cracks in L-S loading in AA2050 have a tendency to turn towards L-direction. It has been shown in section 2.3 that assuming planar mode I cracking at failure yields conservative estimations of the residual strength in such cases. An alternative approach was suggested, that the effective stress intensity factor for a crack deflecting at 90 degrees $k_{eff} = 0.474 \cdot K_I$ should be used instead of K_I. Both of these approaches are evaluated for AA2050 next. Failure is assumed to take place when $K_I = K_{IC}$ (L-S direction) in planar mode I approach and $k_{eff} = K_{IC}$ (S-L direction) in the alternative approach. Figures 2.4-7 and 8 show the (stress intensity factor)/(fracture toughness) ratios as function of net-section stress normalized by R_{p02}.

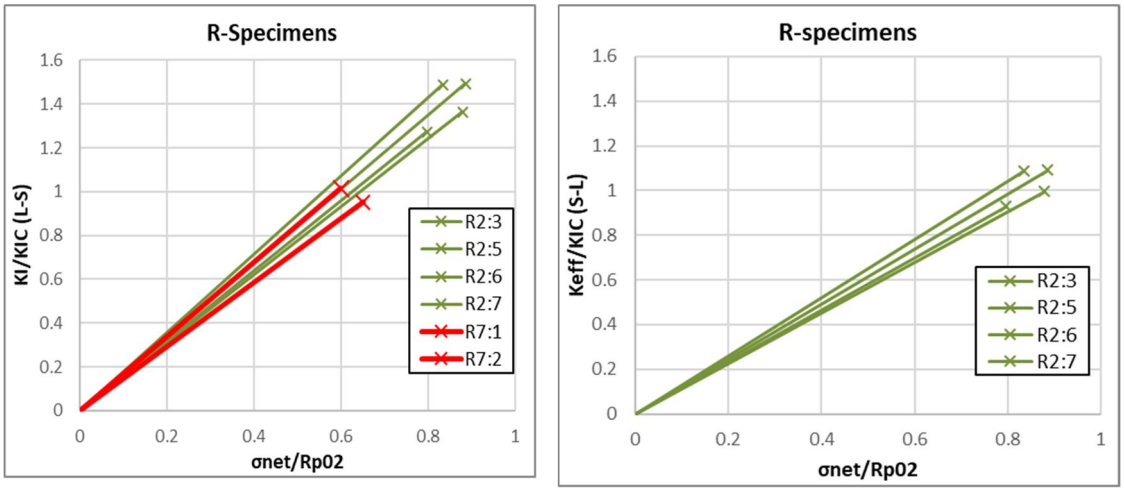

Figure 2.4-7. (Stress intensity factor)/(fracture toughness) ratios for R-specimens AA7050 and AA2050 at failure load.

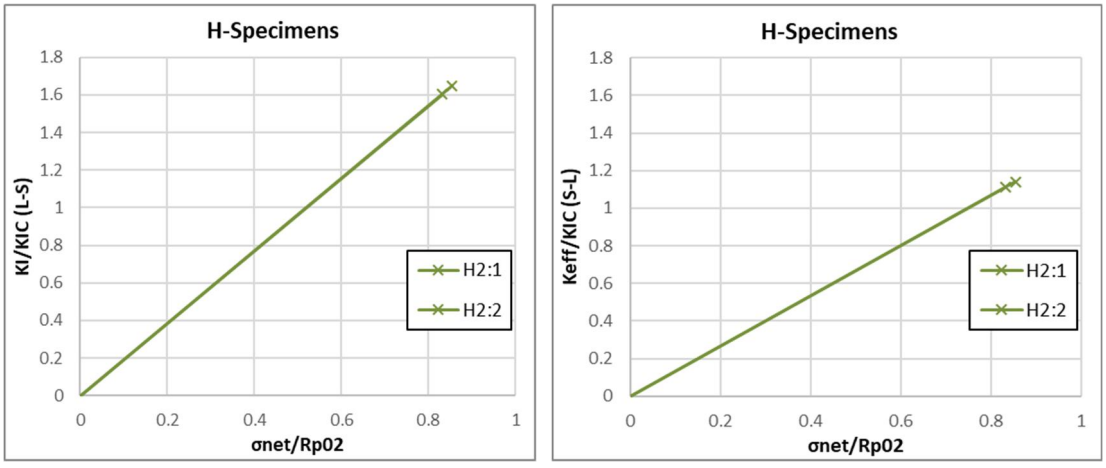

Figure 2.4-8. (Stress intensity factor)/(fracture toughness) ratios for H-specimens AA2050 at failure load.

The figures above confirm the findings from section 2.3, that assuming a branched crack in L-S loading of AA2050 results in better estimation of the residual strength. The planar mode I residual failure assumption gives good predictions for AA7050 but conservative for AA2050.

Conclusions

- Notched AA2050-T84 and AA7050-T7451 plate specimens with defects were fatigued in spectrum loading and loaded to failure.
- In all compared cases, the cracks grew slower in AA2050-T84 than in AA7050-T7451. The crack growth rate depends on the specimen type, the spectrum and the crack length, but can be roughly estimated to be 1.3-1.9 times slower in AA2050-T84 than in AA7050-T7451.
- The predictions of the crack growth were conservative compared to the test outcome if the retardation effects are disregarded.
- Assuming planar mode I residual failure resulted in good predictions of L-S residual strength of AA7050 but underestimated it for AA2050. In the latter case a branched crack assumption gave much better results.

References

[1] AFGROW. User's guide and technical manual. Version 5.03.01.21. August 2017.

2.5 Residual strength analyses and testing of flange like specimens in AA7050-T7451 and AA2050-T84

Zlatan Kapidžić Saab AB, Hans Ansell Saab AB

A study of crack growth in residual strength tests in specimens made of AA2050-T84, see section 2.4, shows that cracks, originally oriented in ST-direction, have a tendency to turn towards L-direction during residual cracking when loaded in L-direction. The study also shows that neglecting the crack turning behavior results in overestimation of the stress intensity factor and therefore a conservative prediction of the failure load. The specimens studied in section 2.4 had generic geometrical shapes, plate with a hole and plate with double radii.

This document presents a complementary study, where the residual strength of a typical portion of a generic bulkhead flange geometry is tested and analyzed. The goals of the study are:

- to experimentally investigate the occurrence of the crack turning behavior in a geometry which is closer to airframe applications than the geometries in section 2.4
- to evaluate the accuracy of the currently used analytical sizing methods for residual strength

Specimens

This test series includes specimens made of both AA2050-T84 and AA7050-T7451, with two different geometries taken out in three material directions. The first geometry is a plate with two radii in the middle of its length and ten holes with a diameter of D = 6 mm, symmetrically place around a stiffener, see Fig 2.5-1. The second geometry is the same but without holes. The specimens are taken out of a 140 mm thick plate and oriented with their lengths in three different directions, L (4 specimens for each material), LT (2 specimens for each material) and

L-LT 45° (2 specimens for each material), and the width of the plate being in ST direction as shown in Fig. 2.5-2. Each specimen was equipped with one 15 mm long through-crack like artificial defect, manufactured using electro machine sparking process. The defects were placed in the middle of one of the radii and oriented in the ST direction, as indicated in Fig. 2.5-1 with a red line. 2.5-Table 1 summarizes all specimen designations, material, orientation of the specimen and geometry type.

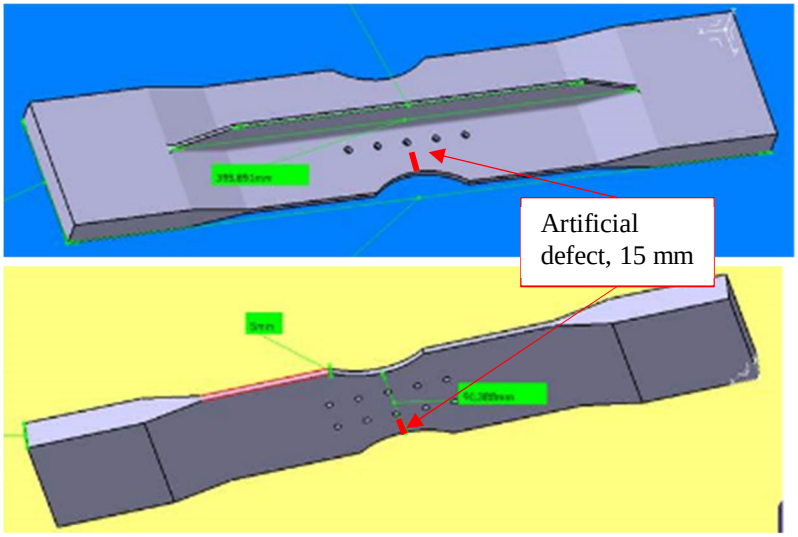

Figure 5.2-1. Test specimen geometry.

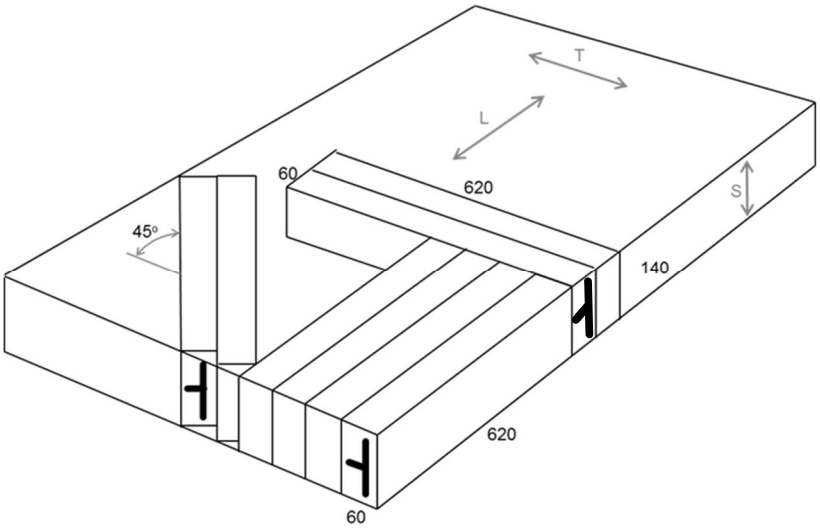

Figure 2.5-2. Specimen directions.

Spec	Material	Specimen length direction	Force-defect direction	Geom
A1	AA2050-T84	L	L-S	Holes
A2				Holes
A3				No holes
A4				No holes
B1		LT	T-S	No holes
B2				No holes
C1		L-LT 45°	(L-LT 45°)-S	No holes
C2				No holes
D1	AA7050-T7451	L	L-S	Holes
D2				Holes
D3				No holes
D4				No holes
E1		LT	T-S	No holes
E2				No holes
F1		L-LT 45°	(L-LT 45°)-S	No holes
F2				No holes

Table 2.5-1. Specimen summary.

Test procedure

The tests were performed in a hydraulic tensile machine. All specimens were first exposed to pulsating tensile cycling on a relatively low load level in order to initiate some fatigue crack growth at the tip of the defect. Next, each specimen was loaded to complete failure with (with time) linearly increasing tensile force. The applied load signal and the resulting force from the load cell, as functions of time, were recorded.

A recording film camera was set up to monitor the specimens during loading, especially the area containing the crack. A voltmeter, which was calibrated to the applied force, was visible in the camera frame during the experiments. The idea was to use the film, in correlation with the resulting force from the load cell, to determine the applied force at which the crack propagation started. Besides that, the film was used to document the direction and the propagation of the crack growth.

Analysis

Normally, the analytical approach for assessment of the residual strength of cracked structures is based on comparison of the mode I stress intensity factor of a planar crack with the associated fracture toughness in the same loading and crack directions. As shown in section 2.4, this approach predicts the residual strength of AA7050-T7451 components quite well. On the other hand, the predictions for AA2050-T84 in L-S direction were conservative, which is believed to depend on the crack turning behavior observed in this alloy. Assuming a branched crack improves the predictions significantly. In this section, both planar and branched assumptions are considered for L-S direction in AA2050-T84. The remaining part of this chapter presents the calculation of the stress intensity factors and fracture toughness, and the next chapter presents the analyses and test results.

Mode I stress intensity factor

The stress intensity factors were computed using a solid FE model of the whole specimen geometry and are

- For the specimens with hole:

$$K_I = \frac{F}{(W - 2D)t + ht_h}\sqrt{\pi \cdot a} \cdot 1.2980 \qquad (2.8\text{-}1)$$

- For the specimens without hole:

$$K_I = \frac{F}{Wt + ht_h}\sqrt{\pi \cdot a} \cdot 1.2980 \qquad (2.8\text{-}2)$$

where
F is the applied force
a = 15 mm is the crack length
W = 90 mm is the specimen width
D = 6 mm is the hole diameter
t = 5 mm is the specimen thickness
h = 30 mm is the stiffener height
t_h = 3 mm is the stiffener thickness.

Effective stress intensity factor for deflecting cracks

In the case of crack deflection by an angle α, the effective stress intensity factor of the branched crack can be expressed as

$$k_{eff} = \sqrt{(1 - v^2)k_I^2 + (1 - v^2)k_{II}^2} \qquad (2.8\text{-}3)$$

where v is the Poisson ratio, k_I and k_{II} are the stress intensity factors of the branched crack which can be expressed as [1]

$$k_I = cos^3\left(\frac{\alpha}{2}\right)K_I \qquad (2.8\text{-}4)$$

$$k_{II} = sin\left(\frac{\alpha}{2}\right)cos^2\left(\frac{\alpha}{2}\right)K_I \qquad (2.8\text{-}5)$$

Combining the equations and assuming v = 0.32 and α = 90° we get

$$k_{eff} = 0.474 \cdot K_I \qquad (2.8\text{-}6)$$

Fracture toughness

Fracture toughness (K_{IC}) values, which are normally used for sizing, vary depending on the material, the loading-crack direction and the billet size. The apparent fracture toughness for a certain geometry also depends on the plate thickness due to the actual stress/strain state at the crack tip [1]. Here, we adopt the frame work of calculating the apparent fracture toughness K_{crit} as a function of the plate thickness as outlined in [2]. Failure is assume to take place when $K_I = K_{crit}$ in planar mode I approach and when $k_{eff} = K_{crit}$ in deflecting crack approach. Note that K_{crit} is taken in the relevant direction depending on the specimen.

Results

Test results

The test results consist of registered applied force over test time specimen photographs and films of the tests.

The main findings are:

- No observable fatigue crack growth at the tip of the defects after pre-cycling, in any of the specimens.
- During monotonic loading to failure, the cracking took place gradually, which can be seen in the films. It is clear that cracks starts to grow long before the maximum load is applied. Two methods were used to determine the applied load at initial crack propagation:
    - Visual observation of the start of the initial crack propagation in the film, correlated to the force reading on the voltmeter.
    - Reading of the distinct kinks on the load-time curve registered by the load cell.
- Depending on the material and the specimen orientation, different initial crack propagation angles were observed in different specimens, see Table 2.5-2 and the schematic figure beside it. Figure 2.5-3 shows pictures of specimens A1 and D1 after failure. An interesting observation regarding specimen A1 is that despite of the proximity of the neighboring hole to the tip of the defect the growing crack deflected very distinctly, growing towards the third hole in the row.

Spec	Mtrl	Load-defect direction	Observed crack angle α
A1	AA2050-T84	L-S	~90°
A2			~90°
A3			~90°
A4			~90°
B1		T-S	~10°
B2			~10°
C1		(L-LT 45°)-S	~45°
C2			~45°
D1	AA7050-T7451	L-S	~30°
D2			~30°
D3			~30°
D4			~30°
E1		T-S	~0°
E2			~0°
F1		(L-LT 45°)-S	~25°
F2			~25°

Table 2.5-2. Approximate crack propagation angles.

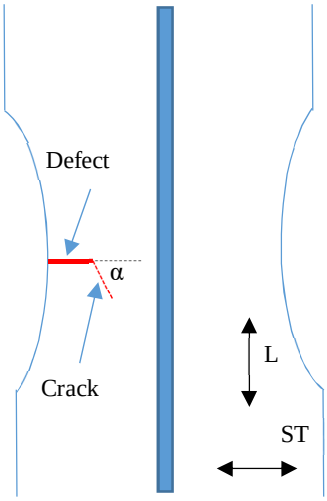

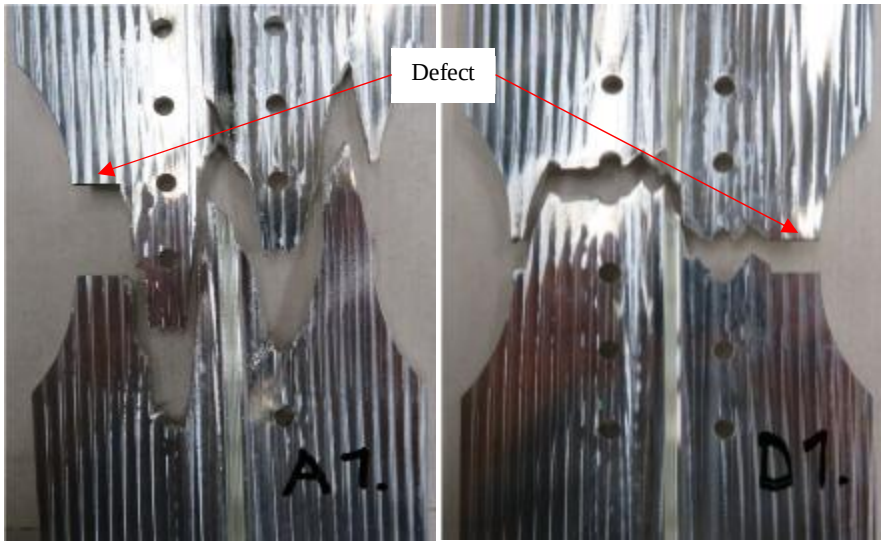

Figure 2.5-3. Specimens A1 (2050 L-S) and D1 (7050 L-S) after failure.

Comparison of the test and analyses results

Figures 2.5-4 shows the (stress intensity factor)/(apparent fracture toughness) ratios as function of net-section stress normalized by R_{p02} at initiation of failure load. A ratio of close to 1 is obtained for all specimens, except for AA2050 L-S specimens, when planar mode I crack growth is assumed. Under the assumption of deflecting crack, i.e. using k_{eff} instead of K_I, a ration of ~1.25 is obtained for AA2050 L-S specimens. Similar results are seen in section 2.4.

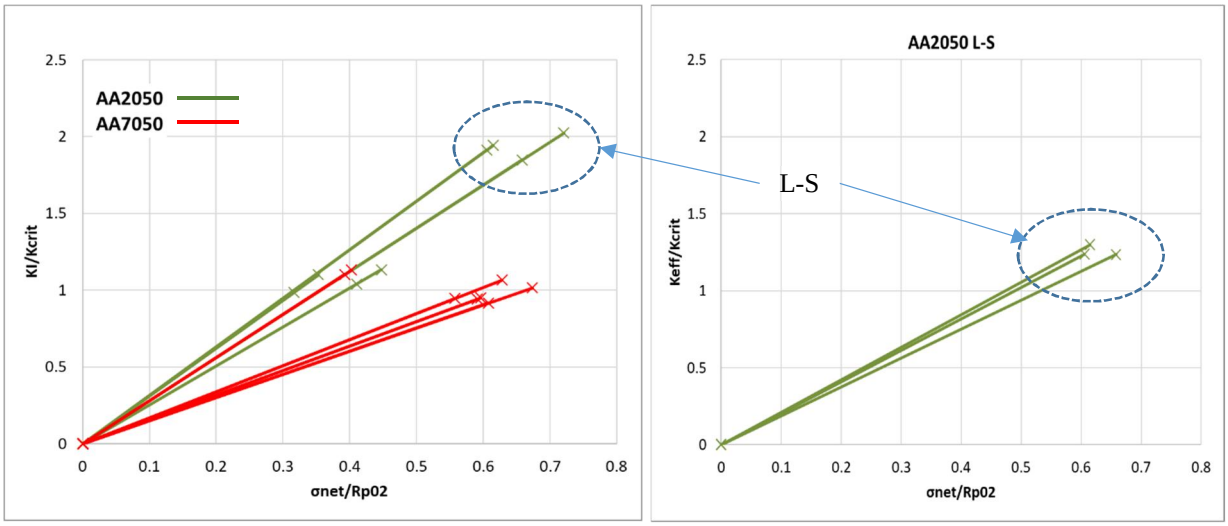

Figure 2.5-4. (Stress intensity factor)/(apparent fracture toughness) ratios for AA7050 and AA2050 at initiation of failure load.

Conclusions

- Residual strength tests and analyses of flange like plates made of AA2050-T84 and AA7050-T7451 including artificial defects were conducted.
- As in section 2.4, severe crack turning was observed in AA2050-T84 L-S specimens where the cracks clearly preferred to propagate along L-direction.
- For all specimens except the specimens in AA2050-T84, L-S direction: assuming a planar mode I crack growth, calculations gave stress intensity factors reasonably close to the apparent fracture toughness, at an applied load level at which the crack propagation was observed in the experiments.
- For the specimens in AA2050-T84, L-S direction:

- Straight crack growth assumption is conservative, which agrees with the results in section 2.4.
- Assuming crack deflection, the stress intensity factors comes closer to the apparent fracture toughness at crack propagation load.

References

[1] TL Anderson. Fracture Mechanics, Fundamentals and Applications. CRC Taylor & Francis 2005.
[2] AFGROW Technical Manual and Users Guide 5.3.1.21.

2.6 Ductile failure of AA2050-T84 plate specimens with a hole

Zlatan Kapidžić Saab AB, Rikard Rentmeester Saab AB

Introduction

Studies of crack growth in residual strength tests made of AA2050-T84, see sections 2.3-2.5 of this document, show that cracks originally oriented in ST-direction, have a tendency to turn towards L-direction during residual cracking when loading is in L-direction. Moreover it was observed in 2.4 and [1] that defect free sections containing stress concentrations failed in a similar manner. This raises a question whether or not this phenomenon has a detrimental effect on the static strength. This document presents a complementary study, where the ductile failure of defect free plate specimens with a hole, made of AA2050-T84 is studied. The goals of the study are:

- to experimentally investigate the ductile fracture behavior of AA2050-T84 in a simple geometry (plate with a hole)
- to evaluate the accuracy of the currently used analytical method for sizing for static failure.

Specimens

Altogether 38 specimens were taken out of a 130 mm thick plate. The length direction of the specimens was oriented in three different material directions (L, LT and ST as shown in Fig. 2.6-1), and the specimens were machined to plates of two different thicknesses, t, and four different widths, W. A through-the-thickness hole with a diameter D = 8 mm was machined in the middle of each specimen. In some of the specimens, the hole was filled by a standard bolt (N10 tolerance).

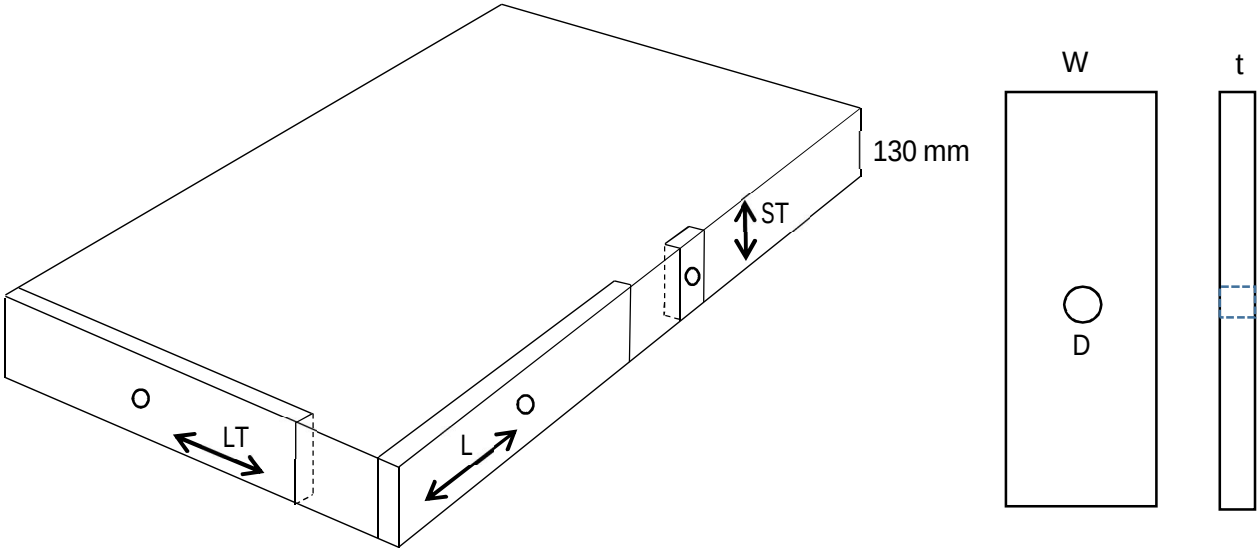

Figure 2.6-1. Specimen orientations.

Test procedure

Totally 34 specimens of 38 were tested to failure, 32 in tension and 2 in compression. The load was applied in the specimen length direction in displacement control with a 2 mm/min rate and the grip displacements and applied force from the load cells were registered and recorded. The specimens were filmed during the load application in order to register the initiation and progression of the cracking at the edge of the hole. A voltmeter, calibrated to the signal from the load cell, was rigged next to the specimen and was visible in the film frame during the test.

Analyses

Two types of analyses are performed:

- Hand calculations of the failure load, assuming that the failure takes place when the net-section stress equals R_m, i.e. the failure force is $R_m \cdot t \cdot (W - D)$. This is the common method normally used in static sizing. For comparing the analysis to test results, mean values of the ultimate strength are used.
- Non-linear FE analysis, where a plane model of the plate is used with a non-linear isotropic plasticity material model. The true effective plastic strain - true stress mean curves are derived from standard tensile tests and are shown in Fig. 2.6-2. In the analyses, the plates are loaded up to a force of $R_m \cdot t \cdot (W - D)$, and the net-section stress as a function of grip displacement is extracted.

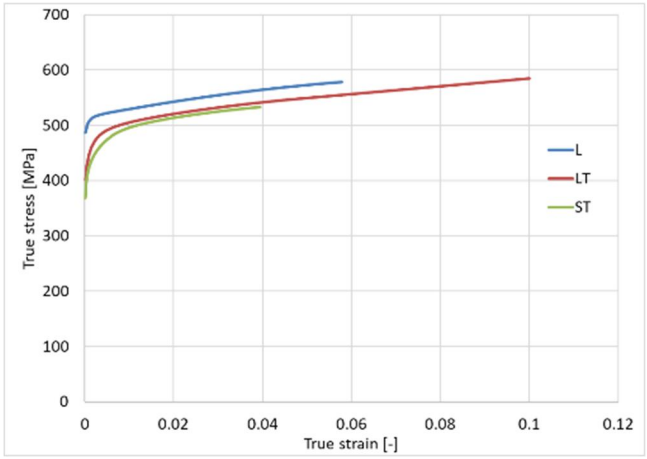

Figure 2.6-2. True stress strain curves used in the FE analyses.

Results

Test results

The following was observed during testing and by examination of the recorded material:

- All specimens displayed a considerable amount of plastic deformation prior to failure, which can be seen on the load-displacement curves, cf. Fig. 2.6-4.
- The specimens loaded in L-direction showed a clear tendency to crack in the L-direction, perpendicular to the net-section, see example in Fig. 2.6-3. The cracking started at maximum load.
- LT and ST oriented specimens cracked along the net-section plane perpendicular to the load, see example in Fig. 2.6-3..
- No effect of the filled hole on the cracking behavior or the failure load was seen.
- No cracking was observed in the specimens loaded in compression.

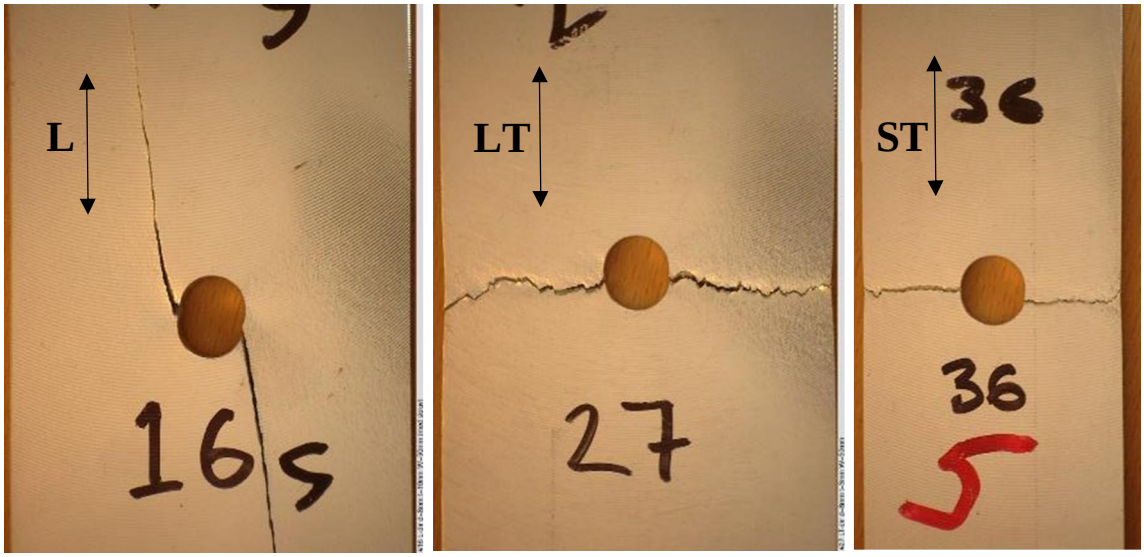

Figure 2.6-3. Failed specimens.

Comparison of test and analyses results

The failure load obtained by tests falls within 5% deviation of the hand calculated failure load $R_m \cdot t \cdot (W - D)$ for all specimens tested in tension, see Fig. 2.6-4.

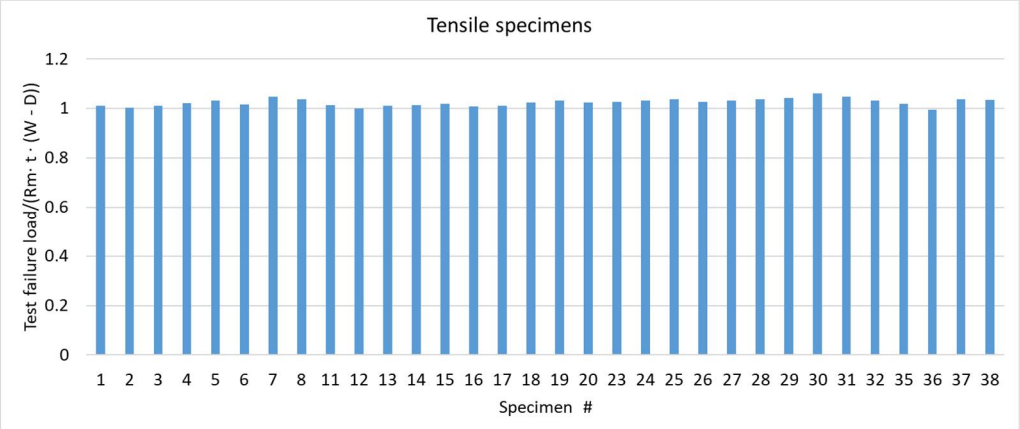

Figure 2.6-4. Comparison of test failure load and hand calculated failure load.

Fig. 2.6-5 shows the FE and test results expressed in the net-stress (load/net-area) versus the grip displacement normalized with the specimen length. The video recordings show that the cracking initiates when the net-stress is close to R_m in all cases. Although some of the test curves are slightly non-linear even in the elastic regime, the upper parts of all curves are clearly indicating plastic deformation during considerable part of the test.

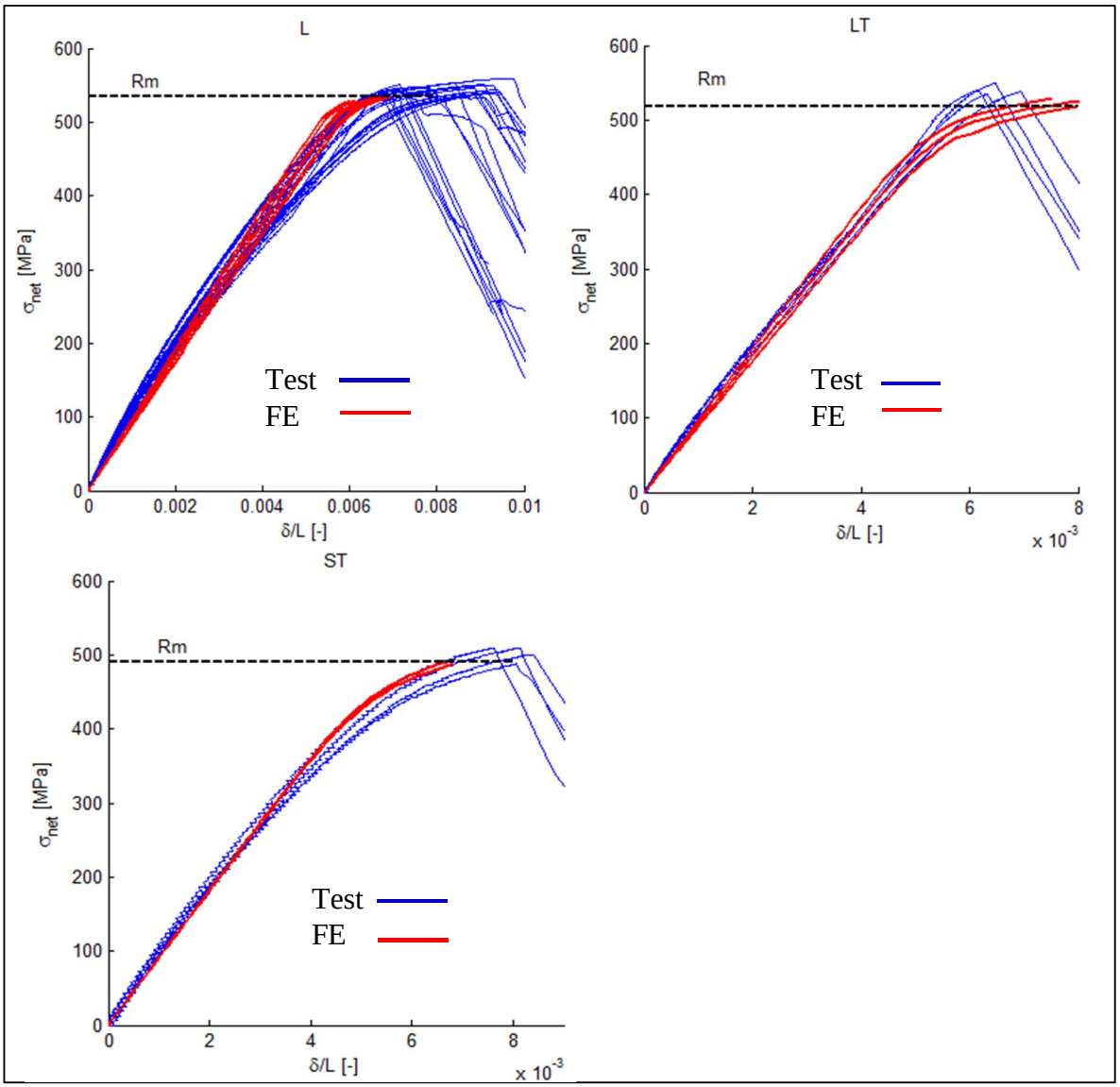

Figure 2.6-5. Net stress vs. normalized grip displacement, L, LT and ST specimens.

Conclusions

Tests and analyses of AA2050-T84 plate with hole specimens in L, LT and ST directions have shown that predictions of the static failure load, based on the assumption that the net-stress equals R_m at failure, correspond well with the test results. Residual crack turning towards L-direction was observed in the tests but had no effect on the ultimate load capacity of the specimens.

References

[1] Ansell, H. A Review of Aeronautical Fatigue Investigations in Sweden During the Period April 2015 to March 2017, ICAF 2017 Proceedings of the 36th Conference, Nagoya, Japan.

2.7 Bending tests in aluminium-lithium AA2050-T84

Rikard Rentmeester Saab AB, Zlatan Kapidžić Saab AB

Introduction

Aluminium-lithium has become an interesting alternative to conventional aluminium alloys in airframe applications due to its relative higher stiffness and strength and the lower density. Early generations of the alloy had a pronounced tendency to fail in predominated material directions. The texture of the material makes it prone to crack through the plate thickness, rather than across the longitudinal direction. This has behaviour has been observed also in the present alloy, AA2050-T84.

In addition to anisotropic crack propagation and residual strength values, the material displays anisotropy also in regular strength values. The short transversal direction (ST) is weaker than the longitudinal (L) and the long transversal (LT) directions. This applies to uniaxial tensile strength and ductility as well as to shear strength. Hence, the question regarding static failure mode in this alloy has arisen. If this is an issue that must be taken into account in static sizing of the airframe, it would have a detrimental impact on the regular design work and stress analyses in the product development.

Several non-standard structural tests were carried out in order to determine whether it is an issue or not. The test objects were all single machined parts load quasi-statically in various directions. That means that no fasteners or other structural parts were involved, except for the test rigs. The tests were designed in order to provoke progressive failure in the material ST-direction.

Beam bending tests

Type 1

Four-points bending tests with various notches and stress concentrations tests were used to introduce stress states that is not normally covered by regular material testing. A test rig as shown in Figure 2.7-1 was used in the tests.

First of all, a solid beam with rectangular cross section, 40x50 mm was developed, see Figure 2.7-1b. In the bending area of the beam, two perpendicular holes were made. Thus, the critical section consisted of three ligaments, (A), (B) and (C), as shown in Figure 2.7-1b.

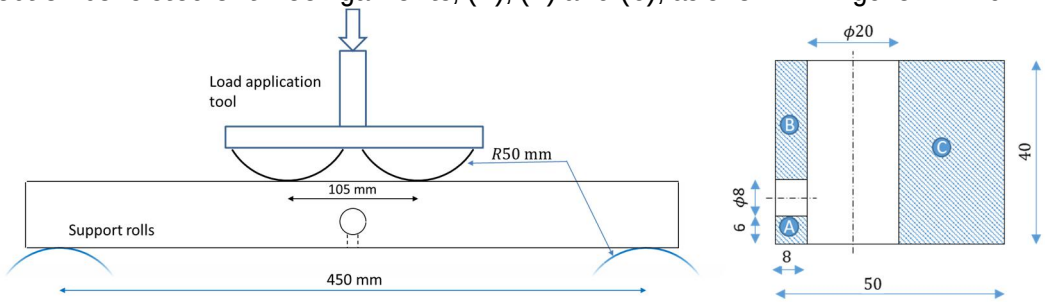

Figure 2.7-1. (a) Four point bending test rig with a special designed test specimen. (b) Cross section of the specimen.

In the first test, the small hole was oriented downwards, see Figure 2.7-1(a). Figure 2.7-2 shows the result of the testing. The failure occurred in two steps. First, the relative small ligament failed in tension, as expected. However, the secondary failure occurred in terms of a crack along the specimen, originating from the hole. This is somewhat unexpected from a

sizing point of view, where the section that is considered to be critical is perpendicular to the beam, as indicated in the figure. It should also be mentioned that the same type of test was carried out in aluminium AA7050-T7451, and the failure mode in this material was as expected.

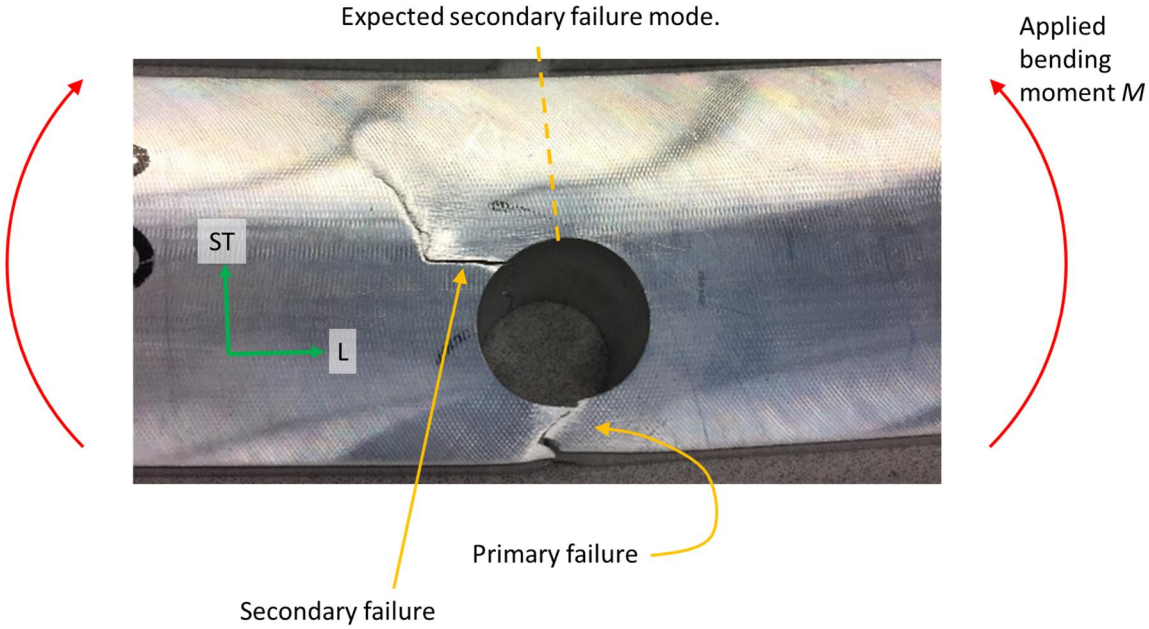

Figure 2.7-2. Failure behaviour of the aluminium-lithium beam.

The second type of test was carried out on a test specimen similar to the on shown in Figures 2.7-1 and 2.7-2. However, the specimens were rotated so that the ST-direction was perpendicular to the load application direction. The result is shown in Figure 2.7-3. First, the ligament A failed in tension, as expected. However, the subsequent progressive failure occurred along the specimen. The large ligament (C) deformed plastically without any failure.

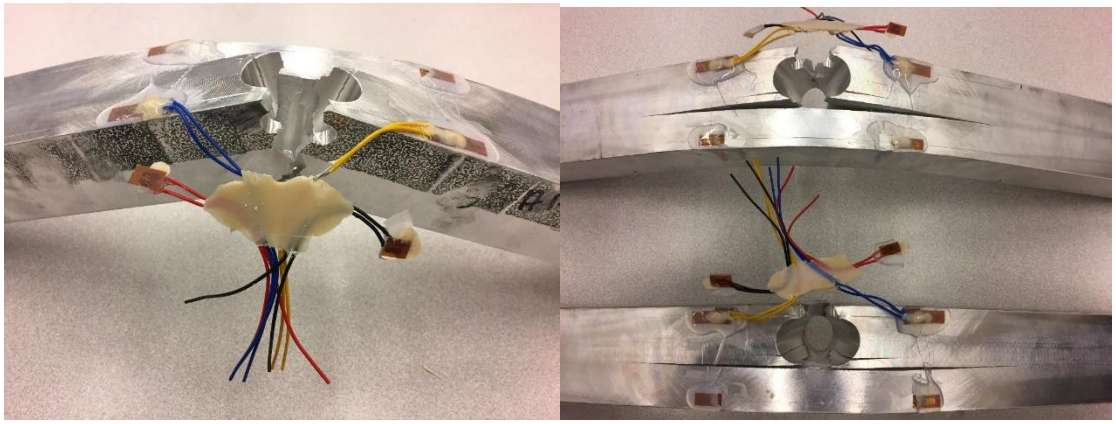

Figure 2.7-3. Post-test images of the tests.

Type 2

The result of the Type 1 beam tests called for further testing, with emphasis on the static failure behaviour in the ST-direction. It was suspected that the rather poor shear strength in the ST-L direction was the governing property that resulted in the unexpected failure modes. Therefore, beam test type 2 was developed, see Figure 2.7-4. Various combinations of R and h was used. Figure 2.7-5 shows a post-test image of the test type 2 specimen. Although the

crack direction is not as pronounced as in type 1, see Figure 2.7-2, the onset of the crack is oriented long the test object.

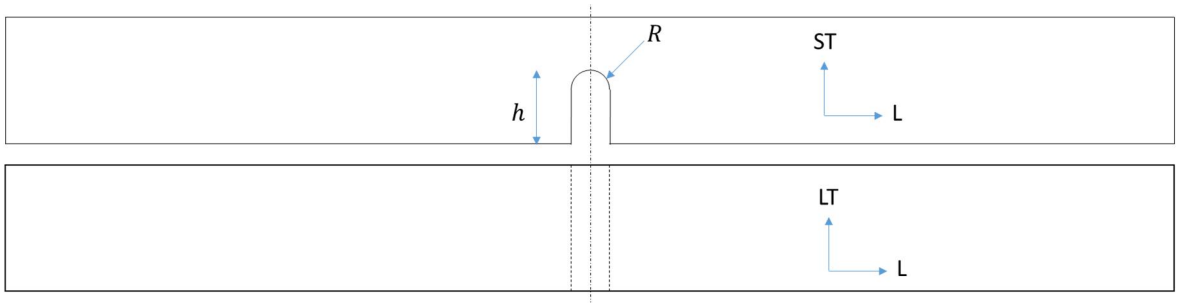

Figure 2.7-4. Beam test type 2.

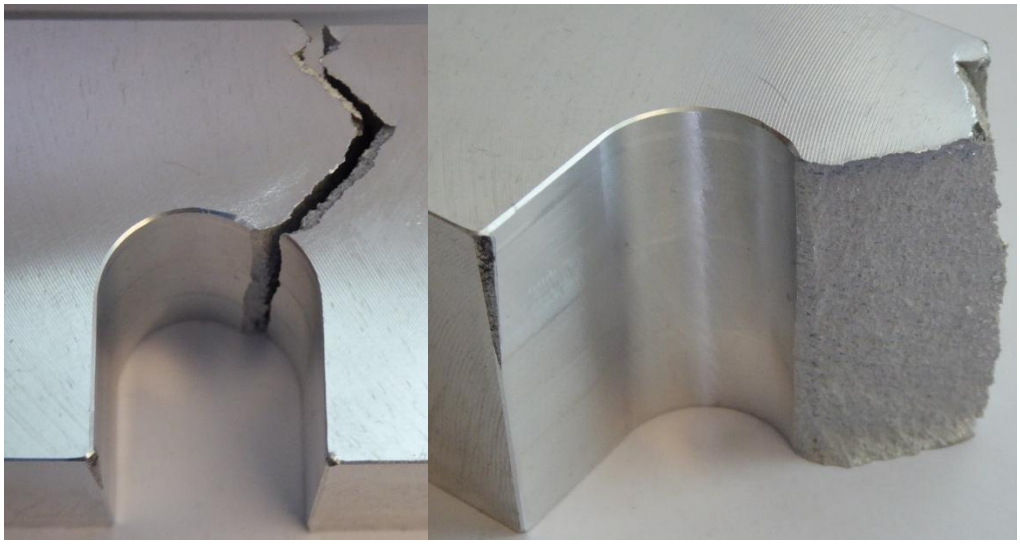

Figure 2.7-5. Post-test image of the beam test type 2.

Type 3

A test object were developed in order to test the shear strength in combination with stress concentrations. The test objects consist of I-beam sections with pockets. Contrary to types 1 and 2, the test areas are located between the inner load applications rolls and the outer support rolls. Hence, the test setup is rather a three point test than a four-point test. The webs of the beams are oriented in the materials L-ST plane. The failure started at the hole and was consequently oriented along the material L-direction.

Figure 2.7-6. Beam test type 3.

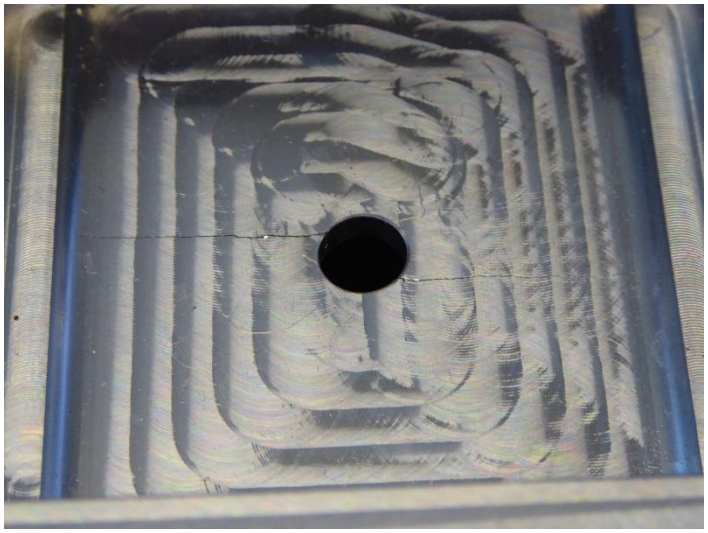
Figure 2.7-7. Post-test image of the type 3 specimen.

Analyses of the tests
Finite element analyses as well as handbook calculations were carried out in order to predict the ultimate load capacity of the test objects. The FE analyses were carried according to standard procedure, including non-linear material representation, non-linear geometry and contacts where applicable. The following conclusions were drawn:

- The overall deformation until the onset of cracking is well predicted by the FEA.
- Effective plastic deformation (von Mises) is not a sufficient quantity to use for the onset of cracking.
- The onset of cracking seems to be driven by a combination of shear stress and normal stress in the ST-direction.
- The ultimate load capacity in the tests correlated well with or exceeded the prediction made by the handbook calculations.

Conclusions
The static failure behaviour in the aluminium-lithium alloy AA2050-T84 showed a consequent tendency to crack along the material L-direction, perpendicular to the ST-direction, rather than perpendicular to the first principal stress direction. Although the failure occurred in sections that may not be considered in regular sizing, it was found that the load levels at failure were above or similar to what is normally considered as the ultimate load capacity of the objects.

2.8 Development of data and method for fatigue sizing of bolted joints in AA7050-T7451 and AA2050-T84

Zlatan Kapidžić Saab AB, Hans Ansell Saab AB

This chapter highlights the international cooperation research activities in between Saab Aeronautics (Sweden) and VTT (Finland)

Introduction
Current method for fatigue sizing of bolted joints in aluminium at Saab is based on data for joints in sheet materials AA2024 and AA7050. The methods and data for this purpose was

developed in the early 70-ies mainly for Saab 340 and Gripen A type of assembled thin sheet structure. Commencing with Gripen C/D and driven further in Gripen E/F is the vast use of machined integral structural solutions by use of thick aluminium plate product forms. Bolted joints in conventional AA7010/7050 alloys have been able to be handled with fairly accurate corrections of the original methods for Gripen C/D. Gripen E/F however will use Aluminium-Lithium alloys AA2050 to a huge extent which current corrections to existing methods and design data cannot handle in a proper way. New design data and modifications of the methodology is needed.

The aim of the work is to generate design data for bolted joints in thick plate alloy AA2050 and to adjust current stress severity factor method to fit to the stress analysis working process. Additional tests with specimens manufactured from thick plate alloy AA7050 are done on a limited basis. The work is split into two parts:

- Constant amplitude (CA) and spectrum fatigue testing of bolted joints
- Development of the fatigue sizing method

and will come together in a comprehensive methodology.

Test matrix principle

The principle for building up the test matrix and the expected outcome for evaluation is schematically outlined below. Complete SN-curves (three load levels) shall be generated only for R = 0 and R = -1 for AA2050 alloy and for R = 0 for the AA7050 alloy. Other variations, such as specimen type (single or double shear), number of fastener rows (2 or 3) , plate thickness (3mm or 5mm), fastener type (countersunk or protruding, Hi-Lite or Ti-screw), fastener diameter (6mm or 8mm), variable amplitude loading, are founded on fewer test specimen results. Figure 2.8-1 shows the schematic representation of the test matrix principle for CA tests.

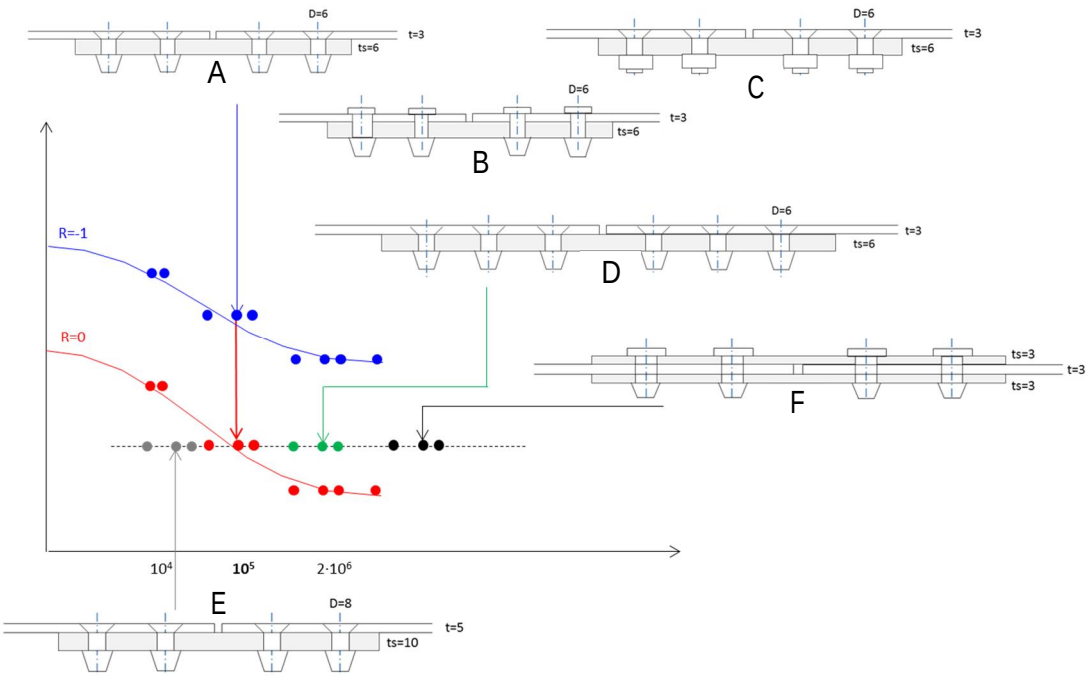

Figure 2.8-1. Test matrix principle for CA testing.

The idea behind the variation of joint parameters included in the testing is to obtain a data set with varying amount of bolt transferred/by-pass load, secondary bending and stress

concentration. All three of these parameters have an effect on the fatigue life and are included in the sizing method.

Test specimens

All specimens are two-column butt joints with a width of 8D and with various fastener types: specimens A, D and E are bolted with countersunk Hi-Lites, specimens B and F are bolted with protruding head Hi-Lites and specimens C are bolted with countersunk Ti-screws. Four of the C specimens were assembled with low pretension torque (~2Nm) and all other specimens were torqued to a level prescribed by the industrial standard (~6Nm, referred to as "normal torque"). Table 2.8-1 shows the number of tested specimen types, cf. Figure 2.8-1, at various stress amplitude (S_a) levels, the target life and load ratios (R) for both materials. The number of specimens tested in spectrum loading is also shown.

		R = 0			R = -1			Smin = 60 [MPa]	Spectrum Tensile		Spectrum Tensile/ Compressive	
	Spec Type	S_a = High 10^4	S_a = Mid 10^5	S_a = Low $2*10^6$	S_a = High 10^4	S_a = Mid 10^5	S_a = Low $2*10^6$	S_a = Mid 10^5	S_{max} = High 30 kflh	S_{max} = Low 60 kflh	S_{max} = High 10 kflh	S_{max} = Low 20 kflh
AA2050	A	4	4	4	2	3	4	3	2	2	1	1
	B		3	2								
	C		4	1								
	D		3	2								
	E		3	2								
	F	2	3									
AA7050	A	3	4	4		3			3	1		
	C		4	1								

Table 2.8-1. Test matrix, number of tested specimens, totally 78 specimens tested.

Two spectra were used with about 60 cycles/flight hour, a tensile dominated wing bending spectrum and a tensile/compressive fin spectrum. The results from spectrum tests are used subsequently for validation of cumulative damage calculations.

Test setup

Two uniaxial tensile/compressive machines were used in order to speed up the testing time. The specimens were installed in the grips with shimming plates at each end. Initially, 7 tests were performed without any lateral support and a very significant secondary bending was observed. 3 of these specimens failed in the joint plate whereupon it was decided that a lateral support shall be used, see [1]. Figure 2.8-2 shows an early sketch of the lateral support and its realisation later on. The support had a significant influence on the secondary bending and its effects were evaluated using non-linear FE-model of the setup.

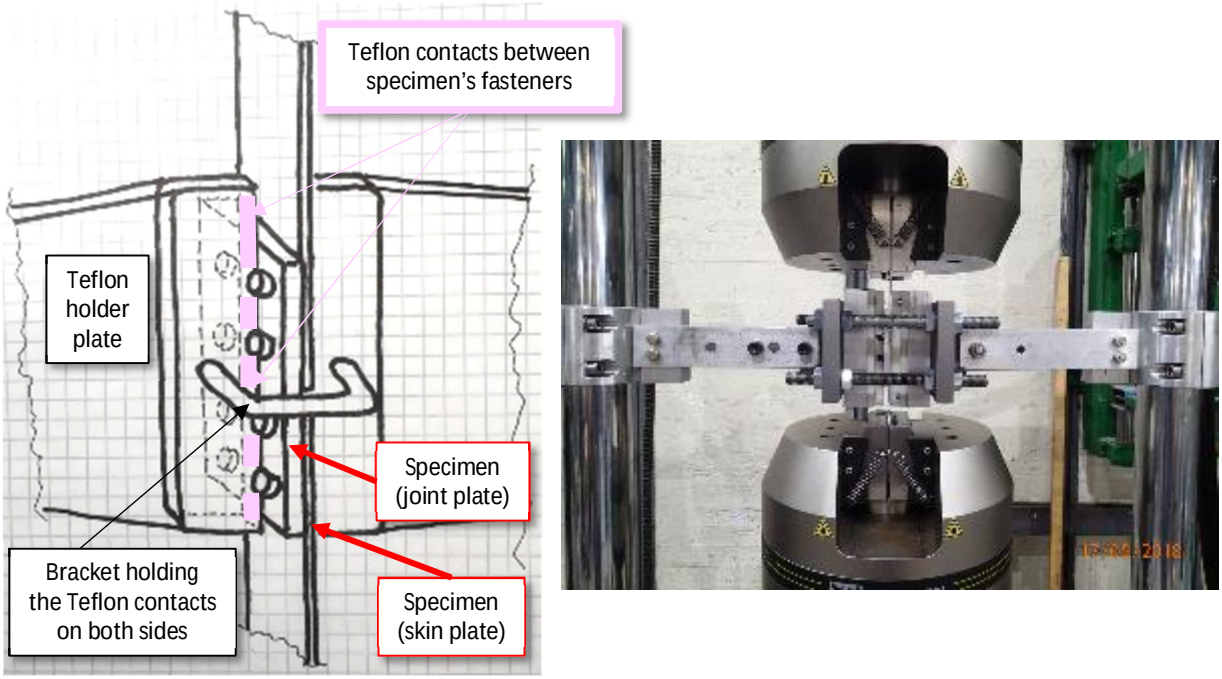

Figure 2.8-2. Lateral support.

Test results

Figure 2.8-3 shows all test results in terms of applied gross stress amplitude σ_a and number of cycles to failure N_f. Some general comments about the test results presented in Figure 2.8-3:

- Specimens A, B and C had roughly the equally long fatigue lives, which is why they are presented as the same category in Figure 2.8-3.
- Specimens with no lateral support had significantly shorter fatigue lives than the ones with the support.
- Specimens with low pretension (2Nm) had significantly shorter fatigue lives than the ones with normal pretension (6Nm).
- Specimens E tend to have a slightly shorter lives than specimens A, B and C and specimens D and F tend to have longer lives.
- Tests at R = - 1 gave longer lives than the tests at R = 0, as expected, cf. Figure 2.8-1.
- AA2050 specimens had on average 1.5 times longer life than AA7050 specimens.

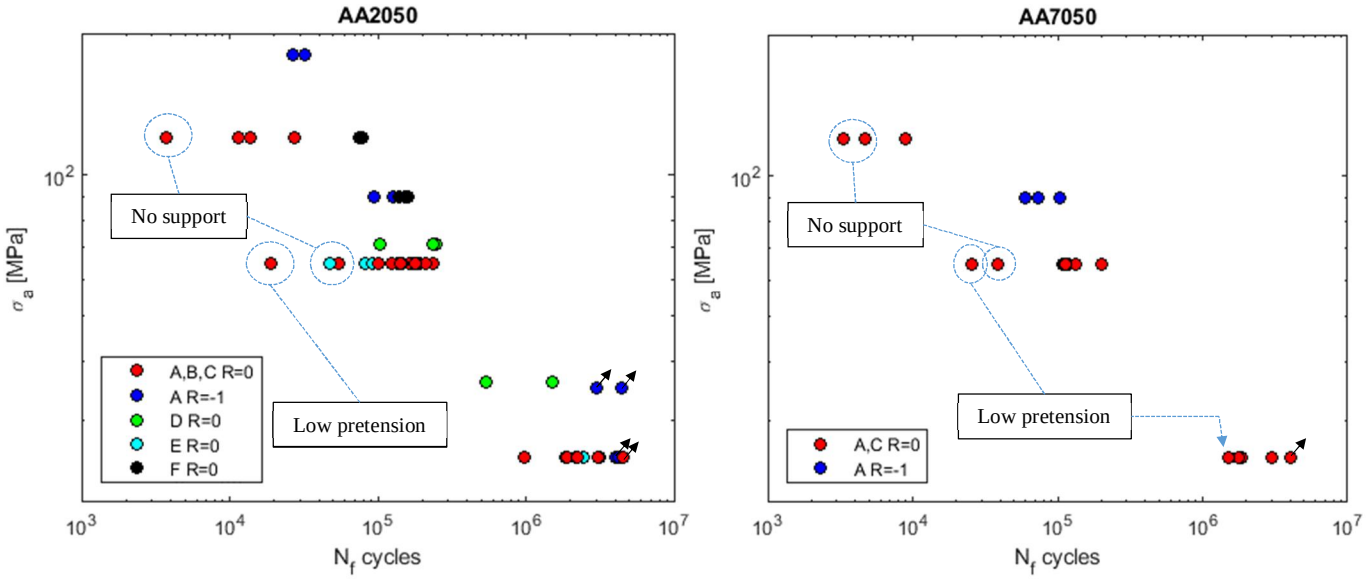

Figure 2.8-3. Test results, gross stress amplitude and number of cycles to failure N_f.

The observed failure/cracking modes of all specimens are categorized in the following four groups as shown in Figures 2.8-4:

I Cracking though the net-section of the outer bolt hole row of the skin plate
I* Cracking though the gross section of the skin plate near the outer bolt hole row
II Cracking though the gross section of the skin plate at the joint plate edge
III Cracking through the joint plate at the inner bolt hole row

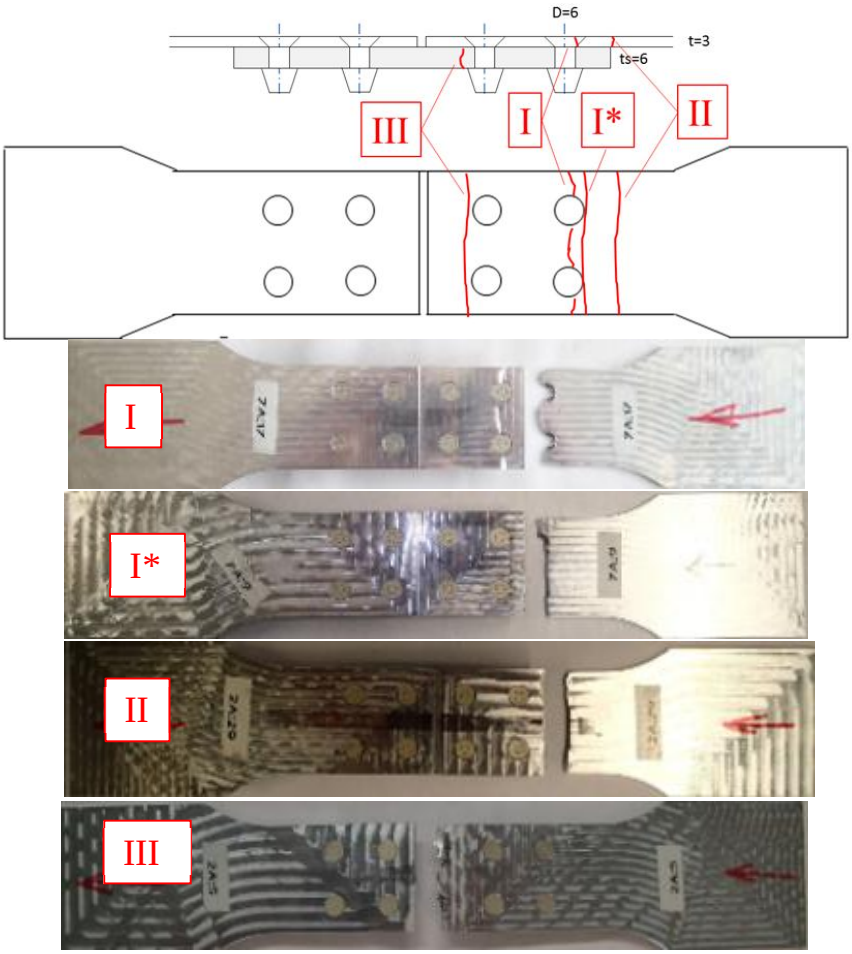

Figure 2.8-4. Observed failure modes.

Failure modes I and I* were observed in ~70% of the test specimens and are the modes of interest for formulation of the sizing method. A fractography study of the fracture surface of 6 specimens that failed in modes I and I* was performed by VTT [2], see Figure 2.8-5. In normally pre-torqued specimens, the cracks typically initiated at the faying surface of the skin plate at some distance from the hole in both mode I and I*. In specimen with low pre-tension, the cracks initiated from the hole edge at the faying surface. These findings suggest that the stress concentration created by the bolt hole is probably of less importance than the amount of load transfer and secondary bending in normally pre-torqued joints.

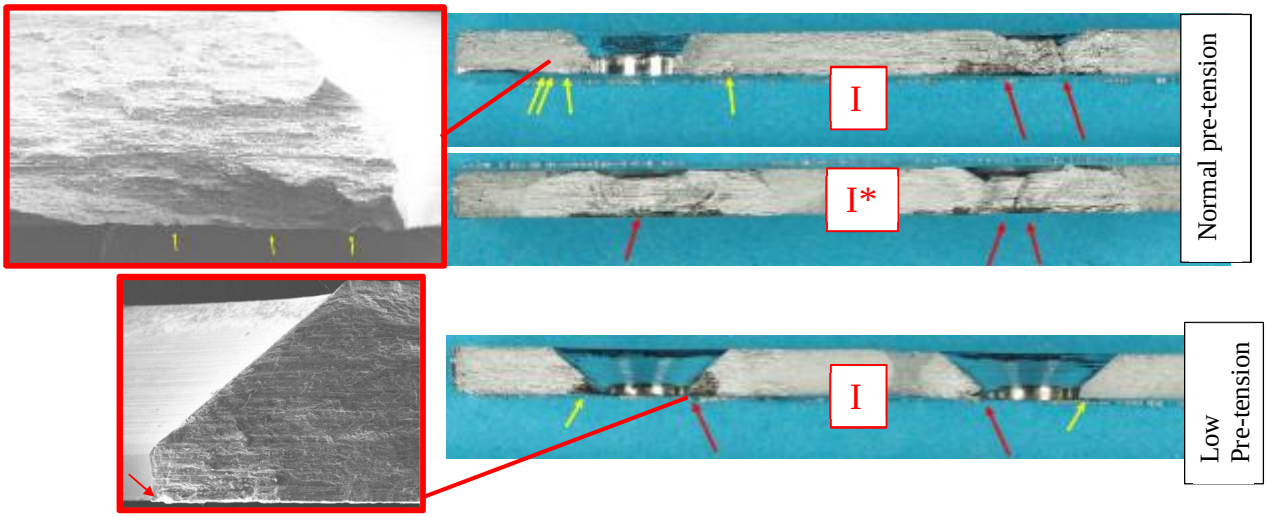

Figure 2.8-5. Fractography images of the typical crack initiation sites.

Fatigue sizing method

The present method is based on the concept of reference geometry method presented in [3] and outlined below. Consider the critical (mode I) bolt row in the skin plate and the stresses applied on it, see Figure 2.8-6.

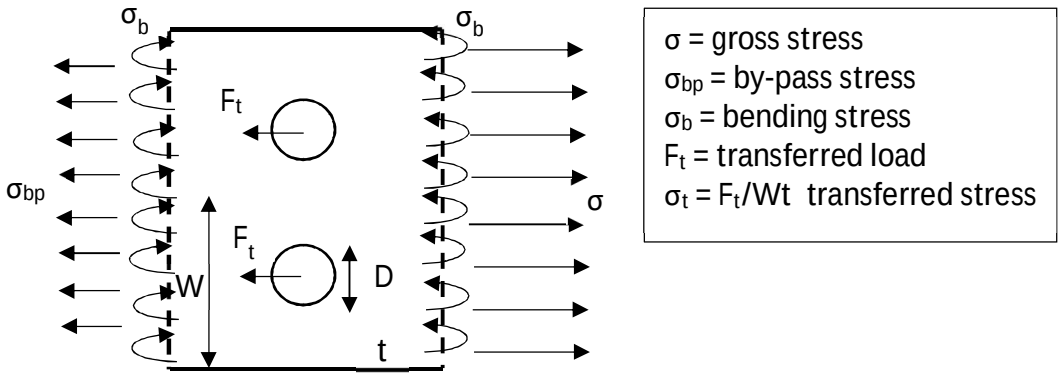

Figure 2.8-6. Stresses in the skin plate at the critical bolt row.

The net-section stress is written as

$$\sigma_n = \frac{\sigma(1 + k_b)}{1 - \frac{D}{W}} \qquad (2.8\text{-}1)$$

where k_b is the bending to gross stress ratio σ_b/σ. A log-linear type relation is assumed between the net-section stress amplitude σ_n, fatigue life N, stress concentration K_t and load ratio R. Expressed in terms of gross stress amplitude σ_a, via 2.8-1, this relation yields

$$\sigma_a = C(K_t)^p(1 - R)^q N^{-1/m} \frac{\left(1 - \frac{D}{W}\right)}{(1 + k_b)} \qquad (2.8\text{-}2)$$

where C, p, q and m are material parameters and K_t is defined as

$$K_t = \left((1-f)K_{tg} + f\frac{W}{D}K_{tt} + k_b K_{tb} \right) \frac{1-\frac{D}{W}}{1+k_b} \qquad (2.8\text{-}3)$$

where $f = \sigma_t/\sigma$ is the transferred load ratio and K_{tg}, K_{tt} and K_{tb} are stress concentration factors for by-pass, pin and bending load, defined as ratios between max stress at hole edge and gross stress, bearing stress and bending net-stress respectively. The parameters in Equation 2.8-3, including the bending ratio k_b, are determined using FEM for all specimens.

Equation 2.8-2 is logarithmised and fitted to the data by the least squares method. Modes II and III are considered to be outside of the scope of the method at hand and will not be regarded as such within it. The test results related to failure mode II and III are, however, included in the data for method formulation if the fatigue life is equal or longer than the life of mode I for same specimen type. The results for tests with no lateral support are included in the data, considering increased secondary bending which is calculated using FEM. The tests with low pretension are not included. All fatigue lives for AA7050 specimens were scaled by 1.5 in order to reduce the data to a single set. There was not enough AA7050 data points to fit the materials separately. A log-linear regression is performed on the gross stress amplitude normalized by the K_t, *R, D/W* and k_b factors in 2.8-2 (referred to as S_a) and the result is shown in Figure 2.8-7.

Equation 2.8-2 can be solved directly for N for any set of joint parameters and the cumulative damage can be obtained for any gross stress spectrum. However, the relation 2.8-2 is valid only in the range of the test data (10^4 - $4*10^6$) and all stress amplitudes evaluated outside that range will yield unrealistic fatigue life. Therefore it is more feasible to adopt the concept of reference joint [3] in order to suit the already established methodology at Saab.

First, a Haigh diagram is constructed for a reference geometry (in this case type A specimen) based on Equation 2.8-2 with joint type A parameters. The tails of the S-N curves are provided with asymptotes at R = 0, tending towards 250 MPa at 10^3 and to 25 MPa at 10^7. This is an ad hoc correction based on evaluation of earlier data and is used for now until some more elaborate method can be established. Haigh diagram for AA7050 reference joint is scaled down by using $C = 7272*(1.5)^{-1/m}$ in 2.8-2, because we have previously scaled the data up by a factor of 1.5, and is shown in Figure 2.8-8.

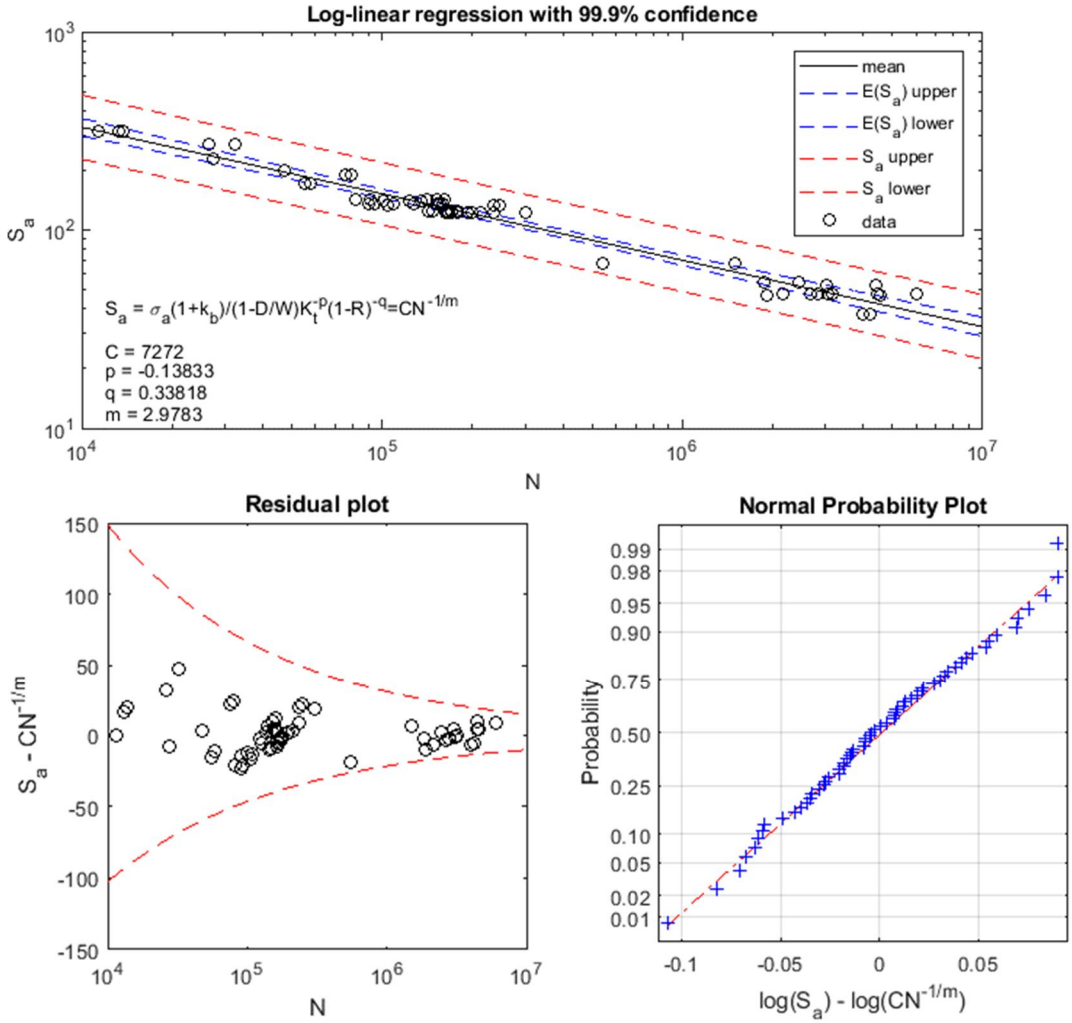

Figure 2.8-7. Log-linear regression of the fatigue data, with the confidence interval for the mean $E(S_a)$ and the prediction interval based on log-normal distribution of the error.

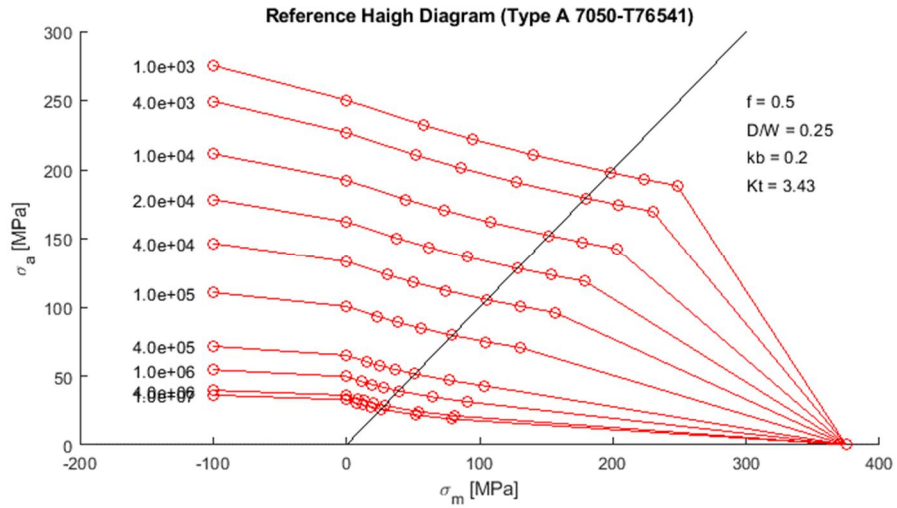

Figure 2.8-8. Reference Haigh diagram, Type A joint, AA7050.

In line with the method in [3], a Haigh diagram for an actual joint geometry is calculated from the reference Haigh diagram as

$$\sigma_a = (\sigma_0)_a \cdot \phi \qquad (2.8\text{-}4)$$

where $(\sigma_0)_a$ are the gross stress amplitudes for the reference geometry and the correction factor is

$$\phi = \left(\frac{K_t}{K_{t0}}\right)^p \frac{\left(1-\frac{D}{W}\right)}{\left(1-\left(\frac{D}{W}\right)_0\right)} \frac{(1+k_{b0})}{(1+k_b)} \qquad (2.8\text{-}5)$$

where the subscript *0* refers to the reference geometry. The mean stresses σ_m are scaled by the same correction factor. Cumulative damage is based on the Palmgren-Miner rule.

Evaluation of the fatigue sizing method

The method outlined above is applied for calculation of cumulative damage for spectrum loaded specimens of Type A. Figure 2.8-9 shows the comparison of test results with the method predictions assuming failure at damage equal to one.

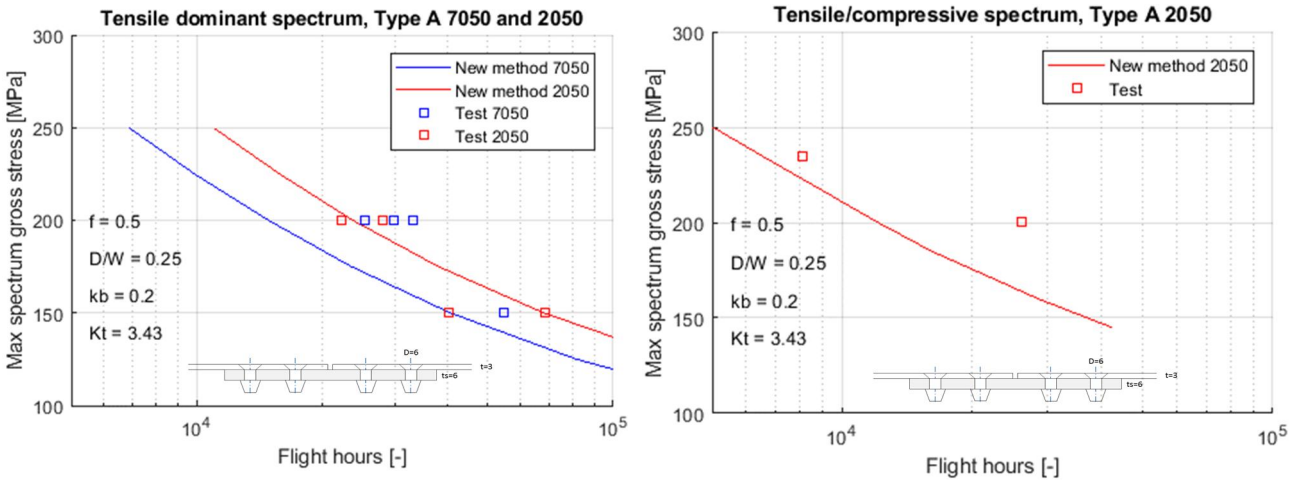

Figure 2.8-9. Test results and prediction for Type A specimens.

Further comparisons are performed to data presented in [4] and [5] where several types of 7050-T7651 specimens with Hi-lok fasteners were tested using FALSTAFF spectrum. The same secondary bending and transferred load as measured with strain gauges [4] are used in the predictions. The comparisons are shown in Figures 2.8-10-13.

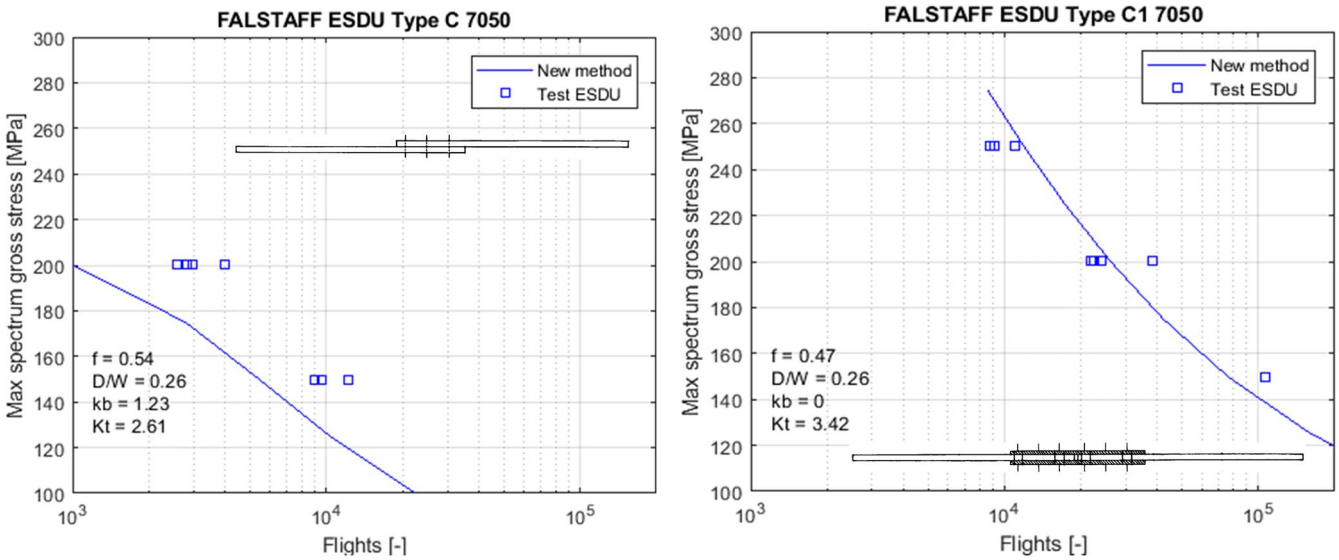

Figure 2.8-10. Test results and prediction for Type C (single shear) and C1 (double shear) specimens [4].

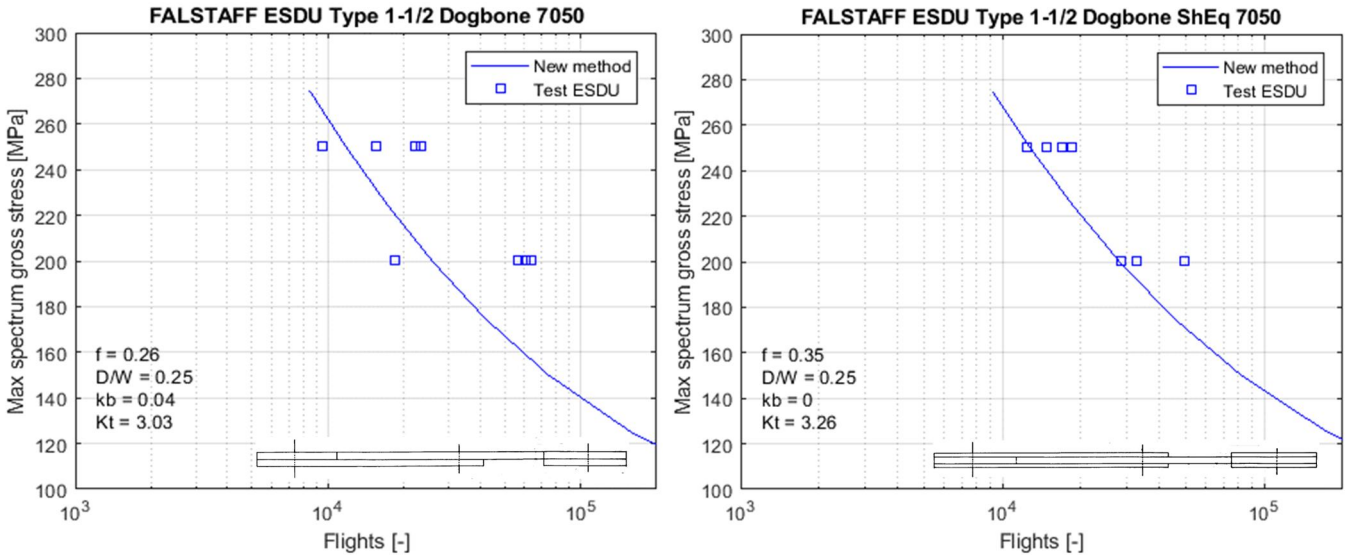

Figure 2.8-11. Test results and prediction for Type 1-1/2 Dogbone and 1-1/2 Dogbone shear equivalent specimens [4].

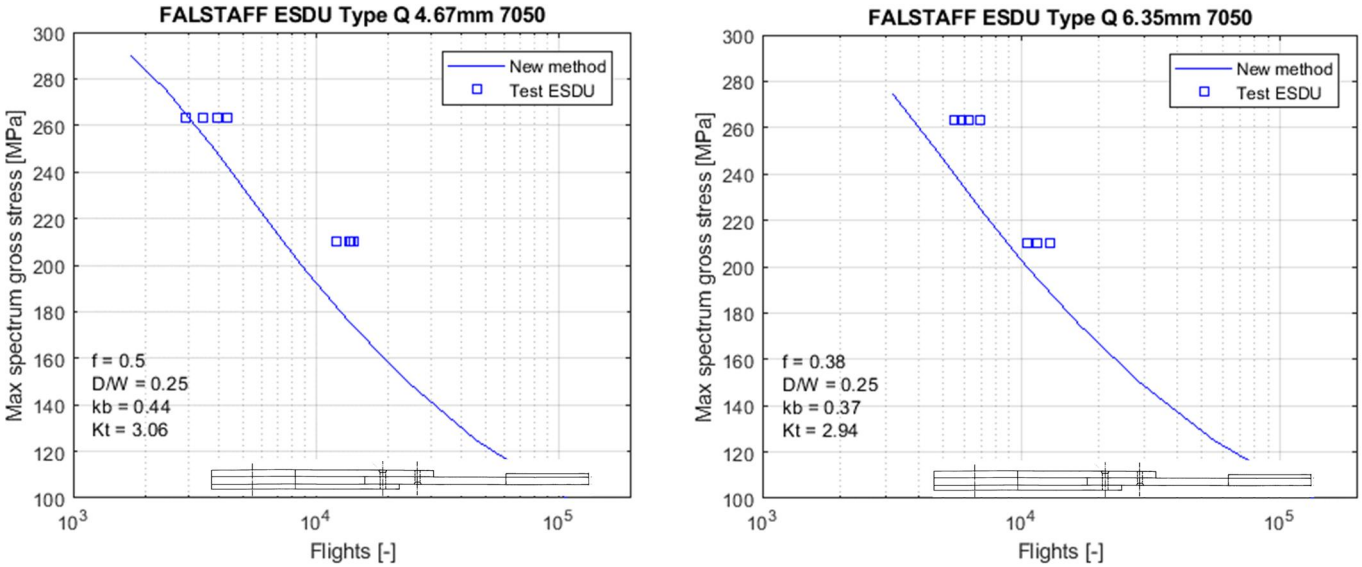

Figure 2.8-12. Test results and prediction for Type Q 4.67 mm and Q 6.35 mm specimens [4].

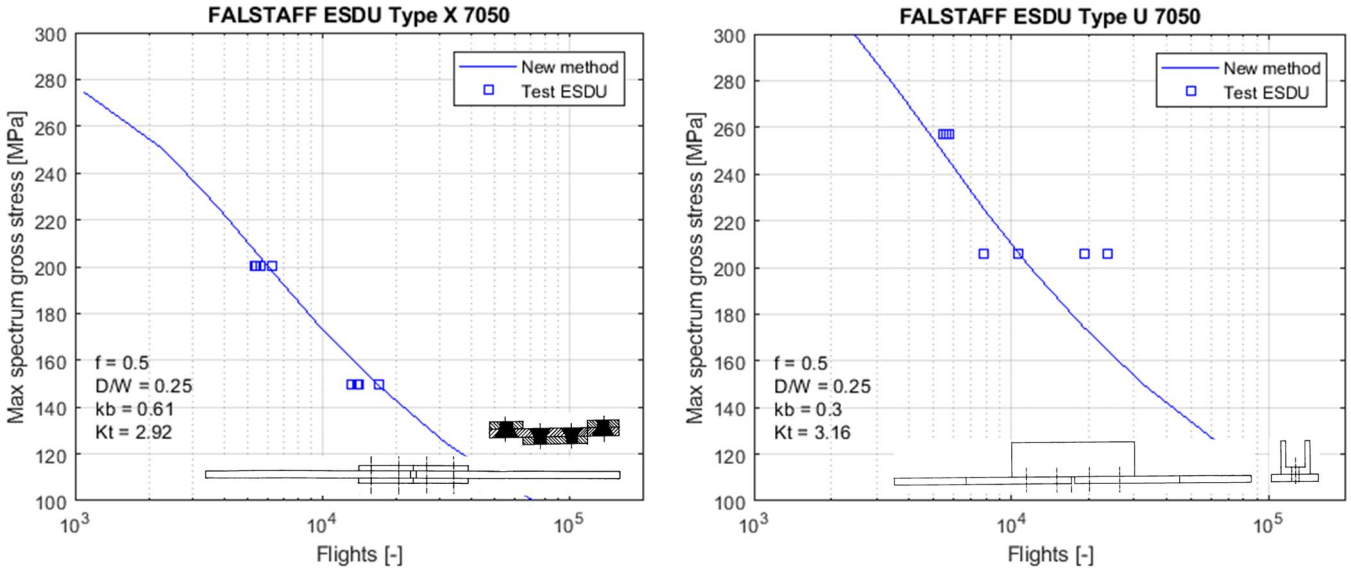

Figure 2.8-13. Test results and prediction for Type X and U specimens [4] and [5].

Conclusions

- A fatigue test series including varying joint configurations in alloys AA7050 and AA2050 were conducted.
- A fatigue sizing method, based on the concept of reference geometry is developed and fitted to the test data. The method takes into account the amount of transferred load, secondary bending, stress concentration and spectrum loading and is valid for normally torqued joints.
- Predictions of spectrum fatigue life of several tested specimens and tests of 8 different types of joints from the literature were in satisfactorily correlation with the test results.

References

[1] Koski K. Bolted joint tests, Research Report VTT-R-00065-19.

[2] Yli-Olli S, Koski K. Fractographic and metallographic evaluation of fatigue test pieces, Customer Report VTT-CR-00308-19.

[3] Larsson SE. The development of a calculation method for the fatigue strength of lugs and a study of test results for lugs of aluminium. Proceedings of the 4th ICAF Symposium, 1969.

[4] ESDU 90018. Fatigue of aluminium alloy joints with various fastener systems. High load transfer.

[5] FFA TN 1986-01. Fatigue Life and fastener flexibility of single shear joints with countersunk fasteners.

2.9 Structural integrity of repaired monolithic metal structure

Hans Ansell Saab AB
Anders Klarbring, Ulf Edlund, Bo Torstenfelt, Linköping University

Primary load carrying structures in fuselages are mainly manufactured from machined and/or forged single pieced parts. Such parts are weight optimized and contain most often stress raisers of various kinds e.g. cut-outs, thickness steps, interacting radii which make them prone to fatigue failure. The number of such hot-spots seems to increase when designing with digital modelling techniques. If fatigue cracking occurs during service life it is costly and impractical or most often impossible to replace these parts. A repair procedure to restore flight safety and availability is needed which includes several challenging engineering activities which involve research work.

Inventory and problem definition

An inventory is made of typical aircraft primary structural components prone to fatigue cracking. Typical structural design parameters are identified such as pocket sizes, thicknesses, holes and cut-outs and related significant design load cases. Based on these findings, generic damages scenarios are defined as starting points for further analysis and demonstration.

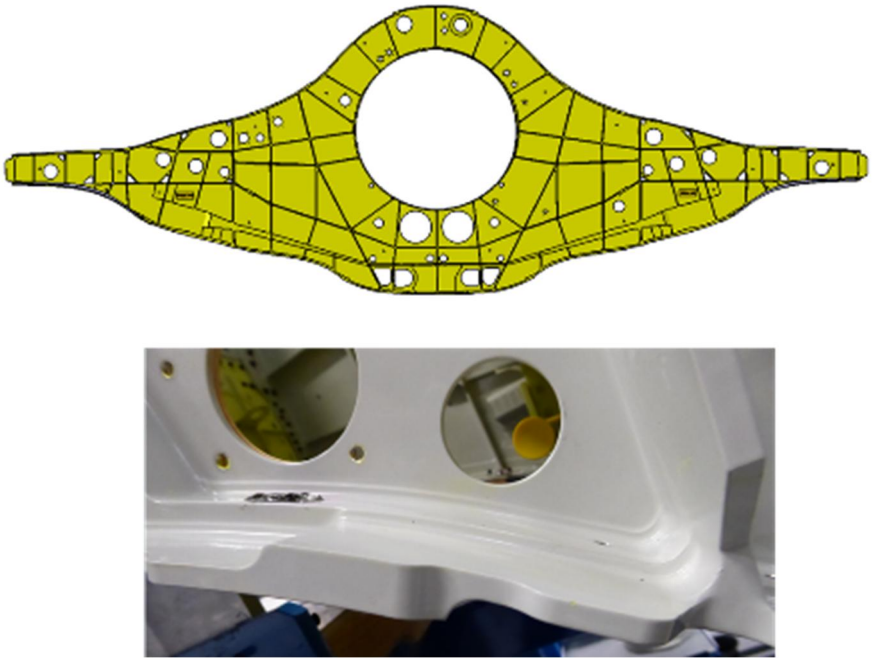

Figure 2.9-1. Monolithic structures.

Model Formulation and mechanical experiments
The topology optimization problem is defined by relevant objective functions and constraints. Both stiffness constrains and stress intensity factor constrains are evaluated. The theory is defined in [1].

A number of crack/patch scenarios are studied and fatigue testing are conducted to support the modeling work and to show that the model concept is relevant.

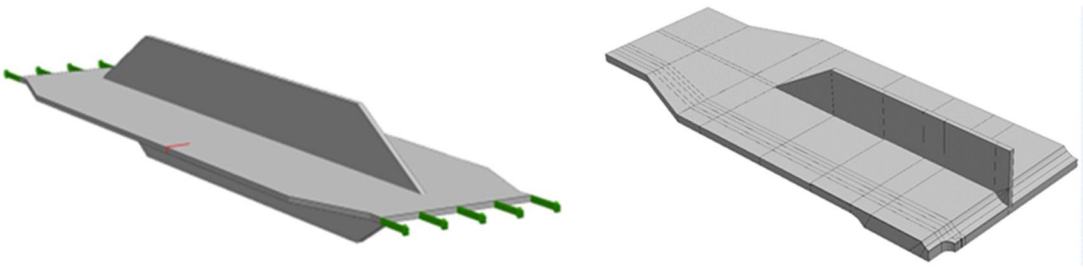

Figure 2.9-2. simplified specimens a) straight edge, b) at stress raiser.

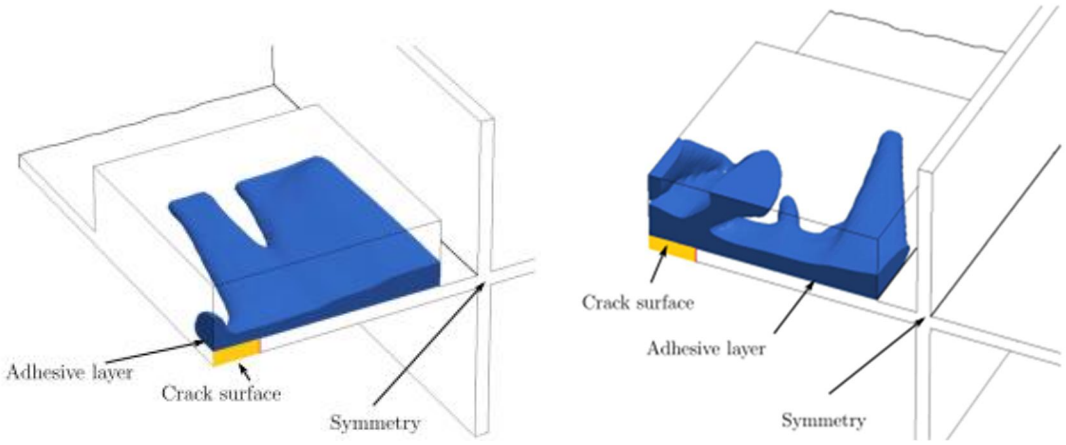

Figure 2.9-3. Optimized repair patches for crack at straight edge obtained by minimizing: a) compliance and b) energy release rate.

Initial analyzes for the optimization of repair patches for the simplified geometry have been analyzed both with and without conditions that make the design of the repair more practical to manufacture, e.g. geometric limitation in the out-of-plane direction has been introduced, figure 2.9-4

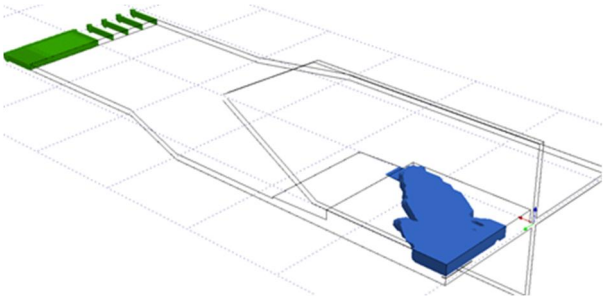

Figure 2.9-4. Optimized repair patches with geometrical out-of-plane limitations.

Implementation of the FE systems and scale-up for general applications
The models developed are implemented in FE software Trinitas for general application and demonstration of the applicability of general repairs. A full-scale demonstrator will be manufactured in which repair patches are included.

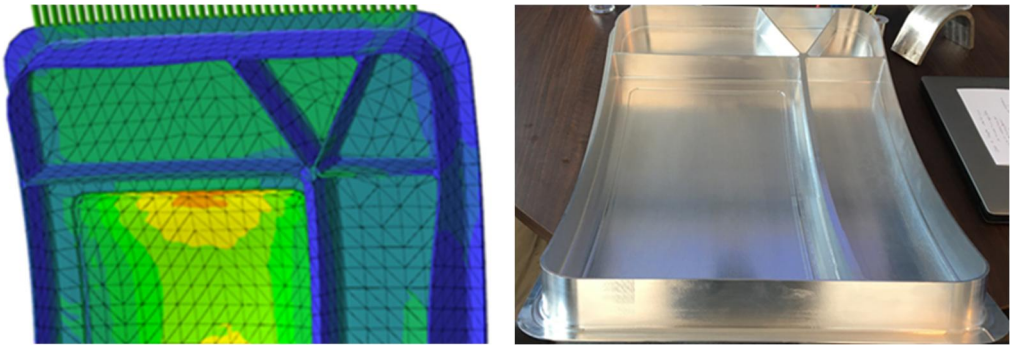

Figure 2.9-5. Monolithic door to be used for application of optimized patches.

References
[1] A. Klarbring, B. Torstenfelt, U. Edlund, P. Schmidt, K. Simonsson, H. Ansell. “Minimizing crack energy release rate by topology optimization”. In Structural and Multidisciplinary Optimization (2018) 58:1695–1703.

2.10 Fatigue performance of additive manufactured Ti6Al4V in Aerospace Applications

Magnus Kahlin, Hans Ansell, Saab AB
Johan Moverare, Linköping University

Background
Additive Manufacturing (AM) for metals includes is a group of production methods that use a layer-by-layer approach to directly manufacture final parts. In recent years, the production rate and material quality of additive manufactured materials has improved rapidly which has gained increased interest from the industry to use AM not only for prototyping but for serial production. AM offers a greater design freedom, compared to conventional production methods, which allows for parts with new innovative design. This is very attractive to the aerospace industry, in which parts could be designed to have reduced weight and improved performance contributing to reduced fuel consumption, increased payload and extended flight range. There are, however, challenges yet to solve before the potential of AM could be fully utilizes in aerospace applications. One of the major challenges is how to deal with the poor fatigue behaviour of AM material with rough as-built surface. The surface of as-built AM parts is very rough and partially melted powder grains creates micro notches which act as stress concentrations, see Figure 2.10-1.

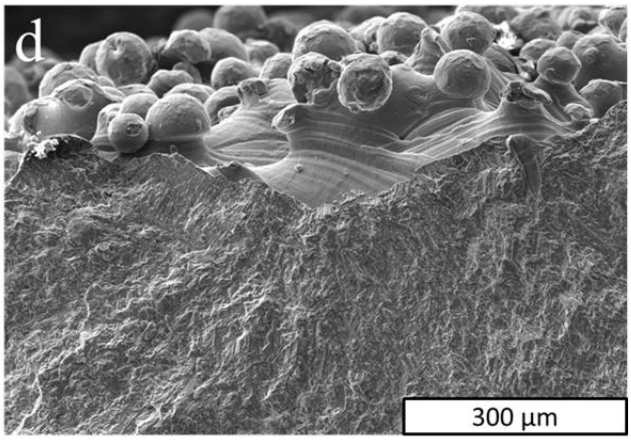

Figure 2.10-*1. Micro notch formed at the surface of an EBM sample. A fatigue crack initiation is visible at the root of the notch.*

Fatigue Investigations
This work has been focused on determining the fatigue properties of material with rough as-built AM surfaces and the combined fatigue behaviour of geometrical notches with rough as-built surfaces. The material is Ti6Al4V manufactured using both Laser Sintering (LS) and Electron Beam Melting (EBM). For smooth specimens it was found that the rough as-built surface was the single most severe factor for fatigue. The rough as-built surface alone resulted

in a fatigue notch factor, K_f, of 2.8 for LS material and 4.3 for EBM material, which correspond to 65-75% reduction in fatigue strength [1].

Few aircraft parts have, however, simple flat geometries and the effect of stress concentrations like corners or radii of curvature need to be considered, as illustrated in Figure 2.10-2. AM specimens with geometrical notches (K_t = 2.5) with rough as-built surfaces were investigated and resulted in fatigue notch factors of Kf=6.2 for LS and Kf=6.6 for EBM in relation to smooth specimens of wrought bar material. The notch sensitivity, q, was found to be equal for LS and EBM material with rough as-built surface and machined wrought material. The fatigue notch factor, K_f, have been determined for both machined and rough as-built surfaces for material with and without Hot Isostatic Pressing (HIP) treatment.

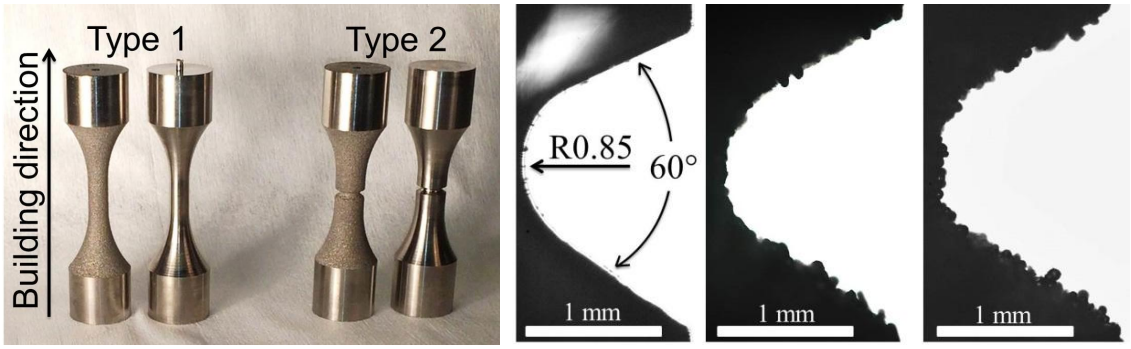

Figure 2.10-2. (left) Smooth and notched fatigue specimen. (right) From left to right; machined notched, LS as-built notch and EBM as-built notch [1].

Furthermore, the constant amplitude fatigue data and cumulative damage calculations were used to predict the fatigue life for the variable amplitude load sequence Short-FALSTAFF (Fighter Aircraft Loading STAndard For Fatigue) which is a tensile dominated load spectrum. Cumulative damage calculations were used to predict a load level corresponding to 15 000 simulated flights which were further used for variable fatigue testing. The predicted fatigue life was overall consistent to the experimental results, even though most experiments slightly exceeded the predicted life, see Figure 2.10-3. Consequently, a cumulative damage approach can therefore be used, at least for tensile dominated load sequences, to predict the fatigue life for variable amplitude loaded Ti6Al4V structures manufactured by AM.

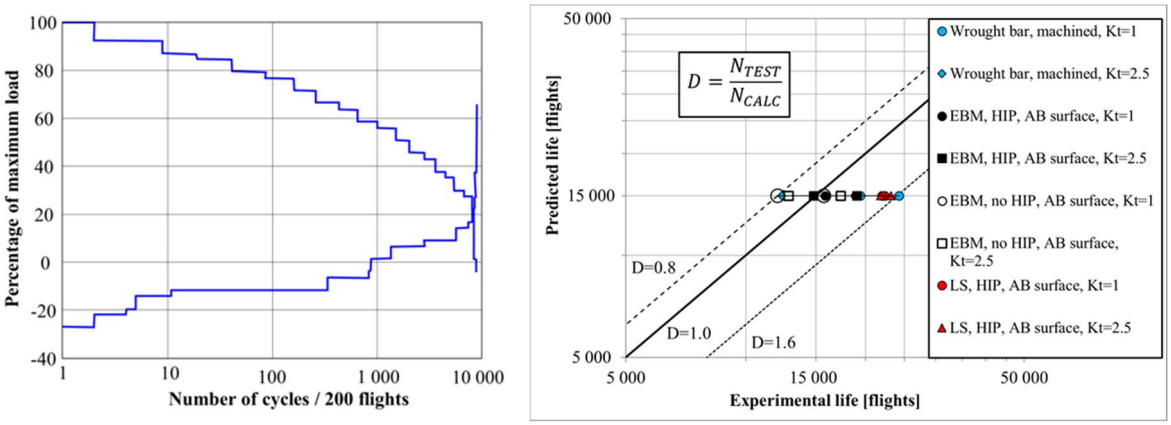

Figure 2.10-3. (left) Load distribution for the short-FALSTAFF sequence. (right) Predicted fatigue life compared to test results [2].

Conclusions and further work

Neither constant nor variable amplitude loading showed any significant improvement in fatigue life for material subjected to Hot Isostatic Pressing (HIP) treatment for specimens with rough as-built surfaces. The conclusion is that the fatigue behaviour will be dominated by the rough as-built surface rather than by defects inside the material.

Finally, to fully be able to use the potential of AM in aerospace applications, the fatigue properties need to be improved by further work to reduce the surface roughness, either by process parameter optimization or by post processing. Therefore, work is currently ongoing to identify surface post-processing techniques which will increase the fatigue performance of AM, for both EBM and LS components. Investigations into 5 post processing methods are currently made: Laser shock peening, shot peening, laser polishing, finishing (abrasive finishing) and centrifugal finishing.

Reference

[1] Kahlin M, Ansell H, Moverare JJ. Fatigue behaviour of notched additive manufactured Ti6Al4V with as-built surfaces. International Journal of Fatigue 101 (2017) 51–60.

[2] Kahlin M, Ansell H, Moverare JJ. Fatigue behaviour of additive manufactured Ti6Al4V, with as-built surfaces, exposed to variable amplitude loading. International Journal of Fatigue 103 (2017) 353–362.

3 FATIGUE AND DAMAGE TOLERANCE CHARACTERISTICS OF COMPOSITE MATERIAL AND STRUCTURE

3.1 Improved analysis capability of bolted joints in advanced metal-composite structure

Hannes Wemming Saab AB, Zlatan Kapidžić Saab AB, Hans Ansell Saab AB

Background

Weight performance and cost in the development, production and operation phases are prime factors in every air vehicle project. Lower weight typically implies overall higher stress levels which can, if not properly addressed, result in unacceptable safety-of-flight margins. One option is to use the best material combinations suitable for each structural member building up the complete assembly i.e. a hybrid structure. Often composite materials are used together with metals.

Primary hybrid airframe structure components are often joined by many bolted lap connections, which become weak points of the structure. In order to ensure acceptable safety-of-flight margins, and at the same time minimize the weight, these weak points need to be carefully considered. A thorough understanding of the material and structural behaviour, as well as reliable analytical and experimental methods need to be developed for this specific problem. The current industrial analysis approach is based on simplifying, often conservative, assumptions regarding the distribution of global and local loads, material failure and local interaction effects, especially for composite materials. There is a need for a deeper understanding of the mentioned effects as well as reliable advanced modelling techniques, capable of representing these effects. The methodology should be able to improve the design but also to produce the basis for improvement of the assumptions used in the simplified industrial approach.

The project “Improved analysis capability and strength improvement of bolted joints in advanced metal-composite structure” is a joint effort between SAAB, Linköping University, Royal Institute of Technology, RISE SICOMP and Oxeon, and is funded by the Swedish Armed Forces, Swedish Defence Materiel Administration and Swedish Governmental Agency for Innovation Systems. It started in 2018 and will run until the end of 2021. It is a continuation of previous work performed in [1] and Chapter 3.1 of [2].

Analyses and experimental work

A part of the project that is focused on improving the analysis capability ranges from the local scale, involving detailed numerical and experimental studies of bolted joint specimens to the global scale, involving analysis of complete airframe structures, e.g. a wing and its attachment to the aircraft fuselage. The analysis concerns establishing operational parameters, such as flight loads, relevant for a typical supersonic manned multirole aircraft and performed by a simplified global finite of a complete airframe. Results from the global model in terms of local load distribution serve as input for finer models and detailed analyses on a local scale, as shown in Figure 3.1-1.

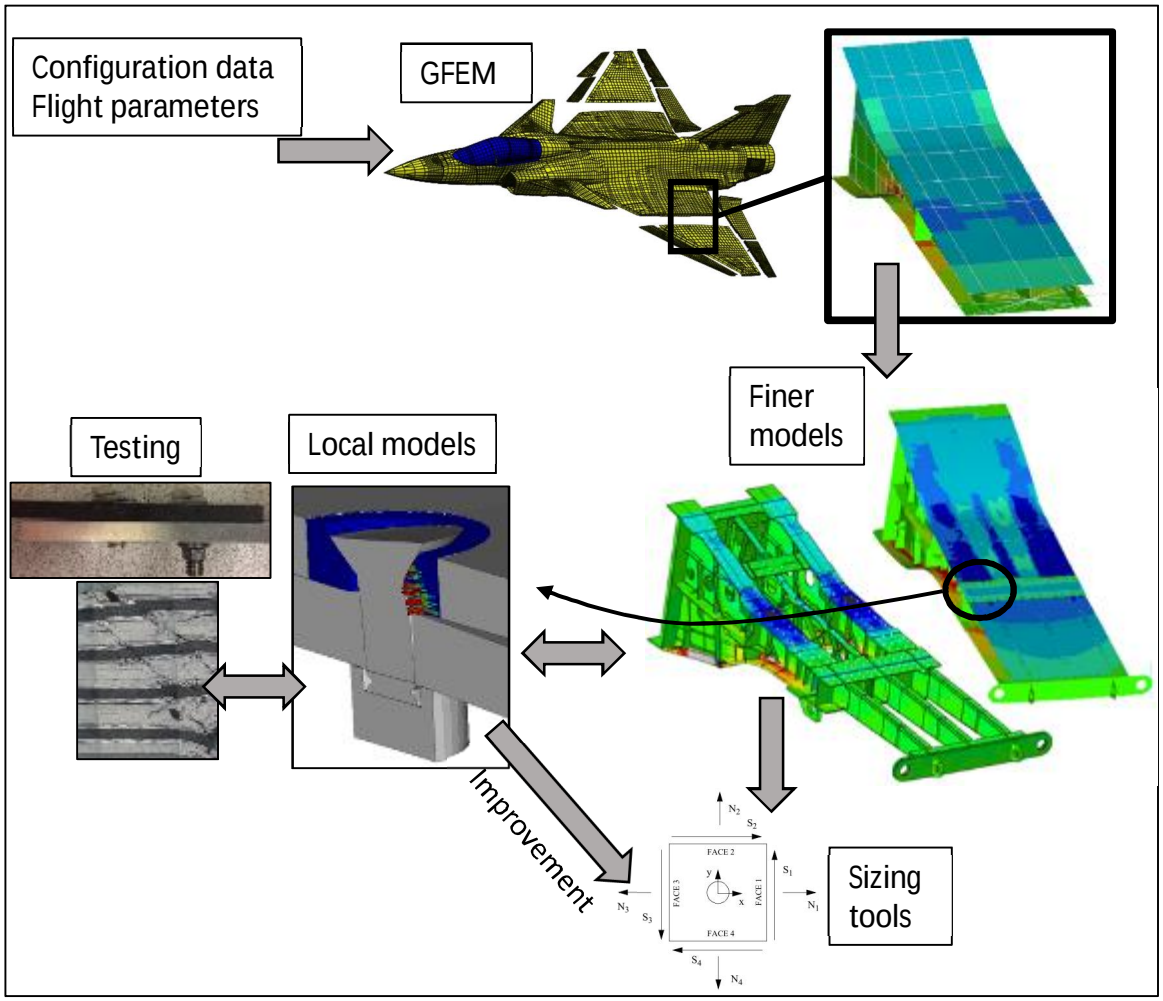

Figure 3.1-1. Analyses flow.

On local scale, experimental studies are performed on coupons such as open-hole, bearing, half-hole bearing as well as assembled single and double shear joints, see Figure 3.1-2, of varying width, hole and fastener diameter, fastener type and pre-tension level. The aim of the study is to understand and characterize the local material failure mechanisms in the joint and how they are affected by the variation of the joint parameters. Such understanding is necessary for development of physically sound modelling methods which can then be used for improvement of the sizing tools.

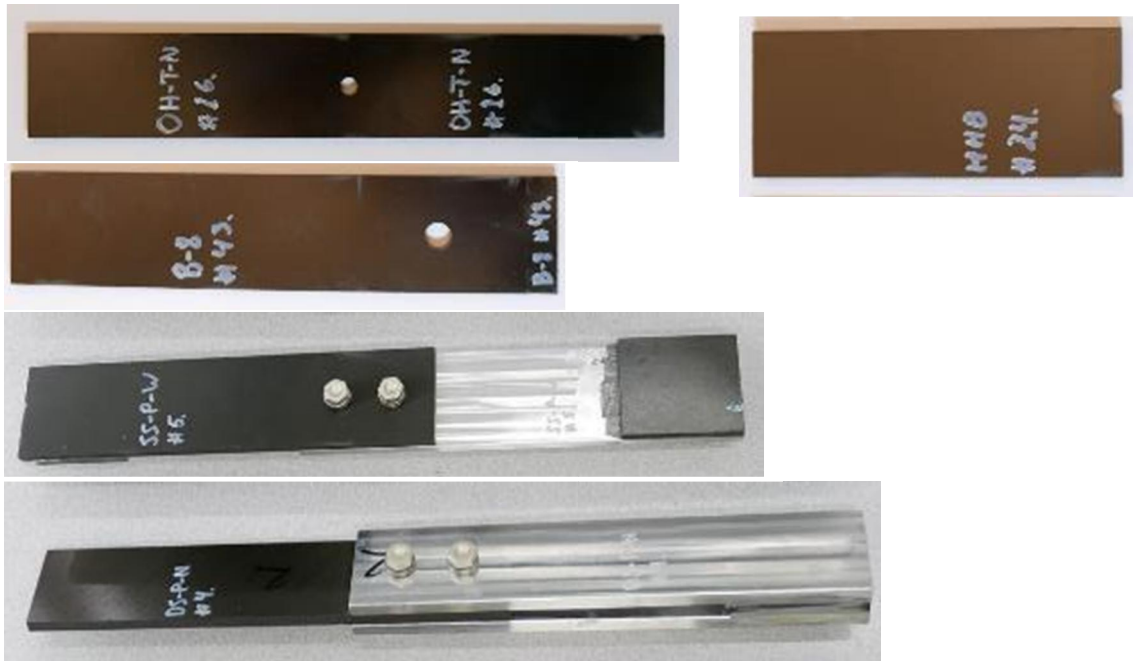

Figure 3.1-2. Specimen types: Open Hole, Bearing, Half-Hole Bearing, Single Shear, Double Shear.

The specimens are loaded quasi-statically to failure and the failure modes are registered. Force, displacement, acoustic emission (AE) and digital image correlation (DIC) strain measurements are registered during the whole loading sequence. Some specimens are tested to near failure load and studied using fractography, see example in Figure 3.1-3. Such images reveal the type of local material failure mechanisms and damage propagation.

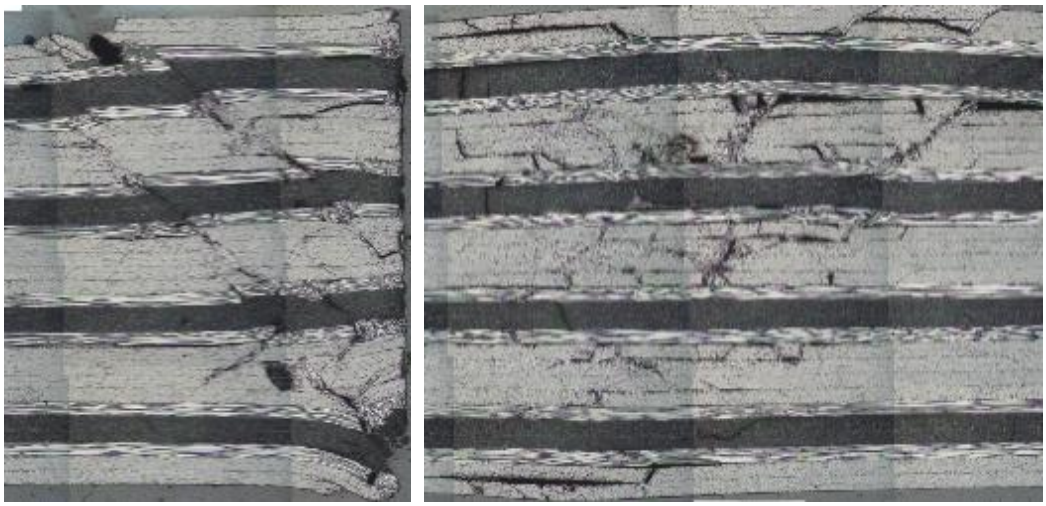
Figure 3.1-3. Fractography images of bearing plane (left) and net-section plane (right) of a double shear composite-aluminium joint.

A Stereo-DIC setup (two cameras) that make it possible to measure out-of-plane deformation of the specimen was used during the test. An example of the stereo-DIC camera images for a single shear specimen is shown in Figure 3.1-4. In Figure 3.1-5, stereo-DIC strain results measured on the surface of the laminate are compared to FE-model results at similar load levels. An example of the AE results is given in Figure 3.1-6.

The combined results from the tests, the measuring equipment and fractography are used for verification of detailed finite element simulations including progressive failure modelling.

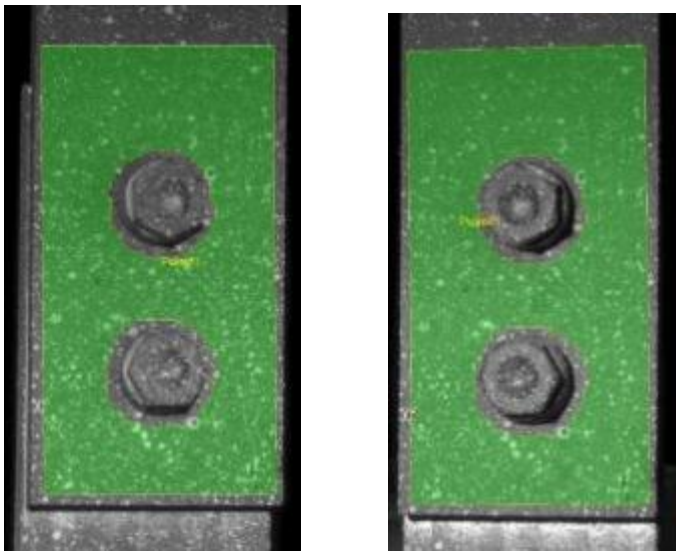

Figure 3.1-4. DIC tracking area.

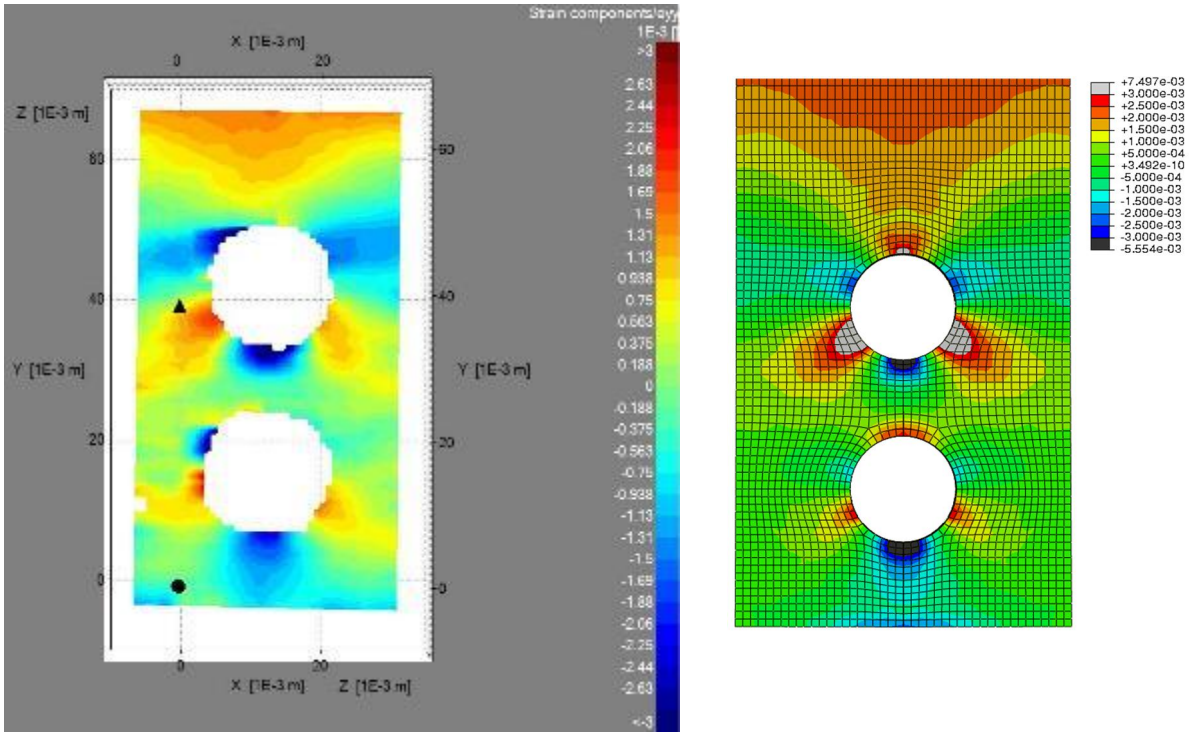

Figure 3.1-5. Strain on the laminate surface as measured by stereo DIC (left) and as computed by FE (right).

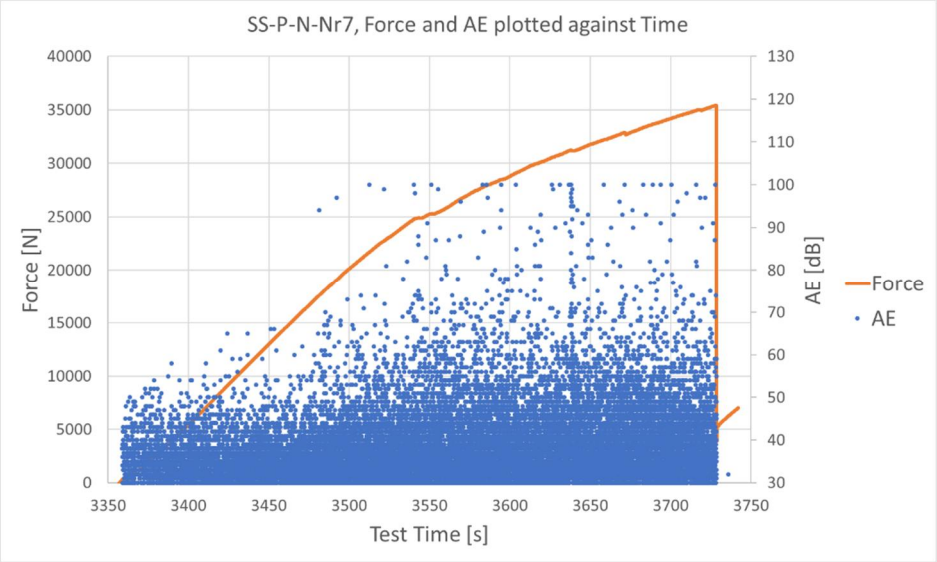

Figure 3.1-6. Force and Acoustic Emission (AE) events plotted against time for a single shear type specimen.

Finally, findings from the activities above will be included in a refined model of a large scale airframe structure, such as a wing attachment. The bolted joint behaviour from the local analyses should be included into the large scale structural model. The goal is to reach a reliable analysis method for analysing bolted joints that is suitable for industry with regards to time consumption and complexity.

Other project activities
Local hole reinforcements with metal inserts to improve bolted joint strength, see section 3.2. Carbon fibre composites made of thin plies may increase the bolted joint strength, see chapter 3.3.

References
[1] Kapidzic Z. Static and Fatigue Failure of Bolted Joints in Hybrid Composite-Aluminium Aircraft Structures, Doctoral Thesis, Dissertation No. 1706, Linköping University, 2015.
[2] Ansell, H. Review of Aeronautical Fatigue Investigations in Sweden During the Period April 2015 to March 2017, Presented at the 35th Conference of the International Committee on Aeronautical Fatigue and Structural Integrity (ICAF), Nagoya, Japan 5-6 June 2017.

3.2 Metal reinforcement around fastener holes in composites

Sahar Akbarpour, Stefan Hallström, KTH

Introduction
An effective way to improve the load bearing capacity of bolted joints in composites is to use local hole reinforcement with high-strength metals. KTH and SAAB have mutually developed a local hole reinforcement concept, schematically illustrated in Fig. 3.2-1.

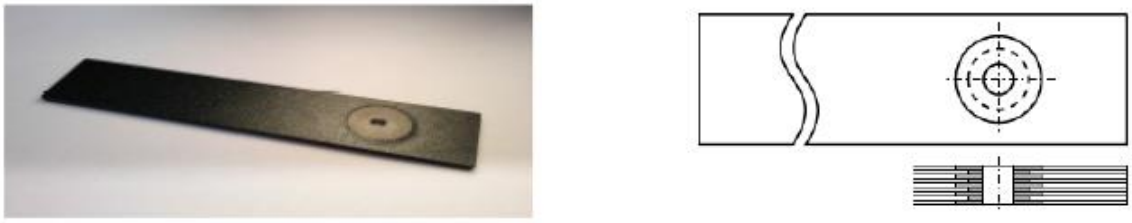

(a) (b)

Figure 3.2-1. A specimen with a patched metal insert (a) and a schematic of the insert geometry (b).

The concept uses inserts built from stacked metal patches at the locations of the holes in order to improve the bearing strength of the composite. The core of the concept is the idea to separate the bearing stress problem from the hybrid metal-composite joint problem and handle the two at different interfaces rather than at the same. In the way it is implemented the concept also provides a number of other benefits. One is the great potential for weight saving in cases where the bearing strength drives the laminate thickness. In addition, the presented concept enables clamping pressure by the fasteners and thereby joints can also partly carry load by friction. Finally, layer-wise integration of the inserts in the prepreg laminates during curing, and simpler drilling operations compared to co-drilling of metal-composite interfaces are additional advantages.

After some initial tests and a parameter study, some specimens with improved stacked patch inserts were designed for pin-loaded and open-hole tensile tests within the EU project LOCOMACHS. In another test series, some double-bolt joints were assessed in single tests as part of the RASK project. Finally, an extensive experimental work was performed within an ongoing NFFP7 project in which, the weight saving potential of the concept for single-shear bolted joints was investigated. The experimental study included testing of specimens with both stainless steel and titanium stacked metal inserts. In addition to the experimental work, 2D and 3D finite element analysis have been performed in order to investigate the local stress states and the failure mechanisms.

The insert concept can enhance the efficiency of multi-row bolted joints. A joint with higher efficiency is generally defined as a joint that carries more load without adding considerable weight. Considering multi-row bolted joints, the efficiency is not only governed by the bearing strength but also by the by-pass load between the fastener rows. The composite-metal hybrid material around the bolt hole should be designed to supply the required strength to transfer the by-pass load. Increasing the efficiency of joints in composite laminates would generally increase the efficiency of the whole composite material since the thickness of the composite material often is driven by the joint strength.

Previous research activities [1-4] have reported results demonstrating the advantageous influence of titanium hybridization on specific characteristics of CFRP-materials. It was demonstrated that use of hybrid laminates with 20% titanium content increased the specific tensile strength of a three-row bolted joint by 32% when compared to that of a CFRP laminate.

The specific bearing strength of a hybrid joint with 50% titanium content at the bearing region was 29% higher than that of a monolithic CFRP joint.

Comparing the results from testing the specimens with the stainless steel or titanium inserts, it can be concluded that high strength titanium alloy is the most suitable choice due to its relatively low mismatch of stiffness and strain to failure compared to carbon fiber reinforced plastics (CFRP). Its relatively high strength and low coefficient of thermal expansion (CTE) are also advantageous. In contrast, the high CTE and density of stainless steel are properties that are disadvantageous compared to Ti.

Experimental study

Some Pin-loaded and tensile specimens were manufactured and tested together with the references (Fig. 3.2-2). The details of the materials, specimen geometries and manufacturing processes are presented in [5]. Some improved insert configurations were designed and tested (Fig. 3.2-3). Two of the insert configurations had repetitive stacking sequences for both the patches and the composite laminates (Fig. 3.2-3(a) and (b)). In addition to the specimens with repetitive stacking sequences labelled as I3 and I4), three other insert configurations were designed by varying the stacking of the metal patches and the prepreg plies. These configurations were made from fewer metal patches and are denoted I5, I6 and I7, shown schematically in Figure 3.2-3(c), (d) and (e).

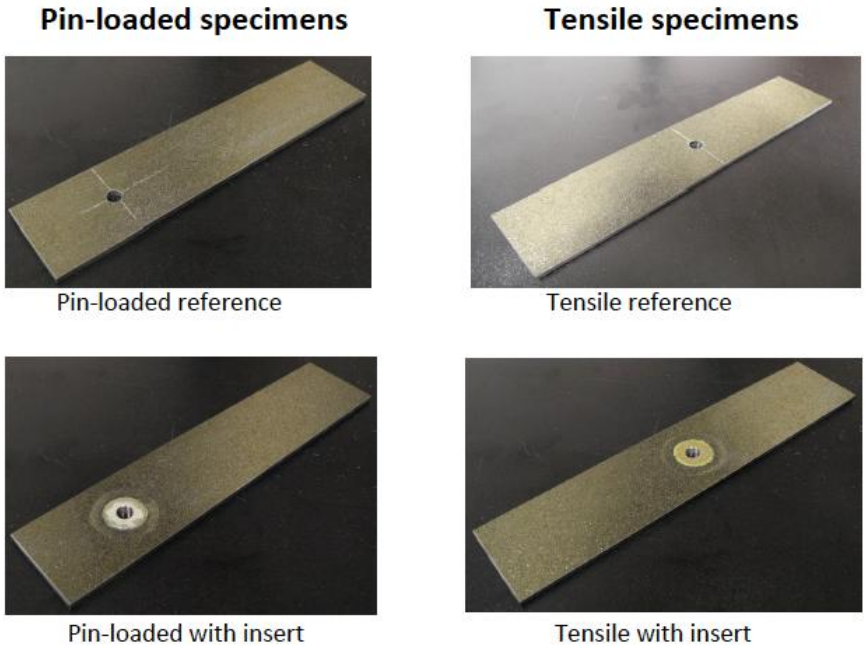

Figure 3.2-2. Pin-loaded and tensile specimens and the corresponding references.

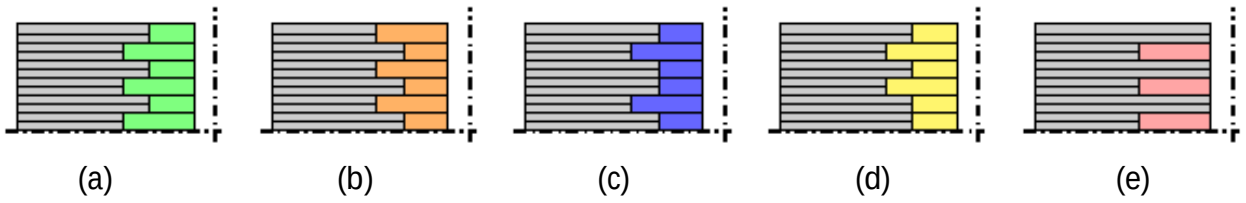

Figure 3.2-3.Insert configurations of I3 (a), I4 (b), I5 (c), I6 (d) and I7 (e).

Pin-loaded tests

The pin-loaded test setup is shown in Figure 3.2-4. The results from the pin-loaded tests were in general strikingly consistent with very low scatter as shown in Figure 3.2-5. The pin-loaded test results showed about 50-60% improvement in ultimate failure load. The results from the pin-loaded reference specimens can also be used as references for I4 and I7 since the laminates are all quasi-isotropic with 24 prepreg plies. All of the configurations showed bearing failure.

Figure 3.2-4. Test setup for pin-loaded specimens.

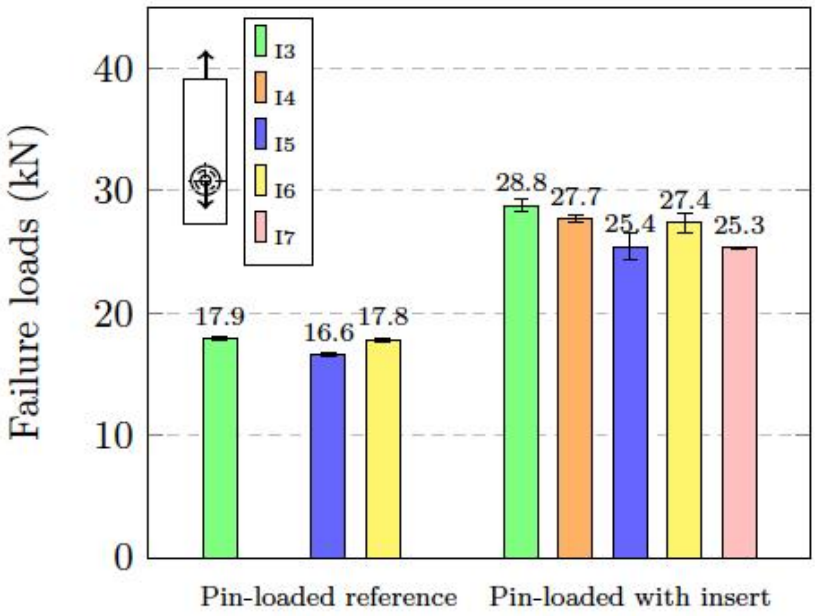

Figure 3.2-5. Failure loads of pin-loaded specimens with stainless steel inserts.

The metal patches were made of Stainless steel (AISI 301) for the first test series, mainly because of its availability. Later in the project, Ti Beta 21S alloy were also used for the concept.

The concept benefits from using a high strength metal. The nominal yield and ultimate strength of the Ti Beta 21S alloy and the Stainless steel AISI 301 were similar but the specimens with titanium inserts showed lower ultimate failure loads in pin-loaded tests as shown in Figure 3.2-6.

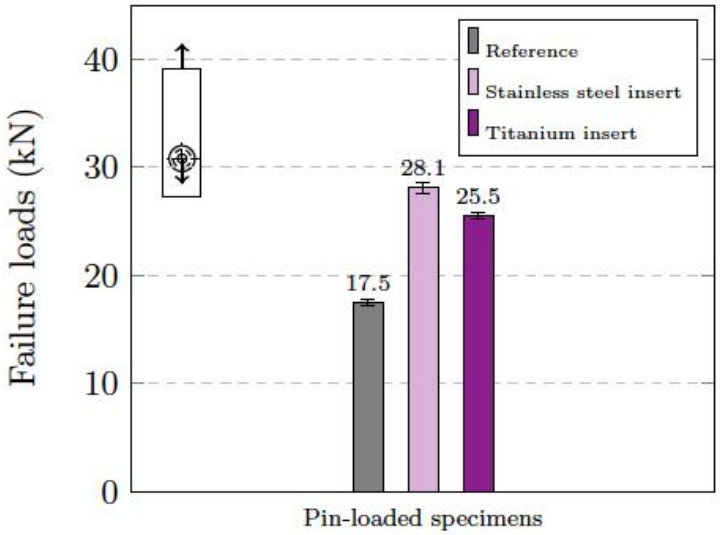

Figure 3.2-6. Ultimate failure loads of pin-loaded references, specimens with stainless steel and titanium inserts.

The bearing failure of the hole initiates at a lower load level when the hole edge deforms plastically. The 2% method (Fig. 3.2-7) was used to measure the bearing strengths of the stainless steel and titanium patches according to the ASTM standard (D5961/D5961M) and the results were compared with the composite material (Fig 3.2-8). The bearing strength of the edge was 25% and 45% higher for the specimens with titanium and stainless steel inserts, respectively, than for the references.

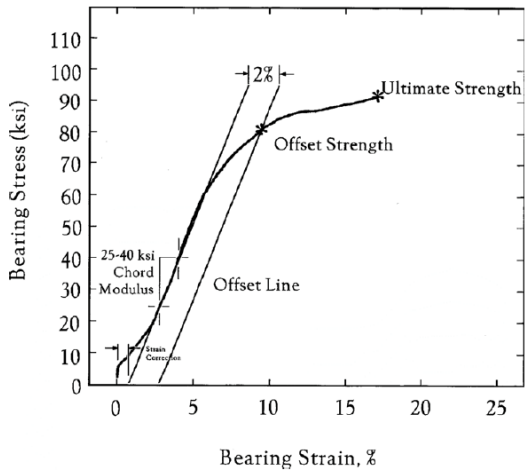

Figure 3.2-7. Example of bearing stress vs. bearing strain curve according to ASTM D5961.

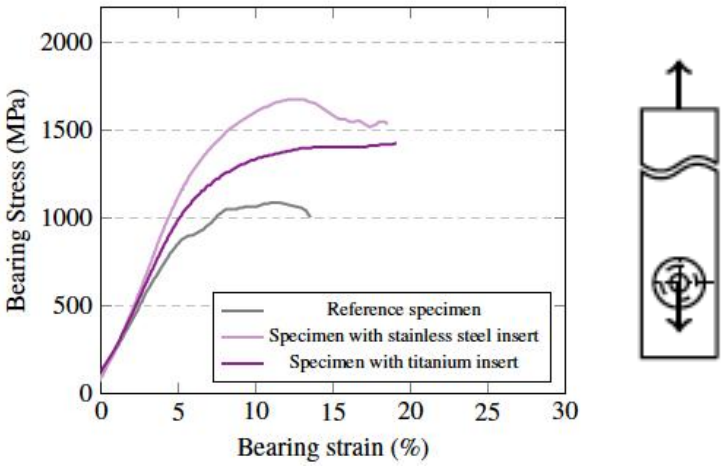

Figure 3.2-8. Bearing stress vs. bearing strain graphs from pin-loaded specimens with stainless steel or titanium inserts compared to references.

Open-hole tensile tests

Open-hole tensile tests measure the strength of the finger-joint between the metal patches and the composite and give indication of the amount of load that can be by-passed. The open-hole test setup is shown in Figure 3.2-9. The tensile strength of I3 came out 13% lower than for the reference case as shown in Figure 3.2-10. The tensile strength of I5 was considerably higher while I4 and I6 were slightly lower than for the reference case.

Figure 3.2-9. Test setup for open-hole tensile tests.

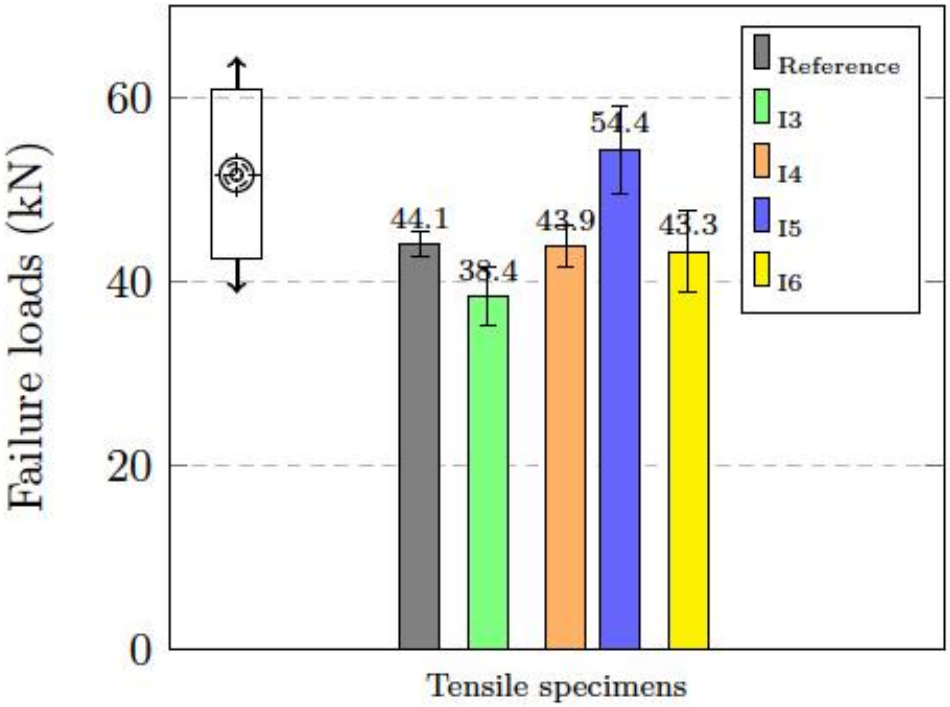

Figure 3.2-10. Open-hole tensile results for specimens with stainless steel inserts.

As mentioned, the efficiency of a bolted joint can improve considerably if both the bearing strength at the edge of the hole and the by-pass strength of the hybrid material around the hole increase. The very advantageous result of using titanium patches was the remarkably high by-pass strength. In fact, all the tested insert configurations with titanium patches showed higher by-pass strength compared to the references even the ones that were not optimized. The by-pass strengths of I3 and I4 with titanium inserts came out about 25% higher than for the reference case as shown in Figure 3.2-11.

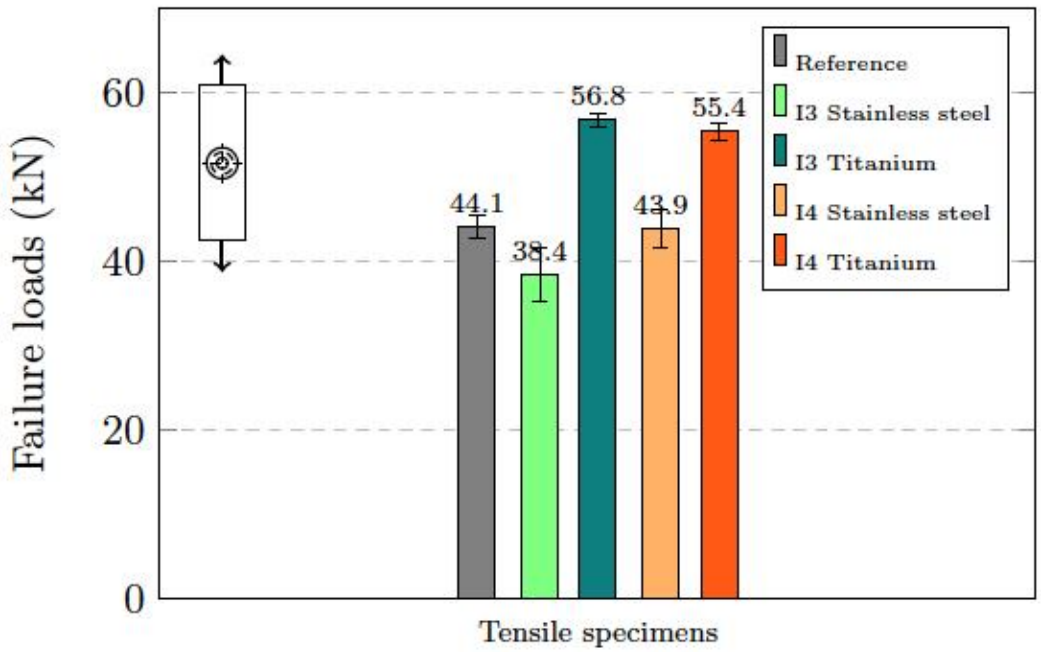

Figure 3.2-11. Failure loads of tensile references, I3 with stainless steel or titanium inserts, and I4 with stainless steel or titanium inserts.

Minimum Bolt-distance

The intension of performing pin-loaded tests for narrower specimens was to investigate whether using an insert would require increasing the bolt-distance or not. 24 mm wide specimens with stainless steel inserts were tested and the results showed that even the specimens with the minimum allowable ratio of width to diameter (W/d=4), failed due to plastic deformation at the hole edge. No composite-metal debonding or net-section failure was seen. The narrow specimens showed about 55% strength improvement compared to the references, with virtually no loss in by-pass strength.

Open-hole tensile tests at high temperatures

When a specimen with an insert is tested at temperatures higher than room temperature, the thermal residual stresses between the metal patches and the composite plies are expected to decrease because the composite-metal bond was cured at 180° C. The consequence should be higher strength. On the other hand, the strength of the composite-metal bond decreases with increased temperature as the strength of the adhesive drops decreases with increasing temperature. The graph shown in Fig. 3.2-12 illustrates the expected increase in the failure load due to lower thermal residual stresses predicted by the FE models. The reduced strengths at two elevated temperatures, together with the strength at room temperature (extracted from the adhesive datasheet) were used and the degradation was approximated with a bilinear curve in the figure. The two graphs show the purified effect of decrease in the thermal residual stresses and the lower strength of the adhesive at high temperature separately. The experimental results showed that both of these effects exist simultaneously and the failure loads of I5 specimens with stainless steel inserts fall out between the two graphs (Figure 3.2-12). The important result of these tests was that the tensile strength of the I5 specimens was higher than the bearing strength of the hole even at 140° C.

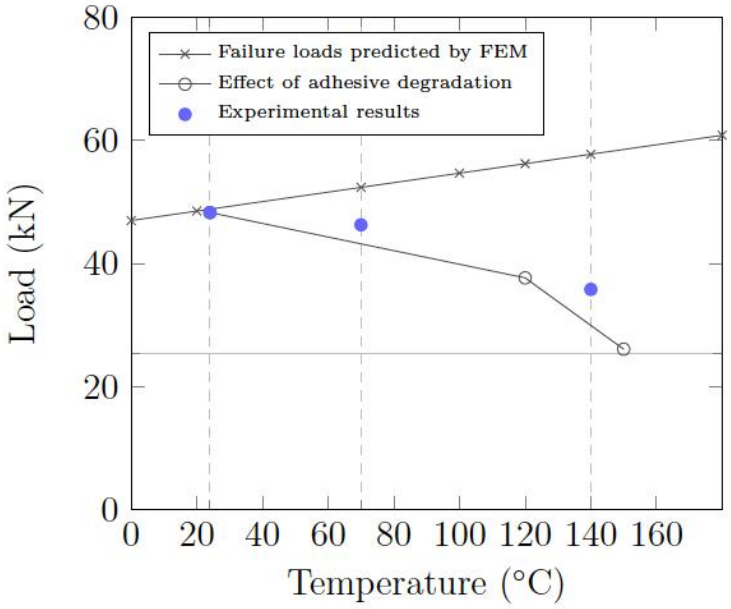

Figure 3.2-12. The tensile strength of the specimens with stainless steel inserts decreases at elevated temperature.

Single-shear tests

The single-shear test setup is shown in Figure 3.2-13. The bearing stress vs. bearing strain graphs for the single-shear double-bolt specimens are shown in Fig. 3.2-14. The final failure for these specimens happened when the bolts broke. Using the 2% method, the results showed that while the reference specimens had failed at a considerably lower load when the composite edge of hole deformed, the specimens with titanium inserts showed bearing failure at a similar level as the final load with more than 40% improvement compared to references. The improvement was even higher for the specimens with stainless steel inserts and the specimens failed when the bolts broke. It should be mentioned that at 2% bearing strain, the hole edge look more damaged for the references due to the brittleness of the composite material. The concept benefits from not only the high bearing strength but also the hardenability of the metal.

Figure 3.2-13. Test setup for single-shear test.

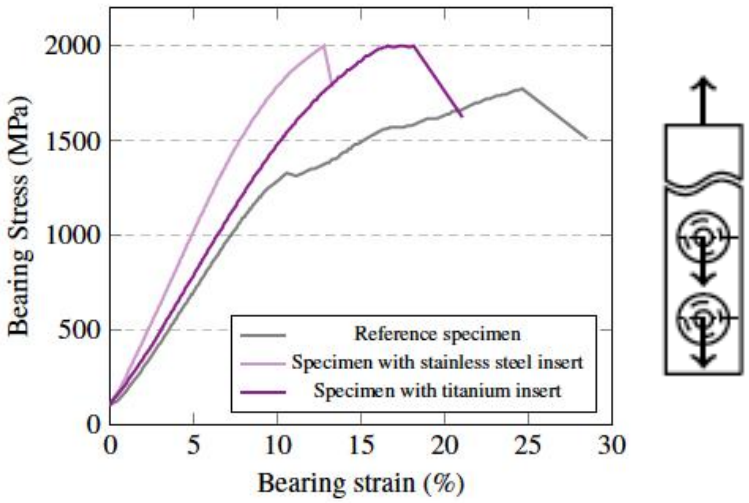

Figure 3.2-14. Bearing stress vs. bearing strain graphs from single-shear double-bolt specimens with stainless steel or titanium inserts, compared to references.

Finite element analysis

2-dimensional (2D) FE models were used to analyse the stresses at the multi-material edges of tensile specimens, using Ansys 18.0. In the neighbourhood of the multi-material corners, where there are high stress concentrations due to the elastic mismatch, a very fine mesh was used (Figure 3.2-15). The applied mechanical load was introduced as predefined displacement at the specimen ends and thermal load was also applied to simulate residual stresses from the curing process.

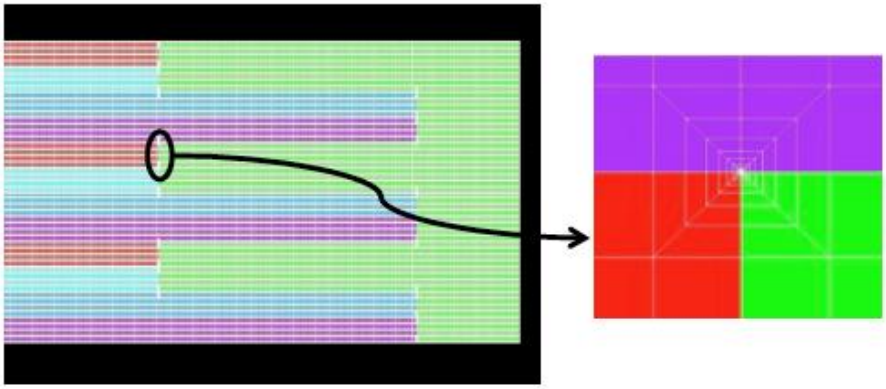

Figure 3.2-15. A 2D FE model of a composite-metal finger-joint.

In order to analyse the stress concentrations close to the hole edge and estimate the by-pass stresses, 3D FE models were used (Figure 3.2-16). In 3D modelling, the specimen geometry was represented authentically and the load transfer mechanisms and the stress contours were investigated. The singular stresses at the multi-material corners, however, could not be resolved fully in the numerical analysis using the 3D models because the very refined mesh that was used to for capturing the singular stresses in the 2D modelling would be too computationally expensive to use in 3D.

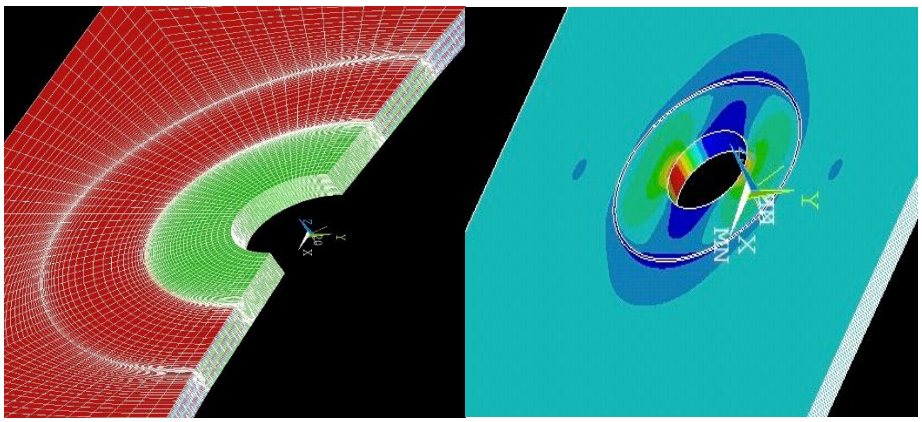

Figure 3.2-16. A 3D FE model of a specimen with an insert (a), and stress contours, σ_x[Pa] (b).

Conclusions

Local hole reinforcement of composite laminates with inserts made of stacked metal patches is an effective way to improve load bearing capability of bolted joints. In the research work, a

number of specimens with different insert configurations were designed and tested and several of them showed more than 50% strength improvement in pin-loaded tests. In addition to the bearing strength the by-pass load is also an essential parameter related to the load capacity of multi-row bolted joints. The by-pass strength of specimens with inserts was also examined through open-hole tensile tests. While only one optimized insert configuration with stainless steel insert showed 20% improvement in by-pass strength, the improvement was about 25% for almost all of the insert configurations with titanium inserts. It was shown that proper implementation of metal inserts through tailored stacking of patches at the holes of composite laminates improves the strength of bolted-joints considerably. For example, the strength of single-shear double-bolt specimens was improved with about 40% when metal patches made of Ti Beta 21S alloy were used. The efficiency of joints in composites could thus be improved significantly and thereby reduce the weight of composite parts and even structures, since the thickness of the material in many cases is driven by requirements on the joints. Further analysis and optimization activities are foreseen to bring the concept closer to industrial implementation.

References

[1] A. Fink, P.P. Camanho, and B. Kolesnikov. Hybrid titanium composite material improving composite structure coupling. *European conference on spacecraft structures, Materials and Mechanical Testing,* 2005.

[2] B. Kolesnikov, L. Herbeck, and A. Fink. CFRP/titanium hybrid material for improving composite bolted joints. *Composite Structures,* 83:368-380, 2008.

[3] P.P. Camanho, A. Fink, A. Obst, and S. Pimenta. Hybrid titanium-CFRP laminates for high-performance bolted joints. *Composites:Part A,* 40:1826-1837, 2009.

[4] A. Fink, P.P. Camanho, J.M. Andrés, E. Pfeiffer, and A. Obst. Hybrid CFRP/titanium bolted joints: Performance assessment and application to a spacecraft payload adaptor. *Composite Science and Technology,* 70:305-317, 2010.

[5] S. Akbarpour and S. Hallström. Metal reinforcement around fastener holes in composites. *European Conference on Composite Materials, 2016.*

3.3 Thin ply composites: benefits and advantages

Mohamed Loukil RISE SICOMP

Abstract

Thin-ply composites have recently been receiving significant interest in the composite industry. The motivation for this trend toward thinner plies is not only to allow the production of thinner and lighter laminates and structures, but also to provide enhanced strength and damage resistance due to increased laminate design space and positive size effects. By reducing the ply thickness in a multidirectional laminate, the in-situ effect, characterized by an increase in transverse strength of a lamina constrained between two plies with a different fiber orientation, can be observed. Matrix cracking and delamination can, therefore, be delayed without the use of special resins and/or through-the-thickness reinforcements, providing high strength and enhancing fatigue life. The aim of this paper is

to give a comprehensive overview of the implication of using thin plies in composites, its advantages and its influence on various properties and how it may influence the design.

Introduction

Composite materials have found usage in many industrial applications and more recently they are increasingly used in aerospace panels and airframes. The use of composites in the aerospace industry is justified by their excellent specific modulus and strength. When a composite laminate is loaded in tension with increasing load it will eventually fail (macroscopically). The failure is preceded by initiation and evolution of several microdamage modes and if the amount of damage increases during, for example the service life of the structure, laminate thermo-elastic properties are reduced. Several studies have been published describing the effect of damage development in composite laminates on the thermo-elastic properties [1-7]. Hence, it is desirable to suppress the damage development, especially the initiation of transverse cracks, which is typically the origin for the successive damage modes – delaminations and fiber breaks. One way to realize this effect is by reducing the thickness of the plies in the laminate which will effectively increase the transverse tensile strength of a ply [8, 9].

The potential benefits of such ultra-thin plies are several. On one hand, the use of thinner plies allows the production of thinner and lighter laminates and structures. On the other hand, per given laminate thickness, more plies can be accommodated (particularly interesting for thin laminates), increasing the design space and leading to a possibility of using smaller relative fiber angles between adjacent plies. This is beneficial for example when it comes to interfacial fracture between plies [10]. Hence, by reducing the ply thickness in a multidirectional laminate, the in-situ effect, characterized by an increase in transverse strength of a lamina constrained between two plies with a different fiber orientation, is observed. Matrix cracking and delamination can, therefore, be delayed [11-13] without the use of special resins and/or through-the-thickness reinforcements, providing high strength and enhancing fatigue life. The general effect of an increased first crack formation strain in thin layers of laminates in tension is described in [8, 9]. Another example of the thin-ply effect was demonstrated by Sihn et al. [14], who performed an experimental campaign comparing the mechanical properties of conventional laminates to thin-ply laminates. In this study they observed that without special resins, the thin-ply laminate composites suppress microcracking, delamination and splitting damage for static, fatigue and impact loadings. In [15], quasi-isotropic laminates were prepared using both standard prepregs and thin-ply prepregs in order to examine the effect of ply thickness on the damage accumulation processes. Clear difference on the damage accumulation process between standard laminates and thin-ply laminates was identified; fiber fractures occurred in thin-ply laminates. The effect of ply thickness on the crack propagation mechanism was discussed by Saito et al. [11] with respect to the energy release rate of the intralaminar transverse crack calculated using finite element analysis. They verified the crack suppression effect using thin ply and they concluded that this effect is apparently caused by a decrease in the energy release rate at the crack tip in the thin layer. The initiation and propagation of damage for Non-Crimp-Fabric thin-ply laminates under off-axis uniaxial loading are analyzed by Guillamet et al. [16]. The study showed that delamination is delayed or even suppressed for thin layers. Numerical studies presented in [17, 18] analyzing the influence of ply thickness on the in-situ strengths showed a significant improvement in transverse cracking and delamination resistance when using thin-ply based laminates.

Owing to their high crack suppression properties, one potential application for thin-ply laminates could be in cryogenic composite fuel tanks for the future aerospace vehicles such as, for example, LapCat and SpaceLiner [19]. Thin-ply laminates could replace the existing

designs of composite fuel tanks, which utilize metallic or polymer based liners for leakage control. Using thin-ply laminates with high crack suppression ability the additional liners could be omitted resulting in a more lightweight structure.

Benefits of using thin-ply composites

Increased design space

The first benefit of using thinner plies is the ability to build very light structures by decreasing the minimum possible laminate thickness. A second benefit is that of increased design space with lighter plies permitting the designer to tailor the composite properties of a laminate by adjusting the ply orientations while still satisfying design constraints such as symmetry, balance of the laminate, and minimum percentage of fiber at a particular angle. For example, the use of 37gsm (grams per square meter) thin-ply material instead of 300gsm standard weight material in a 0.9 mm sandwich skin allows the designer to propose more optimal laminates such as [0°/+α°/90°/-α°]3s instead of a [0°/+60°/-60°] asymmetric quasi-isotropic layup. With 20 gsm plies, it would even be possible to get rid of the symmetry as the number of plies would be sufficient to avoid any warping during the cooling stage [20].

Improved damage tolerance (Ply-size effect)

By utilizing cross-plies with different thickness of 90° layers the effect of ply thickness on the transverse strength was experimentally investigated at different temperatures: room temperature, -50°C and -150°C. Strain levels up to final failure have been applied to the test samples and the obtained results proved that formation of micro-cracks is delayed in the thinner layers at all the applied temperatures.

The cross-ply specimens were loaded in a step-wise manner until a certain maximum strain level, then unloaded and taken out from the testing machine. The polished edges of each specimen were studied under optical microscope and the number of cracks counted within the gauge length of 50 mm. No loading was applied during the inspection and crack counting under the optical microscope, however, the cracks were well visible due to high magnification used and due to residual thermal stresses which open the crack surfaces. Thereafter the specimens were subjected to next loading step with a higher maximum strain level and the counting of transverse cracks was performed as described before. Each step size was 0.2% of strain. All tests were performed using an Instron 8501 testing machine equipped with a 100 kN load cell. An Instron climate chamber was used for -50°C and -150°C tests using liquid nitrogen as a coolant. When reaching the temperature of -50ºC or -150ºC the specimens were allowed to dwell in the set temperature for 5 minutes to ensure an even temperature distribution in the specimens before starting the mechanical loading.

Crack density as a function of the applied strain for $[0_4/90_3/0_2/90/0_2/90_2/0_2]$s laminate and for $[90_4/0_3/90_2/0/90_2/0_2/90_2]$s laminate are shown in Figures 3.3-1 and 3.3-2 respectively.

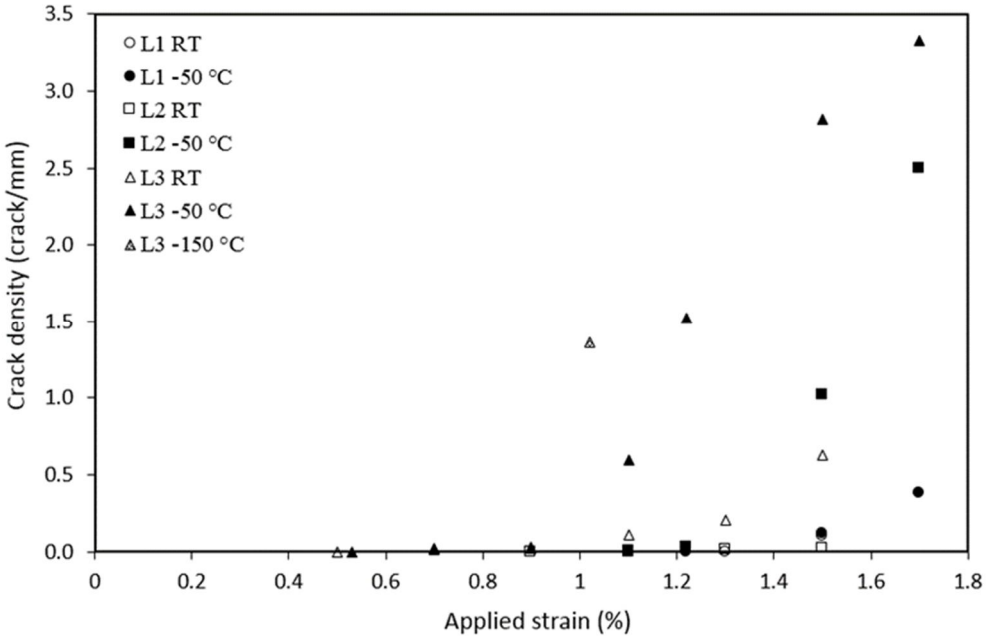

Figure 3.3-1. Crack density as a function of applied strain. RT, -50°C and -150°C

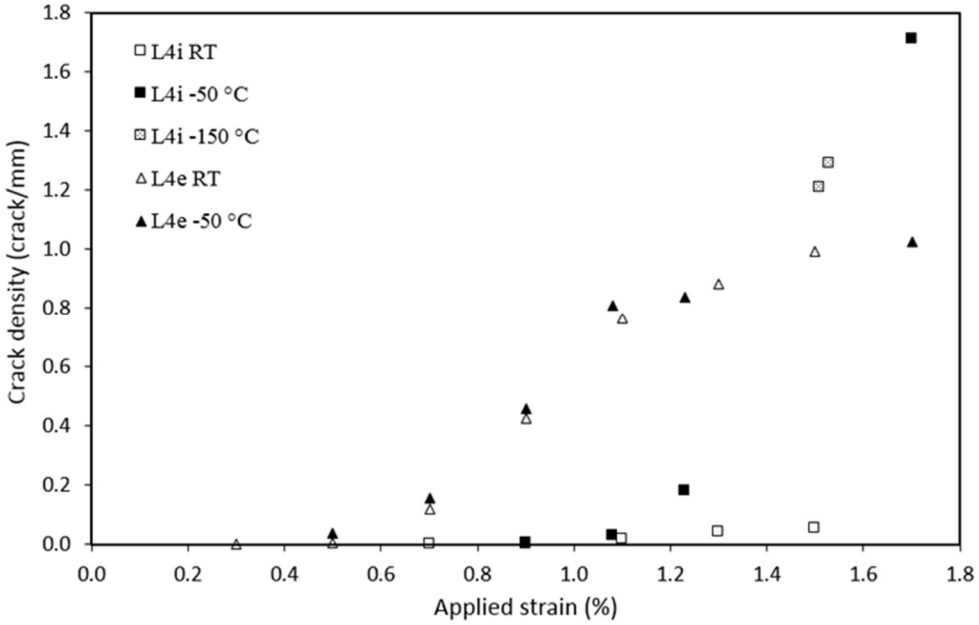

Figure 3.3-2. Crack density as a function of applied strain. RT, -50°C and -150°C

Notation of the layers is according to Figure 3.3-3.

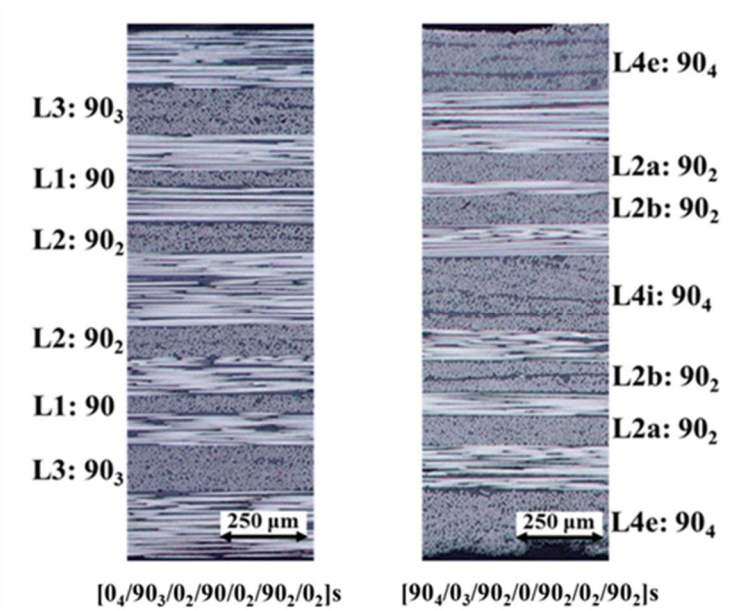

Figure 3.3-3. Optical microscopy image of a polished edge

Regarding $[0_4/90_3/0_2/90/0_2/90_2/0_2]$s laminate, Figure 3.3-1 shows that at RT, the transverse cracks initiate at 0.7% mechanical strain in layer L3, at 1.1% mechanical strain in layer L2 and at 1.5% in layer L1 mechanical strain. As expected, the initiation of transverse cracks is significantly delayed in thinner layers. Transverse cracks in very thin 90° layers, for example, in layers L1 with thickness of 50 µm, were very small and it was found that they are not propagated through the whole layer thickness even at very high applied strains (1.5%). This is specific for thin ply laminates and not typically observed in conventional laminates with relatively thicker layers, where the transverse cracks are well-defined.
$[90_4/0_3/90_2/0/90_2/0_2/90_2]$s laminate, Figure 3.3-2 shows that at RT, the transverse cracks initiate in layer L4i at 0.9% mechanical strain and at 0.5% mechanical strain in layer L4e. Only a few transverse cracks were found in layers L2a and L2b after 1.5% mechanical strain. These results follow the same trend as for $[0_4/90_3/0_2/90/0_2/90_2/0_2]$s laminate, showing delayed initiation of transverse cracks in thinner layers. In addition, the results in Figure 3.3-2 show earlier initiation of transverse cracks in the surface layers compared to internal layers of the same thickness (layers L4e vs L4i).
Regarding the effect of low temperature for both lay-ups, for the same applied mechanical strain level, the crack density in any layer is much higher when the temperature is lower as it can be seen in Figures 3.3-1 and 3.3-2. This is due to higher thermal stresses at low temperatures. Since the thermal expansion coefficient of a UD layer is higher in the 90º direction than in the 0º direction, in the studied cross-ply configurations the transverse tensile stresses in 90º layer increase by decreasing the temperature.

Improved fatigue performance
In Loukil et al. [21], cross ply $[90_2/0_3/90/0_2/90_2]_s$ laminates were tested in tension-tension fatigue in order to determine the crack density in 90° layers at different applied number of cycles. The 90° layers were denoted with respect to their thicknesses. L1=50 µm (one layer of oxeon ply), L2=100 µm and L4=200 µm (e: external).

Fatigue tests were performed at room temperature. 0.5% and 0.9% were the applied strain levels. The results were shown in Figure 3.3-4. The internal thin layer L1 has less cracks than L2 and L4 in both cases.

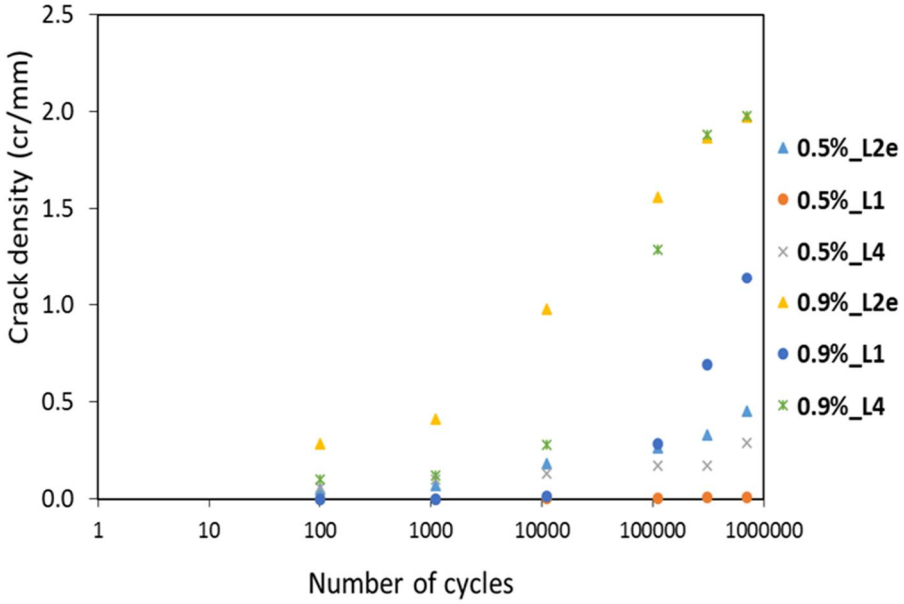

Figure 3.3-4. Crack density after tension-tension fatigue tests at room temperature

Increased bearing strength

The results presented in Figure 3.3-5 presented by Amacher et al. [13] show that the ultimate strengths attained in the single shear bearing test in as received conditions are 476 MPa for thick and 584 MPa for thin-ply quasi-isotropic laminates (+23%). When performing the test in hot–wet conditions, the difference is even more distinct as thick-ply laminates reach only 156 MPa while thin-ply laminates still achieve 372 MPa (+138%).

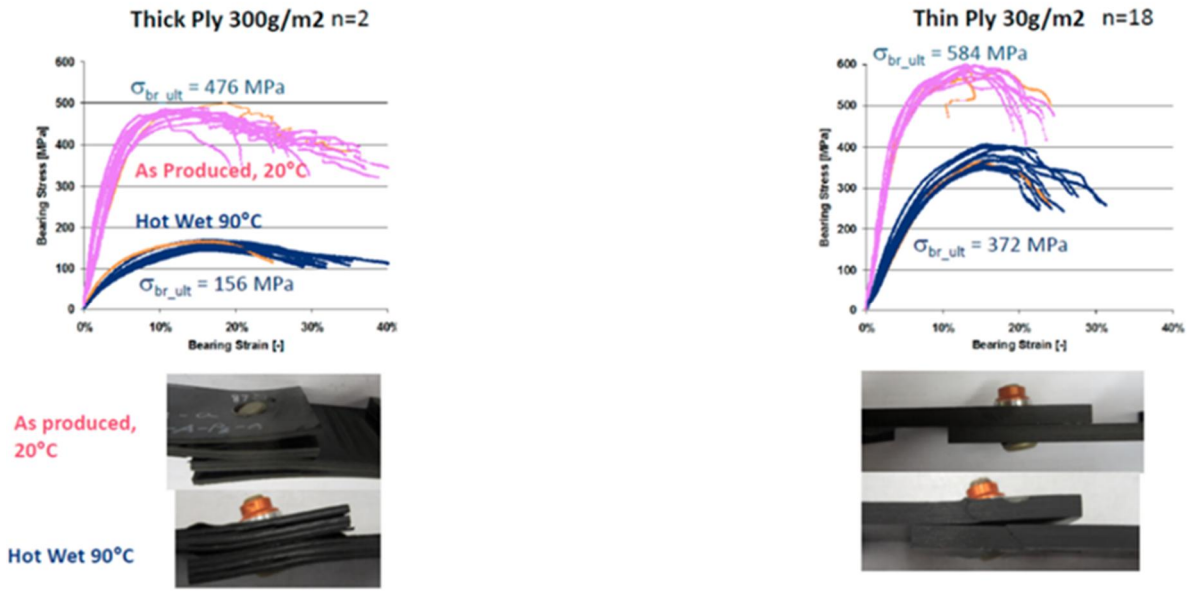

Figure 3.3-5: Comparison thick plies/thin plies bearing strength [13]

New concepts: Hybrid Structure

When it comes to improving bearing strength the first option is to use a laminate with only thin plies, however the manufacturing (time and cost) can be an issue. One option may be to work with pre-made stacks of thin-ply prepregs which will simplify the manufacturing process

and save cost. A mixture of thin/thick plies is also a solution which can be used to increase the bearing strength and decrease the production cost. If load paths are known, one of the options is to change only layers in 90° by thin-ply layers. Figure 3.3-6 shows an example of a quasi-isotropic laminate, where two extreme cases with 100% thick and 100% thin plies are presented. The third case (middle) presents and hybrid structure with 25% of thin-ply where the 0° and +/-45° layers are kept as thick plies and the 90° layer is changed to a thin-ply.

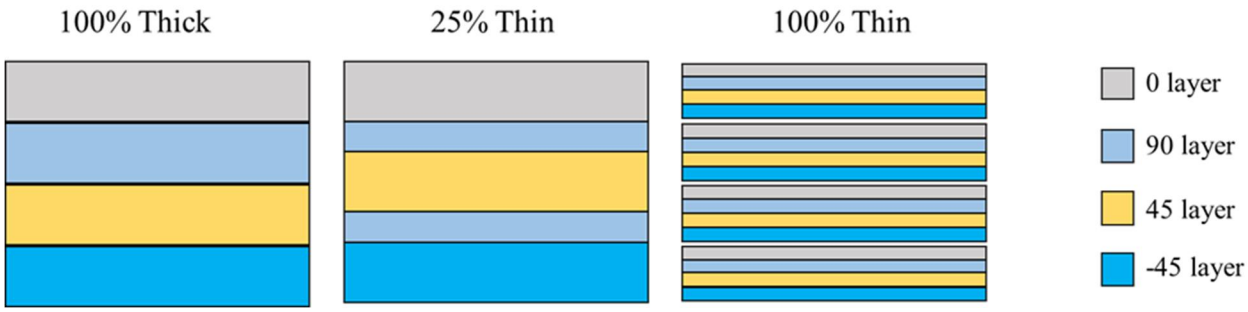

Figure 3.3-6: Hybrid structure

One option is to have 100% of thin plies at the hole area as it is shown in Figure 3.3-7. In this case the transition area thick/thin plies is very critical. To solve this problem a suggested structure is presented in Figure 3.3-8.

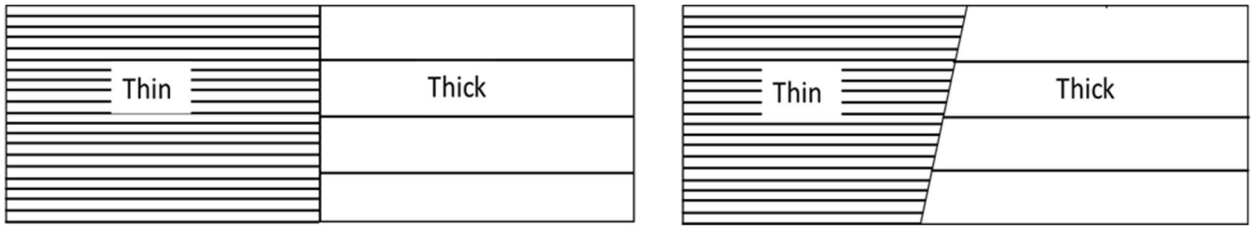

Figure 3.3-7. Critical transition area

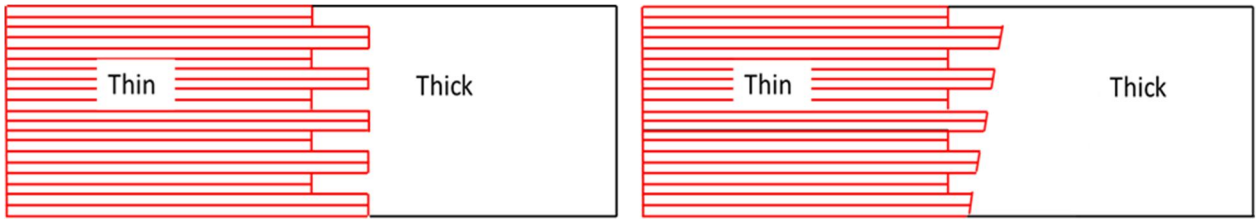

Figure 3.3-8. Solutions for the transition area

Thin plies can be considered as a means of reinforcement close to the hole to increase the bearing strength as it is shown in Figure 3.3-9 (Thin-plies can be used as a reinforcement for both sides top and bottom).

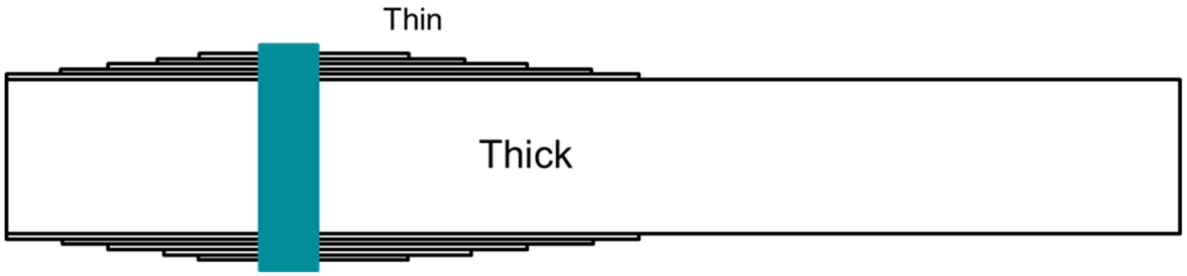

Figure 3.3-9. Thin-ply used as a reinforcement close to the hole

All configurations described in Figures 3.3-6, 3.3-8 and 3.3-9 above, will be investigated during the ongoing NFFP project “Improved analysis capability and strength properties of bolted joints in advanced metal-composite structure”.

Conclusion

Thin ply technology is becoming a viable option in composite design since a number of manufacturers have developed methods to produce thin fiber preforms at competitive prices. In this paper advantages in terms of mechanical performance such as: delaying the onset of damage development, increasing design space, and increased fatigue performance, are discussed in detail. These effects are partly due to the increased in-situ strength, and partly due to a reduced width of the zone with high interlaminar stresses. Furthermore, the benefit of increased design space with lighter plies permitting the designer to tailor the composite properties of a laminate by adjusting the ply orientations while still satisfying design constraints such as symmetry, balance of the laminate, and minimum percentage of fiber at a particular angle, opens up new possibilities in design. It was also shown that thin plies have a very high bearing strength comparing to a conventional composite material. The possibilities of using thin plies in a hybrid structures to increase the bearing strength will be investigated in ongoing NFFP7 project.

References

[1] J. M. Berthelot. Transverse cracking and delamination in cross-ply glass-fiber and carbon-fiber reinforced plastic laminates: static and fatigue loading, Applied Mechanics Review, 56(1), 2003, 111-147.

[2] M. Kashtalyan, C. Soutis. Analysis of composite laminates with intra and intrelaminar damage, Progress in Aerospace Sciences, 41, 2005, 152-173.

[3] J. Varna, L. A. Berglund. Thermo-elastic properties of composite laminates with transverse cracks. Journal of Composites Technology & Research, 16, 1994, 77-87.

[4] J. Varna and L. A. Berglund. Multiple transverse cracking and stiffness reduction in cross-ply lamintes. Journal of Composites Technology & Research, 13:2, 1991, 97-106.

[5] M. S. Loukil, J. Varna, Z. Ayadi. Engineering expressions for thermo-elastic constants of laminates with high density of transverse cracks, Composite Part A: Applied Science and Manufacturing, 48(1), 2013, pp.37-46

[6] M. kashtalyan, C. Soutis. Stiffness degradation in cross-ply laminates damaged by transverse cracking and splitting. Composites: Part A, 31, 2000, 335-351

[7] J. Zhang, KP. Herrmann. Stiffness degradation induced by multilayer matrix cracking in composite laminate. Composite: Part A, 30(5), 1995, 683-706

[8] A. Parvizi, K. W. Garrett, J. E. Bailey. Constrained cracking in glass fibre-reinforced epoxy cross-ply laminates. Journal of Materials Science, 13, 1978, 195-201

[9] G. J. Dvorak. Analysis of first ply failure in composite laminates. Engineering Fracture Mechanics, 25, 1986, 763-770

[10] J. Tao, C. T. Sun. Influence of ply orientation on delamination in composite laminates. Journal of composite materials, 32(21), 1998, 1933-47

[11] H. Saito, H. Takeuchi, I. Kimpara. Experimental evaluation of the damage growth restraining in 90 layer of thin-ply CFRP cross-ply laminates. Advanced composite Materials, 21, 2012, 57-66

[12] T. Yokozeki, Y. Aoki, T. Ogasawara. Experimental characterization of strength and damage resistance properties of thin-ply carbon fiber/toughened epoxy laminates. Composite structures, 82, 2008, 382-389

[13] R. Amacher, J. Cugnoni, J. Botsis, L. Sorensen, W. Smith, C. Dransfeld. Thin ply

composites: Experimental characterization and modelling of size effects. Composites science and technology, 101, 2014, 121-132
[14] S. Sihn, RY. Kim, K. Kawabe, SW. Tsai. Experimental studies of thin-ply laminated composites. Composites science and technology, 67, 2007, 996-1008
[15] T. Yokozeki, A. Kuoda, A. Yoshimura, T. Ogasawara, T. Aoki. Damage characterization in thin-ply composite laminates under out-of-plane transverse loadings Composite structures, 93, 2010, 49-57
[16] G. Guillamet, A. Turon, J. Costa, J. Renart, P. Linde, J.A. Mayugo. Damage occurrence at edges of non-crimp-fabric thin-ply laminates under off-axis uniaxial loading. Composite science and technology, 98, 2014, 44-50
[17] PP. Camanho, CG. Dávila, ST. Pinho, L. Lannucci, P. Robinson. Prediction of in situ strengths and matrix cracking in composites under transverse tension and inplane shear. Composite part A, 37(2), 2006, 165-76
[18] A. Arteiro, G. Catalanotti, AR. Melro, P. Linde, PP. Camanho. Micro-mechanical analysis of the in situ effect in polymer composite laminates. Composite structures, 116, 2014, 827-840
[19] M. Sippel, T. Schwanekamp, O. Trivailo, A. Lentsch. Progress of SpaceLiner Rocket-Powered High-Speed Concept, IAC-13-D2.4.05, IAC2013, 2013, Beijing,
[20] SW Tsai. Weight and cost reduction by using unbalanced and unsymmetric laminates, 2012, Proceedings of the 18th International Conference on Composite materials ICCM-18.
[21] MS Loukil M, A Pupurs, E Marklund, D Mattsson. Damage Resistance Properties of Thin-ply Carbon Fiber/Epoxy Laminates, 7th International Conference on Composites Testing and Model Identification, CompTest, Madrid 2015.

3.4 Fatigue after impact of thin ply composites

Mohamed Loukil RISE SICOMP, Zlatan Kapidžić Saab AB, Florence Rinn Oxeon AB

Thin-ply composites have recently been receiving significant interest in the composite industry. The motivation for this trend toward thinner plies is not only to allow the production of thinner and lighter laminates and structures, but also to provide enhanced strength and damage resistance due to increased laminate design space and positive size effects. By reducing the ply thickness in a multidirectional laminate, the in-situ effect, characterized by an increase in transverse tensile and shear strength of a lamina constrained between two plies with a different fibre orientation, can be observed. Matrix cracking and delamination can therefore be delayed, providing high strength and enhancing fatigue life.

RISE SICOMP and Oxeon have previously collaborated in the project UpInTheBlue, in which thin-ply composites based on Oxeon's spread tow technology were characterized in terms of static strength. Cross-ply laminates made from thin continuous carbon fibre bands were manufactured and by utilizing cross-plies with different thickness of 90°-layers the effect of ply thickness on the transverse strength was experimentally investigated. The results presented by Loukil et al. [1] proved that formation of micro-cracks in thin-ply layers is significantly delayed compared with the conventional laminate layers for static and fatigue loadings. SAAB, SICOMP and Oxeon are currently working with a project where thin ply composites is used to improve the bearing strength, ref section 3.3.

The main objective of the current project is to understand the fatigue performance of impacted thin-ply composite laminate. A comparison between the behaviour of thin ply composites (Oxeon material) and conventional prepregs used by SAAB will be performed.

References

[1] Loukil M, Pupurs A, Marklund E, Mattsson D, (2015) Damage Resistance Properties of Thin-ply Carbon Fiber/Epoxy Laminates. 7th International Conference on Composites Testing and Model Identification, CompTest, Madrid 2015.

4 THERMAL MECHANICAL FATIGUE OF SUPERALLOYS

4.1 Modelling the crack initiation and propagation in a gas turbine disc alloy under thermomechanical fatigue conditions

Daniel Leidermark, Division of Solid Mechanics, Linköping University, Sweden

In order to reach a more sustainable energy and resource usage system for the future, in which gas turbines (for propulsion and power generation) by necessity will continue to play a central role, there is a strong need for making these machines more efficient than today, which calls for higher combustion temperatures. In this context, more efficient cooling, material characterisation and life assessment models are of huge importance. With this in the back Rolls-Royce (UK) initiated the EU-funded research project: Development of experimental techniques and predictive tools to characterise thermomechanical fatigue behaviour and damage mechanisms in two nickel-base superalloys (DevTMF). This project will be ongoing from 2016 until early 2020, with the international team comprised of Linköping University (SWE), University of Nottingham (UK) and Swansea University (UK), which will perform the work in the project.

The aim of the project is to investigate, characterise and model the thermomechanical fatigue (TMF) crack growth behaviour of the relative coarse-grained disc alloy RR1000. Furthermore, to be able to properly predict the crack growth behaviour in the material under TMF load conditions, the constitutive and crack initiation behaviour need to be fully understood, quantified and modelled. Note that the project has just recently started and an outline of the upcoming work to be performed within the project is given below.

On the constitutive side, a macroscopic small-scale yielding model employing the von Mises equivalent stress with the non-linear kinematic Armstrong-Frederick backstress description [1] and a saturated isotropic cyclic softening has been implemented into a user-defined material subroutine for finite element (FE) software. In addition, during the dwell times of the TMF cycle stress relaxation (creep deformation) will occur. The creep has been modelled by use of a power-law description for the viscoplastic multiplier in a Perzyna flow model [2], where creep and plasticity are only active when above the yield limit. See Leidermark *et al.* [3] for in-depth details and Table 4.1-1 for a brief overview of the included equations in the constitutive model.

Table 4.1-1: Brief overview of the implemented constitutive model.

$$f = \sigma_{eq}^{vM}\left(\hat{\sigma}_{ij} - B_{ij}\right) - r - \sigma_Y \qquad r = r_1 + r_2$$

$$\sigma_{eq}^{vM} = \sqrt{\frac{3}{2}\left(\hat{\sigma}_{ij} - B_{ij}\right)\left(\hat{\sigma}_{ij} - B_{ij}\right)} \qquad \dot{r}_1 = q_1\dot{\lambda}$$

$$\dot{r}_2 = h(q_2 - r_2)\dot{\lambda}$$

$$B_{ij} = \sum_k B_{ij}^k \qquad \dot{\varepsilon}_{ij}^{vp} = \begin{cases} 0 & , f \leq 0 \\ \dot{\lambda}\dfrac{\partial f}{\partial \sigma_{ij}} & , f > 0 \end{cases}$$

$$\dot{B}_{ij}^k = c_k\left(\frac{2}{3}a_k\dot{\varepsilon}_{ij}^{vp} - B_{ij}^k\dot{\lambda}\right), k = 1,2 \qquad \dot{\lambda} = \left(\frac{f}{\eta}\right)^m$$

In an industrial application, it is very demanding to perform FE-simulations of every cycle in the TMF loading sequence until failure. Hence, an approach to minimise the computational time is to perform some kind of cycle jumping procedure. Either a parameter modification [4]

or extrapolation method [5] can be adopted to generate an efficient evaluation procedure of the stress/strain state, which in turn will give a sufficient crack initiation and propagation behaviour. An evaluation of cycle jumping procedure is undertaken within the project, where a modification and an extrapolation method are compared.

Before a crack starts to propagate and grow, it will initiate somewhere. The initiation location is usually in highly stressed/strained areas, where the local damage has reached a critical level so that material separation is imminent. The local damage can be attributed by flaws, surface roughness, oxidation, fretting, impact damage and/or local plasticity. With inspiration from real micro mechanisms, a local continuum damage approach has been employed to quantify the number of cycles to crack initiation. This local damage is to be related to the surface damage, as cracks are prone to nucleate at the surface. Hence, a fatigue damage model based on the memory surface concept, from the work of Jiang [6], was used to evaluate the crack initiation life. The model consist of a fatigue damage term that incorporates the material memory and plastic strain energy in the point of interest, hence eliminating the need of a cycle-counting method. The user-defined material subroutine containing the cyclic plasticity material model was updated to include crack initiation by the fatigue damage memory surface model, which calculates the TMF crack initiation damage within each cycle.

The fatigue damage model consist of a fatigue damage term that incorporates the material memory and plastic strain energy in the point of interest, hence eliminating the need of a cycle-counting method. The fatigue damage memory surface is defined as

$$g = \sqrt{\hat{\sigma}_{ij}\hat{\sigma}_{ij}} - \sqrt{\frac{2}{3}}\sigma_{mem} \leq 0$$

where σ_{mem} is the memory stress, which initially is set to the fatigue endurance limit of the material, σ_{end}. The evolution law of the memory stress is defined according to

$$\dot{\sigma}_{mem} = \sqrt{\frac{3}{2}}H(g)\left\langle\frac{\hat{\sigma}_{ij}\dot{\hat{\sigma}}_{ij}}{\sqrt{\hat{\sigma}_{ij}\hat{\sigma}_{ij}}}\right\rangle - \beta(1 - H(g))(\sigma_{mem} - \sigma_{end})\dot{\lambda}$$

The Heaviside function, *H(g)*, makes sure that the memory surface contracts when the stress state is lower than the memory stress ($g < 0$) and expands when it is on the memory surface ($g = 0$). The parameter β defines how much the surface contracts, and $\langle\cdot\rangle$ is the Macaulay bracket. The damage accumulation is then directly coupled to the memory surface, using the memory stress to account for load-sequence effects. For proportional loading conditions the evolution of the damage is thus described by

$$\dot{\omega} = \langle\sigma_{mem} - \sigma_{end}\rangle^{\alpha}\,\dot{\psi}^{p}$$

where α is a material parameter and ψ^p is the plastic strain energy. A simple multiaxial approach was adopted for the plastic strain energy evolution law

$$\dot{\psi}^{p} = H(\sigma_{kk})\sigma_{eq}^{vM}\dot{\lambda}$$

where $H(\sigma_{kk})$ accounts for micro-crack closure by making sure that damage is only accumulated during the tensile part from the loading cycle. It have to be pointed out that the fatigue damage model for crack initiation is not coupled to the stress update in the constitutive model, as traditionally done for continuum damage models. The fatigue damage model is a stand-alone model with inputs directly from the constitutive model, as it is implemented as a subroutine within the above described user-defined material subroutine. Hence, the stress and strain state in each increment is directly feed into the fatigue damage subroutine. Thus, the history of the damage is accounted for and evolves in the subsequent iterations until the critical damage is reached, initiating a macroscopic crack. Consequently, the damage accumulation during each load cycle is summed up to the critical value ω_c, representing crack initiation. This is quantified as

$$\sum_{i=1}^{N_i} \Delta\omega_i = \omega_c$$

where $\Delta\omega_i$ is the damage accumulated during a load cycle.

Based on this model, the predicted TMF crack initiation lives correlate well with the observed experimental behaviour, see Figure 4.1-1. A noticeable different for the experimental lives between *S*1 and *S*3 could be seen from the experiments. This gives a small misguidance in the calibration procedure of the fatigue parameters, as only *S*3 was included. Hence, focus is given to the longer life at the comparable strain range level, which in hand yields a larger relative factor in the predicted TMF crack initiation life of *S*1, *cf.* Table 4.1-2. Thus, more performed tests would level out these kind of deviating results. Furthermore, from the results displayed in Figure 1 it can be seen that all the predicted crack initiation lives from the FE-analyses lie within a factor of 1.3707 from the experiments, corresponding to approximately five standard deviations from the calibrated set of specimens, where the verifying analysis of *S*1 is the one setting this factor. This gives a sound interpretation that the proposed fatigue damage model enables to capture the correct behaviour of the investigated material under the applied engine relevant load conditions. For further details, see Leidermark *et al.* [3].

Table 4.1-2*:* The experimental and predicted TMF crack initiation lives and relative factor with respect to the experimental lives. Normalised with respect to the longest experimental life.

Specimen	Experimental lives	Predicted lives	Factor
S1	0.695	0.9528	1.3707
S2	0.526	0.5490	1.0440
S3	1.000	0.9622	0.9622
S4	0.593	0.5459	0.9200
S5	0.604	0.6610	1.0952

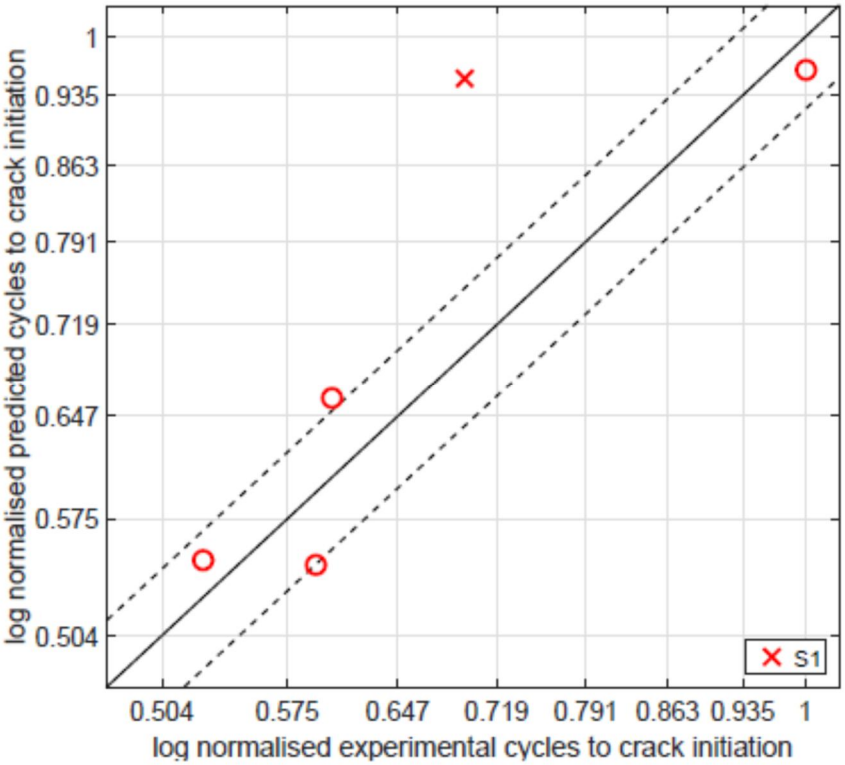

Figure 4.1-1: The normalised predicted TMF crack initiation lives versus the experimental ones.

The crack propagation modelling at these conditions will be defined by decoupling of time independent fatigue and time dependent creep crack growth, and their individual responses are summed together in a total crack extension based on the work of Bouvard [7]. Oxidisation will have an effect on the fatigue crack growth. Oxide layer thickening on the exposed crack surface may, for example, retard crack growth rates due to the associated increase in the opening threshold. Conversely, oxygen diffusion into the bulk material ahead of the crack tip can cause embrittlement, thereby accelerating the crack growth. It has from previous research been observed that the oxidation and crack closure play an important role in disc alloys [8]. This needs to be handled in a proper manner.

Focus has been shifted towards creep crack growth to incorporate effects of dwell hold times and local interaction between environment, local stress state and microstructure, which can lead to a large amount of crack front curvature. Creep crack growth properties have been calibrated for the modified Forman model [9] by observing crack growth rates for historic in vacuum RR1000 tests in isothermal conditions to avoid effects from oxidation. A creep activation temperature has been defined, below which creep mechanisms are assumed to be inactive. When creep mechanisms are active (i.e. at elevated temperatures), creep crack growth and a relaxation in the fatigue crack growth limit is represented in the model, see Table 4.1-3. Anisothermal simulations using the modified Forman model have been performed and show promising results when compared to obtained experimental data. Oxidation effects will be incorporated in the model.

Table 4.1-3: Overview of the Forman crack growth model.

$$da = \left(\frac{da}{dN}\right)_{FAT} dN + \left(\frac{da}{dN}\right)_{CR} dt$$

$$\left(\frac{da}{dN}\right)_{FAT} = \frac{C_f^* \langle \Delta S \rangle^{\eta_f^*}}{(1-R)\left[S_C - S_M\right]}$$

$$\Delta S = S_M - S_S^t = \frac{K_M - K_S^t}{K_{CV}\left(T(t)\right)}$$

$$K_{CV}\left(T(t)\right) = K_{CV}^0 \exp\left(\frac{Q}{\left(\eta_f^* - 1\right) k_r T(t)}\right)$$

All of the above mentioned modelling work is accompanied by a vast experimental testing program. Testing at high temperature conditions, especially at TMF loading conditions, is usually conducted with an induction coil, and this generates a problem when the growing crack is monitored with the commonly used potential drop (PD) technique. Hence, the testing need to be "paused" when performing the PD-measurements in each cycle, as the induction field cancels the electrical measure as PD uses. Standardisation and practical approaches will be investigated and evaluated.

References

[1] Frederick C.O., Armstrong P.J., A mathematical representation of the multiaxial Bauschinger effect, *Materials at High Temperatures,* 2007;24:1-26.

[2] Perzyna P., Thermodynamic theory of viscoplasticity*, Advances in Applied Mechanics,* 1971;11:313-354.

[3] Leidermark D., Eriksson R., Rouse J.P., Hyde C.J., Stekovic S., Thermomechanical fatigue crack initiation in disc alloys using a damage approach, *MATEC Web Conf., 12th International Fatigue Congress*, 2018;165:19007.

[4] Hasselqvist M., Aspects of creep-fatigue in gas turbine hot parts, PhD Dissertation, Linköping University, 2001.

[5] Lin J., Dunne F.P.E., Hayhurst D.R., Approximate method for the analysis of components undergoing ratchetting and failure, *Journal of Strain Analysis*, 1998;33:55–64.

[6] Jiang Y., Fatigue criterion for general multiaxial loading, *Fatigue and Fracture of Engineering Materials and Structures*, 2000;23:19–32.

[7] Bouvard J.L., Gallerneau F., Paulmier P., Chaboche J.L., A phenomenological model to predict the crack growth in single crystal superalloys at high temperature, *International Journal of Fatigue*, 2012;38:130–143.

[8] Storgärds E., Simonsson K., Sjöström S., Three-dimensional crack growth modelling of a Ni-based superalloy at elevated temperature and sustained loading, *Theoretical and Applied Fracture Mechanics*, 2016;81:2-10.

[9] Forman R.G., Kearney V.E., Engle R.M., Numerical analysis of crack propagation in cyclic-loaded structures, *Journal of Fluids Engineering,* 1967;89:459-463.

5 ACKNOWLEDGEMENTS

This editorial work was supported by Saab AB. The editor is also indebted to the following individuals who helped to write this review:

Hans Ansell	Saab AB/LiU	(Section: 2.3, 2.4, 2.5, 2.8, 2.9, 2.10, 3.1)
Hannes Wemming	Saab AB	(Section: 3.1)
Martin Ekström	Saab AB	(Section: 2.1, 2.2)
Rikard Rentmeester	Saab AB	(Section: 2.7)
Magnus Kahlin	Saab AB/LiU	(Section: 2.10)
Björn Fredriksson	Saab AB	(Section: 2.2)
Johan Moverare	LiU	(Section: 2.10)
Daniel Leidermark	LiU	(Section: 4.1)
Stefan Hallström	KTH	(Section: 3.2)
Sahar Akbarpour	KTH	(Section: 3.2)
Tomi Viitanen	VTT	(Sections: 2.8)
Mohamed Loukil	RISE SICOMP	(Sections: 3.3, 3.4)